


Spring 5-12-2018

Speleogenetic Evolution and Geological Remote Sensing of the Gypsum Plain, Eddy County, New Mexico

Jessica Shields
jmshields92@gmail.com

Follow this and additional works at: <https://scholarworks.sfasu.edu/etds>

 Part of the [Environmental Studies Commons](#), [Geology Commons](#), [Natural Resources and Conservation Commons](#), [Natural Resources Management and Policy Commons](#), [Oil, Gas, and Energy Commons](#), [Speleology Commons](#), and the [Water Resource Management Commons](#)

Tell us how this article helped you.

Repository Citation

Shields, Jessica, "Speleogenetic Evolution and Geological Remote Sensing of the Gypsum Plain, Eddy County, New Mexico" (2018). *Electronic Theses and Dissertations*. 155.
<https://scholarworks.sfasu.edu/etds/155>

This Thesis is brought to you for free and open access by SFA ScholarWorks. It has been accepted for inclusion in Electronic Theses and Dissertations by an authorized administrator of SFA ScholarWorks. For more information, please contact cdsscholarworks@sfasu.edu.

Speleogenetic Evolution and Geological Remote Sensing of the Gypsum Plain, Eddy County, New Mexico

Creative Commons License



This work is licensed under a [Creative Commons Attribution-Noncommercial-No Derivative Works 4.0 License](https://creativecommons.org/licenses/by-nc-nd/4.0/).

Speleogenetic Evolution and Geological Remote Sensing of the Gypsum

Plain, Eddy County, New Mexico

By

JESSICA SHIELDS, Bachelor of Science

Presented to the Faculty of the Graduate School of

Stephen F. Austin State University

In Partial Fulfillment

Of the Requirements

For the Degree of

Master of Science

STEPHEN F. AUSTIN STATE UNIVERSITY

May 2018

Speleogenetic Evolution and Geological Remote Sensing of the Gypsum

Plain, Eddy County, New Mexico

By

JESSICA SHIELDS, Bachelor of Science

APPROVED:

Dr. Kevin Stafford, Thesis Director

Dr. Melinda Faulkner, Committee Member

Dr. Liane Stevens, Committee Member

Dr. Kenneth Farrish, Committee Member

Pauline Sampson, Ph.D.
Dean of Research and Graduate Studies

ABSTRACT

Permian evaporites of the Gypsum Plain region of the Delaware Basin host extensive karst phenomena, as well as unique diagenetic alterations of host strata. Because of the complex, poorly understood hydrogeologic system, little has been established concerning the relation and evolution of the overprinted, modern and ancient karst manifestations within the Gypsum Plain, as a whole. Through a combination of traditional field studies and the development of improved remote sensing methodologies, this study established the speleogenetic evolution of the Gypsum Plain in relation to the greater tectonic, stratigraphic, hydrogeologic and climatic history of the Delaware Basin. Emphasis was focused on a 100 square kilometer area of the Gypsum Plain in Eddy County, New Mexico, for the presence of all characteristic evaporite karst manifestations previously reported for the region, including epikarst, epigene caves, hypogene caves, intrastratal brecciation, calcitization and sulfur oxidation.

Late Miocene uplift and tilting of the Delaware Basin tectonic block initiated development of dissolution and collapse of Castile strata, inducing an early phase of hypogene karsting. Renewed uplift and tilting during the latest Miocene, combined with increasing regional geothermal gradients, enabled hydrocarbon maturation, evaporite calcitization and additional hypogene porosity

development. Pleistocene climate fluctuations increased denudation and exposed Castile evaporites to epigene development, while migration of the Pecos River across the area during the late Eocene enhanced karst processes. Karsting slowed with the Holocene shift to the current warm, arid climate, but solutional processes remain active with the general eastward migration of the hydrogeologic system.

Traditional karst studies such as this are often costly and require months, if not years, of physical fieldwork. Preliminary identification of areas of interest through the careful evaluation of geologic maps offers a more efficient approach. However, published geologic maps of the Gypsum Plain feature little to no detail of lithologic variability, a vital attribute when dealing with phenomena dm^2 to tens of m^2 in area. Therefore, 50 centimeter spatial resolution geologic maps were created through the classification of reflectance values of color infrared imagery of the study area in order to better constrain spatial variability in karst processes. Multispectral data was used for this purpose due to the high spatial resolution commercially/publicly available over that of hyperspectral sensor's higher spectral resolutions and band combinations, deemed unnecessary because of the contrasting reflectance values of surface strata across the Gypsum Plain. Coupling of an improved speleogenetic evolution of the area with more accurate geologic mapping enables the development of better land management practices for karsted terrains such as the Gypsum Plain.

ACKNOWLEDGMENTS

First, I would like to thank my thesis advisor, Dr. Kevin W. Stafford for the unending support and guidance that he has provided over the course of my time at Stephen F. Austin State University. I sincerely appreciate all that he has done to help make this thesis a reality and the opportunity he has given me to pursue a field that I truly enjoy. Additionally, I would like to thank the Stephen F. Austin State University Student-Faculty Collaborative Research Program for providing the support and funding necessary to complete this research, as well as each member of my thesis committee: Dr. Melinda Faulkner, Dr. Liane Stevens and Dr. Kenneth Farrish. A special thank you goes to those friends and colleagues who took the time out of their own work in order to travel to New Mexico and help me complete my field studies: Lillian O'Shay, Sarah Zagurski, Jacob Meinerts, Jonah Morris and Bobby Schoen. I could not have completed this study without each and every one of you! To my parents, Mike and Kennea Shields: thank you for all of your support and encouragement, as well as listening to me endlessly talk about caves for the past few years. I would have never made it this far without you.

TABLE OF CONTENTS

ABSTRACT	i
ACKNOWLEDGMENTS	iii
TABLE OF CONTENTS	iv
LIST OF FIGURES	viii
LIST OF TABLES	xiv
PREFACE.....	xv
THE COMPLEX SPELEOGENETIC EVOLUTION OF THE GYPSUM PLAIN: EDDY COUNTY, NEW MEXICO.....	1
ABSTRACT.....	1
INTRODUCTION	3
GEOLOGIC AND HYDROLOGIC SETTING.....	6
KARST MANIFESTATION.....	10
SURFICIAL KARST	10
EPIGENE CAVES.....	16
HYPOGENE KARST.....	23
SPELEOGENETIC EVOLUTION.....	31
CONCLUSIONS	43
REFERENCES	46

A NOVEL APPROACH TO DELINEATING LITHOLOGIC VARIABILITY OF A KARSTED LANDSCAPE UTILIZING CIR IMAGERY AND GIS ANALYSES, EDDY COUNTY, NEW MEXICO	54
ABSTRACT.....	54
INTRODUCTION	56
GEOLOGIC SETTING	61
MULTISPECTRAL IMAGERY DATASET AND CHARACTERIZATION	68
IMAGE CLASSIFICATION.....	71
CONCLUSIONS	80
REFERENCES	83
APPENDIX (A) DETAILED LITERATURE REVIEW	86
INTRODUCTION	87
GEOLOGIC HISTORY.....	89
GUADALUPIAN SERIES STRATIGRAPHY	92
CHERRY CANYON FORMATION	93
BELL CANYON FORMATION.....	95
OCHOAN SERIES STRATIGRAPHY	98
CASTILE FORMATION.....	98
SALADO FORMATION	99
RUSTLER FORMATION	100
DEWEY LAKE RED BEDS.....	102

POST-OCHOAN STRATIGRAPHY.....	103
KARST AND SPELEOLOGY	104
REMOTE SENSING	110
REFERENCES	112
APPENDIX (B) DETAILED METHODOLOGY	119
IMAGE ANALYSES	120
KARST SURVEY	129
REFERENCES	134
APPENDIX (C) CAVE AND KARST	135
CAVE INVENTORY	136
BRIDGE CAVE.....	136
DEATH CRACK AND BIG ROOM CAVES	139
FIREBALL CAVE	142
GREEN MOSS CAVE	143
HORSESHOE CAVE	145
JB HOLE	147
K-HILL PIT	149
LOST CAVE.....	150
NICHOLL'S CAVE.....	152
QUILL SOIL CAVE.....	153
RED HAMMER CAVE.....	155

VB HOLE	156
ZOMBIE CAVE.....	159
VITA.....	161

LIST OF FIGURES

<p>Figure 1.1: Location of the study area in relation to the surrounding Gypsum Plain (comprised of Rustler and Castile formations) and the greater Delaware Basin, delineated by the subsurface Capitan Reef that outcrops in the various mountain ranges (from Stafford, 2008a).....</p>	4
<p>Figure 1.2: Major lithologic units of the Delaware Basin deposited during the middle- to late-Permian (modified from Scholle et al., 2004).....</p>	7
<p>Figure 1.3: Location of features of interest within this study that correspond to the greater characteristic features of the Gypsum Plain and their relationship to the overall surface geology delineated across the site (Shields et al., submitted).....</p>	11
<p>Figure 1.4: Surficial karst manifestations across the study area: A) gypsic crust found across most of the study area; B) rillenkarren on exposed Castile gypsum; C) small sinkhole manifesting as a closed depression within gypsic soil; D) spitzkarren developed on gypsum breccia boulder; E) sinkhole formed in gypsum bedrock of the Castile containing the entrance to Green Moss Cave; and F) grass filled sinkhole formed within gypsite, filled by Quaternary Alluvium</p>	13
<p>Figure 1.5. Karst mounds and areas exhibiting secondary calcitization: A) karst mounds (delineated with dashed white lines) primarily consisting Rustler strata; and B) K Hill, the largest karst mound in the study area consisting of the Rustler, Dewey Lake Red Beds and Cox strata</p>	14
<p>Figure 1.6: Classic examples of epigene morphological features associated with gypsum caves: A) scallops lining the floor and ceiling (white circle) as well as visible dissolution within the ceiling exhibiting strong fracture control; B) Example of rapid decrease in aperture of epigene cave passage seen by the extreme drop in ceiling height over only a few meters; C) Example of visible meandering of passage created by fluid flow and entrenchment along dashed lines on the lower portion of the wall</p>	16
<p>Figure 1.7: Lost Cave: A) sinkhole and entrance to Lost Cave (Eddy County, New Mexico); B) simplified map of Lost Cave.....</p>	18
<p>Figure 1.8: Horseshoe Cave, Eddy County: A) entrance to Horseshoe Cave and associated residual collapse; B) narrow, entrenched epigene passage forming the first half of Horseshoe Cave; C) large block of bedrock rotated in passage as result of undercutting during floor entrenchment; D) rapid decrease in passage</p>	

diameter at the back of Horseshoe Cave; and E) simplified map of Horseshoe Cave.....	19
Figure 1.9: Big Room and Death Crack caves, Eddy County: A) main room of Big Room Cave showing the soil floor and collapse breccia walls and ceiling; B) main room of Big Room Cave showing the relation of the entrance to the soil floor and brecciated walls of the cave; C) vertical, mud-draped drain within the floor of Big Room Cave formed completely within loosely consolidated collapse breccia by flow of waters into the cave primarily by large-scale rain events; and D) simplified map of Big Room Cave and Death Crack Cave	21
Figure 1.10: Soil caves, Eddy County: A) simplified map of Quill Soil Cave; B) simplified map of Nicholl's Cave	22
Figure 1.11: Simplified line map of Black Dog Cave (Eddy County, New Mexico).....	25
Figure 1.12: Features associated with dissolution breccias that have undergone calcitization: A) exposed area of secondary calcite as a blanket breccia; B) small Castile Buttes within the study area; C) zone of calcitization intersected during epigenic formation of Green Moss Cave; and D) calcitized zone of brecciation in Green Moss Cave.....	28
Figure 1.13: Diagram depicting the uplift and tilting experienced by the Delaware Basin tectonic block due to tectonic activity originating at the Rio Grande Rift during the early late Miocene.....	32
Figure 1.14: Diagram depicting the second pulse of uplift and tilting experienced by the Delaware Basin tectonic block during the late Miocene.....	33
Figure 1.15: Diagram depicting the beginning of epigene cave formation and denudation of the Gypsum Plain induced by the higher moisture contents of glacial periods occurring during the Pleistocene.....	39
Figure 1.16: Diagram depicting the present day state of the Gypsum Plain through the Holocene.....	41
Figure 2.1: Traditional geology map of the study area created on a small-scale of 1:500,000 (adapted from Green and Jones, 1997).....	57
Figure 2.2: Location of the study area in relation to the surrounding Gypsum Plain comprised of the Rustler and Castile formations, and the greater Delaware Basin, delineated by the subsurface extent of	

the Capitan Reef and associated outcrops in various mountain ranges. Study area outlined in red (modified from Stafford, 2008a).	59
Figure 2.3: Major lithologic units of the Delaware Basin deposited during the middle- to late-Permian with the dominant karst-bearing unit, the Castile Formation, highlighted in grey (adapted from Scholle et al.,2004).....	62
Figure 2.4: Common surficial karst manifestations within lithologies of interest across the study area: A) gypsic crust precipitate commonly deposited across a large portion of the study area; B) example of rillenkarrren formed within exposed bedrock of the Castile gypsum; C) small-scale closed sinkhole formed due to subsurface collapse within alluvium; D) example of spitzkarren formed on an exposed surface of a gypsum breccia boulder of the Castile Formation; E) open sinkhole containing the entrance to Green Moss Cave formed within bedrock of the Castile gypsum; and F) closed sinkhole formed within alluvium acting as host to a dense cluster of grasses native to the Gypsum Plain.....	64
Figure 2.5: Karst mounds and areas exhibiting secondary calcitization: A) karst mounds (delineated with dashed white lines) primarily consisting of Rustler strata; B) K Hill, the largest karst mound in the study area consisting of Rustler, Dewey Lake Red Beds and Cox strata; C) laterally extensive calcitized blanket breccia; and D) small Castile butte located within the study area consisting of brecciated Castile gypsum that has been calcitized.....	66
Figure 2.6: Location of each control point identified and field checked for nine of the 10 classes used for later classification of the color-infrared data set (control points were not established for “Vegetation”). Chart (top left) details the number of control points across the landscape corresponding to each class identified in the field	73
Figure 2.7: Color-infrared imagery of selected sites of interest evaluated, including: A) relative location of three sites within larger study area (see figure 1 for reference location of Figure 8A); B) clustered area of exposed calcitized breccia and one of the two Castile buttes located in the study area; C) K Hill karst mound remnant of paleocavern breccia infilling; and D) clustered area of karst mounds composed of Rustler collapse strata	75
Figure 2.8: Final Maximum Likelihood Classification rasters produced for each of the three areas of interest from figure 2-7: A) relative	

location of three sites within larger study area (see figure 1 for reference location of Figure 8A); B) clustered area of exposed calcitized breccia and one of the two Castile buttes located in the study area; C) K Hill karst mound remnant of paleocavern breccia infilling; and D) clustered area of karst mounds composed of Rustler collapse strata.	77
Figure 2.9: Final lithologic surface map of the study area based on the maximum likelihood classification performed.....	78
Figure 2.10: Graph displaying the mean reflectance value of each band for the corresponding class' training samples. Note distinct reflectance values for most sample classes.....	79
Figure A1: Extent and location of the Delaware Basin in the Trans-Pecos Region (MB-Midland Basin: VB-Val Verde Basin) (from Stafford, 2015)	87
Figure A2: Location and relationship of major sedimentary basins associated with study (from Pioneer Natural Resources, 2016)	90
Figure A3: Lithologic units of the Delaware Basin and associated cross-section (adapted from Scholle et al., 2004).....	93
Figure A4: Example of the spatial distribution of karstic depressions within the Castile Formation (from Stafford, 2015)	104
Figure A5: Diagram illustrating the formation of blanket-dissolution breccias through the dissolution of halite. Arrows represent fluid movement (from Stafford, 2015).....	108
Figure A6: Diagram illustrating the formation of breccia pipes through the dissolution of halite. Arrows represent fluid movement (from Stafford, 2015)	108
Figure B1: Index map of study area showing WorldView-2 CIR imagery	121
Figure B2: Location of each control point identified and field checked for nine of the 10 classes used for later classification of the color-infrared data set (Not including control points established for "Vegetation"). Chart (top left) details the number of control points across the landscape corresponding to each class identified in the field.....	122

Figure B3: Graph displaying the mean reflectance value of each band for the corresponding training samples, calculated and assigned within the Create Signatures File tool	124
Figure B4: Final lithologic surface map of the study area based on the maximum likelihood classification performed.....	128
Figure B5: Location map of control grids walked to identify cave and karst features. Caves that were surveyed are marked by a star symbol	130
Figure B6: Example of field sketches containing morphological features from JB Hole.....	131
Figure B7: Example of Walls input file containing field measurements of point locations and their corresponding length, inclination, and azimuth.....	132
Figure B8: Plan view line plot generated by Walls from data collected in the Field.....	132
Figure C1: Map of the study area detailing cave and control grid locations	137
Figure C2: Drafted cave map of Bridge Cave	138
Figure C3: drafted cave map of Death Crack and Big Room caves	140
Figure C4: drafted cave map of Fireball Cave	143
Figure C5: drafted cave map of Green Moss.....	144
Figure C6: drafted cave map of Horseshoe Cave.....	146
Figure C7: drafted cave map of JB Hole.....	148
Figure C8: drafted cave map of K-Hill Pit	150
Figure C9: drafted cave map of Lost Cave	151
Figure C10: drafted cave map of Nicholl's Cave.....	152
Figure C11: drafted cave map of Quill Soil Cave.....	154

Figure C12: drafted cave map of Red Hammer Cave.....	155
Figure C13 :drafted cave map of VB Hole	158
Figure C14: drafted cave map of Zombie Cave	159

LIST OF TABLES

Table 1.1: Members of the Castile Formation and their corresponding variable thickness as estimated based on present day values (adapted from Kirkland, 2014).	8
Table 2.1: Primary satellite sensors offering commercially-available imagery data and corresponding relevant technical specifications (adapted from Harris et al., 2011).....	58

PREFACE

Karstic development of the Gypsum Plain is the result of various complex and extensive dissolutional and diagenetic processes induced by the tectonic, stratigraphic, hydrogeologic and climatic history of the Delaware Basin. While previous studies have attempted to identify the origin and formation of karst phenomena present across the basin, little has been established concerning the speleogenetic evolution of the region as a whole. This, and other such characterizations of karsted terrains, is generally a costly, time consuming endeavor, made more efficient by preliminary site evaluations for the presence of karst phenomena through the careful study of geologic maps. Often, only small scale geologic maps are available, which are useless for the evaluation of features that range in area from a few dm^2 to tens of m^2 , such as karst manifestations of the Gypsum Plain. Remote sensing methodologies are actively being pursued in order to offer an alternative source of geologic maps through the classification of surface reflectance values derived from satellite imagery.

The following research established the formational history of karst of the Gypsum Plain, as well as a novel approach to the development of new and improved methodologies for the creation of geologic maps using multispectral satellite data. This study aims to aid in the development of improved best management practices of water and karst natural resources by entities such as

the Bureau of Land Management, as well as improve the efficiency of similar studies. In addition to multiple sections focused on the previously outlined research, a supplementary in-depth literature review, detailed methodologies employed in both evolution and satellite imagery analyses and a complete inventory of all caves surveyed throughout the course of this study are included as Appendices A, B and C, respectively.

**The Complex Speleogenetic Evolution of the Gypsum Plain:
Eddy County, New Mexico**

ABSTRACT

The Permian evaporites of the Gypsum Plain of southeastern New Mexico and West Texas host an extensive array of karst features, including epigene and hypogene manifestations, as well as complex diagenetic alteration of strata within a complex, poorly understood hydrogeologic system. This study attempted to characterize and relate these manifestations within the greater tectonic, stratigraphic, hydrogeologic and climatic regime of the Delaware Basin since deposition of host strata in order to delineate a speleogenetic evolution of the Gypsum Plain. Late Miocene uplift and tilting of the Delaware Basin tectonic block initially incited development of dissolution and collapse within salt members of the Castile Formation by initiating upward migration of fluids from underlying formations. Brecciated zones began to form within the Castile Formation as well as hypogene cave features. Continued uplift and tilting during the late Miocene, combined with increasing regional thermal gradients enabled maturation of hydrocarbons, promoted continued dissolution/collapse of strata and enabled hydrocarbon migration to fuel sulfate reduction coupled with evaporite

calcitization. Climate change associated with Pleistocene glacial/interglacial fluctuations largely sculpted the modern geomorphic landscape and formed the majority of epigene caves within the Gypsum Plain. Additionally, migration of the Pecos River across the Gypsum Plain during the late Eocene enhanced both hypogene and epigene karst development, including intense localized dissolution associated with solution-subsidence trough formation. Karst processes slowed with a Holocene shift to the warm, arid climate experienced across the region today, but speleogenesis remains active with the general eastward migration of the hydrogeologic system as updip portions of the Gypsum Plain become more heavily eroded.

INTRODUCTION

A wide variety of karst features characterize Permian evaporite facies of the Gypsum Plain of southeastern New Mexico and West Texas. The region is the site of extensive epigene and hypogene cave development, accompanied by widespread surficial karst manifestations and related occurrences of secondary mineralization, all of which are formed within a highly complex and poorly understood heterogeneous hydrogeologic system. While previous studies have attempted to identify the origin and formation of different types of karst features present, little has been established concerning the relation and evolution of all forms of manifestations as a whole, due to the complex nature of the system. This study characterized and related the karst manifestations of the Gypsum Plain to the greater tectonic, stratigraphic and hydrogeologic history of the area in order to establish a speleogenetic evolution. The theorized model incorporates the complexly overprinted region containing both modern and ancient karst phenomena as well as extensive diagenetic alteration of host rock. Individual manifestations include: epikarst, epigene caves, hypogene caves, intrastratal brecciation, sulfate reduction and sulfur oxidation associated with an evolving hydrogeologic system, as well as probable hydrothermal alteration associated with basaltic dike emplacement.

The study area used to unravel the speleogenetic complexity in this study (Figure 1.1), is an approximately 100 km² area located along the northwestern

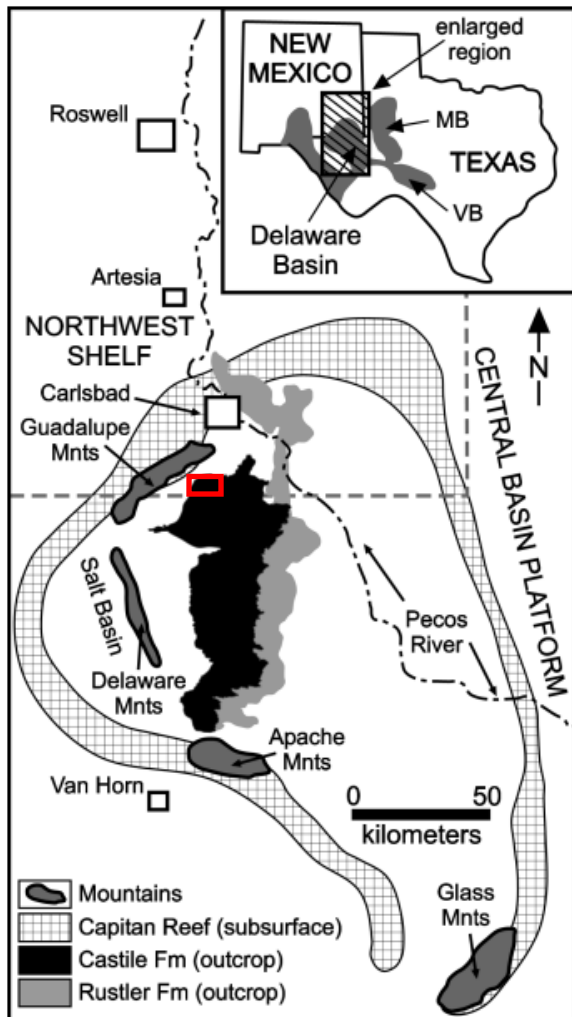


Figure 1.1: Location of the study area in relation to the surrounding Gypsum Plain (comprised of Rustler and Castile formations) and the greater Delaware Basin, delineated by the subsurface Capitan Reef that outcrops in the various mountain ranges (from Stafford, 2008a).

edge of the Gypsum Plain of southeastern New Mexico and West Texas, adjacent to the eastern face of the Guadalupe Mountains and Black River Valley. The entire Gypsum Plain is an area of approximately 2,800 km² of Permian age evaporites along the western margin of the Delaware Basin, primarily consisting of the Castile Formation in outcrop. The basin is located within the northern portion of the semiarid Chihuahuan Desert in the Great Plains Province (Hill, 1996). The area receives an average annual precipitation of 26.7 cm of rainfall, while temperatures average

approximately 17°C, with an average minimum of 9°C and maximum of 25°C (Stafford, 2008b). The portion of the Gypsum Plain in which the study area

resides is commonly referred to as the Yeso Hills area, located along the Texas border in Eddy County, New Mexico, and was selected as the primary area of emphasis due to the concentrated presence of numerous unique karst manifestations representing the total diversity of karst reported across the Gypsum Plain. Specific karst phenomena include the Yeso Hills Selenite Mine, K Hill, Black Dog Cave, basaltic dikes, artesian mineralized springs, paleokarst erosional remnants, intrastratal breccia, calcitized evaporites and other notable features discussed below.

GEOLOGIC AND HYDROLOGIC SETTING

During the mid to late Paleozoic, the Delaware Basin was formed as an intracratonic, deep marine basin due to assimilation of Pangea and resulting Ouachita Orogeny (Hill, 1996; Dickenson, 1981; Stafford, 2017). During Guadalupian time, the Delaware Mountain Group siliciclastic formations were deposited in the basin while Capitan Reef carbonates rapidly formed along the basin margin and a series of interfingering evaporites, carbonates and clastics were deposited as fore- and back-reef facies. Thick sequences of evaporites were deposited within the basin during Ochoan time, following basin restriction to open marine circulation through the closing of the Hovey Channel, which induced a transition to a density-stratified, hypersaline inland sea (Scholle et al., 2004; Stafford, 2017). The Castile Formation was deposited as a series of seven alternating members of laminated to massive anhydrite/gypsum and halite (Henrickson and Jones, 1952) directly overlying the Delaware Mountain Group as a result of basin restriction, followed by evaporites of the Salado and Rustler formations and Dewey Lake Continental Red Beds that cap the Delaware Basin and extend onto the surrounding Guadalupian shelfal deposits (Figure 1.2) (Hill, 1996). Dehydration/hydration processes associated with burial/exposure of the Castile sulfates have caused variable sulfate textures within strata, including

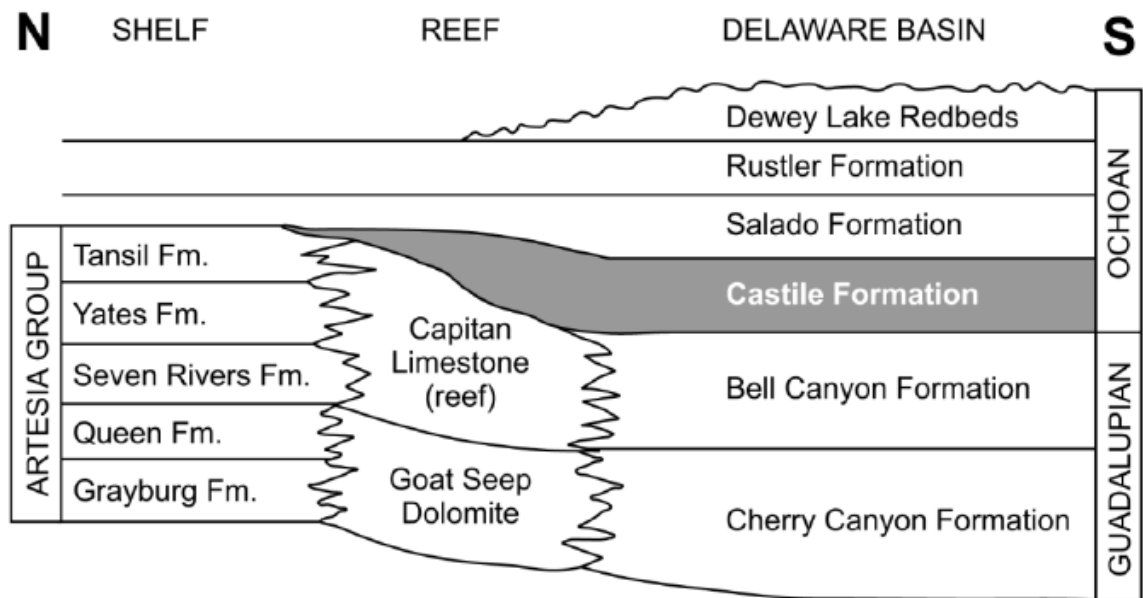


Figure 1.2: Major lithologic units of the Delaware Basin deposited during the middle- to late-Permian (modified from Scholle et al., 2004).

laminated, massive, nodular and selenitic fabrics (Machel and Burton, 1991; Stafford et al., 2008c; Dean et al., 1975; Stafford, 2008b). Alternating Castile anhydrite and halite members vary in thickness across the Gypsum Plain, as well as solubility (Table 1.1).

From the early Mesozoic to the beginning of the late Miocene, the Delaware Basin was a tectonically quiescent area experiencing sporadic deposition by fluvial sediments, including the interbedded sandstone and conglomeratic facies of the Cretaceous Cox Formation (Kirkland, 2014; Hill, 1996). A short period of volcanism occurred due to crustal shortening as regional tectonics shifted from Laramide compression to Basin and Range extension in the late Eocene to mid-Oligocene, coupled with emplacement of a series of

northeast trending basaltic dikes across the basin (Price and Henry, 1985; Hill, 1996). Uplift and tilting of the Delaware Basin tectonic block associated with western extension along the Rio Grande Rift during the late Miocene, as well as a renewed pulse during the latest Miocene to early Pliocene, acted to initiate most speleogenesis evident today within the basin. From the end of the Pliocene until the beginning of the Quaternary, the climate within the Delaware Basin was that of a hot and arid desert (Hill, 1996; Thomas, 1972). A shift in climate occurred during the Pleistocene, fluctuating between glacial periods of higher moisture and dryer, interglacial periods; followed by a final shift during the Holocene to the warm, arid environment present today (Bachman, 1980; Hill, 1996; Thomas, 1972).

Table 1.1: Members of the Castile Formation and their corresponding variable thickness as estimated based on present day values (adapted from Kirkland, 2014).

	Member	Thickness (m)
Castile Formation	Anhydrite IV	90-180
	Halite III	~120
	Anhydrite III	~90
	Halite II	~60
	Anhydrite II	~30
	Halite I	~125
	Anhydrite I	~50

Formations of the Delaware Mountain Group are the primary groundwater source of the Delaware Basin, recharging from flow originating in proximal mountain ranges, especially the Guadalupe Mountains and Delaware Mountains along the western uplifted portion of the basin, to ultimately discharge to the northeast as flow entering the Pecos River or the Capitan and San Andres aquifers (Hill, 1996). Waters generally flow down-dip along the potentiometric surface of basin strata, causing dissolution of adjacent areas (Hill, 1996;

Kirkland, 2014). The ancestral Pecos River migrated across the Delaware Basin multiple times during the early Paleogene to late Neogene, creating a persistent potentiometric low influencing groundwater flow (Thomas, 1972; Stafford, 2009). Surface flow across the basin generally migrates along surface dip until entering the groundwater system through open conduits and subsequently flowing down dip along the basin or entering the Delaware Mountain Group aquifer.

KARST MANIFESTATIONS

The Gypsum Plain is the site of extensive cave and karst development due to the high solubility evaporite strata that dominate the region. Karst manifestations range from surficial phenomena of secondary precipitates, karren, sinkholes, karst mounds and solution-subsidence troughs, to epigene caves of various lengths and hypogene phenomena including breached conduits, brecciated zones and areas of secondary sulfur deposits and calcite alteration. These features represent the regional complexity of speleogenesis induced through a combination of evolving tectonics, hydrogeology, thermal gradients and climate change. The karst phenomena characteristic of the Gypsum Plain, as well as corresponding examples documented within the study area, are detailed in the following sections (Figure 1.3).

Surficial Karst

A variety of surficial karst features exist across the study area, including secondary precipitates, karren, sinkholes, karst mounds and solution-subsidence troughs. Post-depositional alteration of exposed gypsum bedrock has resulted in a few mm to several cm thick gypsic crusts across the majority of the Gypsum Plain (Stafford, 2008b; Watson, 1982). Saturated fluids produced by dissolution

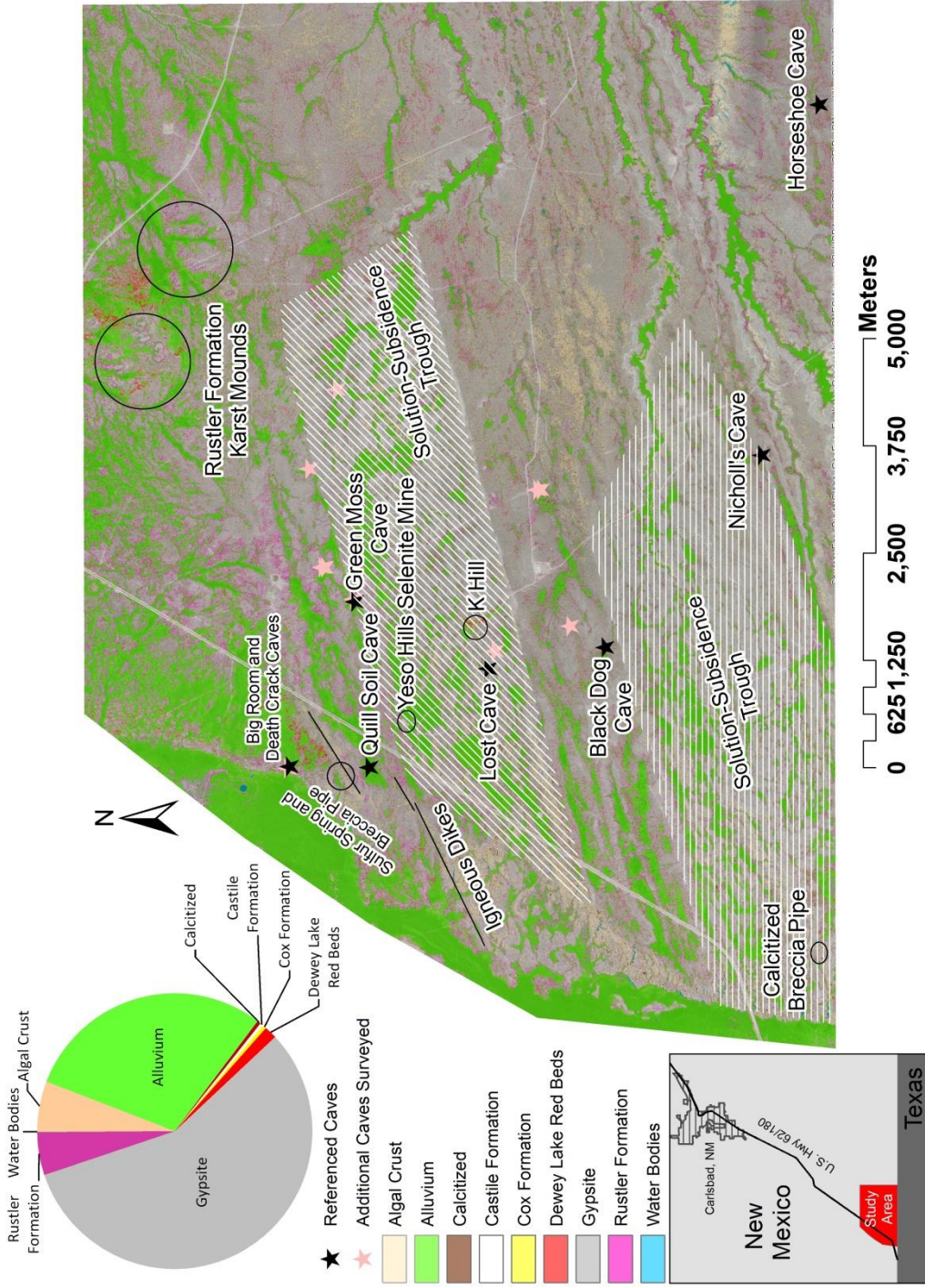


Figure 1.3: Location of features of interest within this study that correspond to the greater characteristic features of the Gypsum Plain and their relationship to the overall surface geology delineated across the site (Shields et al., submitted).

of exposed Castile bedrock surfaces are retained as surface fluids by lichens and microbial colonies, which subsequently produce gypsic crusts (Figure 1.4A) as precipitates. By similar means, gypsite is formed at the interface between gypsum bedrock and gypsic soils, as it can extend several m deep and host a variety of karst phenomena. The process of gypsite formation results in poorly consolidated, indurated soils with particles bound together by secondary gypsum precipitates derived from saturated fluids (Canton et al., 2003; Stafford, 2008b). Exposed surfaces of Castile gypsum not mantled by secondary gypsic precipitates often exhibit a variety of well-developed karren, including rillenkarren (Figure 1.4B), spitzkarren (Figure 1.4D) and kamenitzas (Stafford, 2008b).

The most common surficial karst expressions are closed depressions or sinkholes formed either by collapse of subsurface voids (Figure 1.4C) or dissolution by descending fluids. Open and filled sinkholes exist, with open sinkholes culminating in solutional conduits or cave entrances at the terminus of multi-hectare watersheds (Figure 1.4E), while collapsed sinkholes often feature steep walls of bedrock and, in plan view, a circular to elliptical shape with limited to no surface catchment. Depths and diameters of sinkholes vary across the study area from a few cm to tens of m, and filled versions commonly contain thick soil deposits which retain a higher moisture content than the surrounding areas, thus supporting more dense vegetation (Figure 1.4F) (Stafford, 2008b).



Figure 1.4: Surficial karst manifestations across the study area: A) gypic crust found across most of the study area; B) rillenkarren on exposed Castile gypsum; C) small sinkhole manifesting as a closed depression within gypic soil; D) spitzkarren developed on gypsum breccia boulder; E) sinkhole formed in gypsum bedrock of the Castile containing the entrance to Green Moss Cave; and F) grass filled sinkhole formed within gypsite, filled by Quaternary Alluvium

Residual
hills of dissolution-
collapse breccia
known as karst
mounds form
roughly circular to
elliptical positive
relief structures
across the
Gypsum Plain.



Figure 1.5. Karst mounds and areas exhibiting secondary calcitization: A) karst mounds (delineated with dashed white lines) primarily consisting Rustler strata; and B) K Hill, the largest karst mound in the study area consisting of the Rustler, Dewey Lake Red Beds and Cox strata.

These hills usually stand less than 10 m in height and tens of m in diameter, often forming a series of disconnected masses more than a km long (Bachman, 1980), which have been described as “structure-less heaps of insoluble residue” (Hill, 1996). The filling of collapsed subsurface voids and sinkholes by dissolution-collapse breccia of overlying strata and subsequent exposure due to surface denudation has formed these resistant paleokarst erosional remnants (Crawford, 1993; Hill, 1996; Vine, 1963).

Several karst mounds exist within the study area primarily consisting of residual Rustler strata capped by gypsic crust precipitates (Figure 1.5A). Rustler mounds tend to consist of more erosion resistant members of the formation, the Culebra and Magenta dolomites, with steeply sloping sides and relatively level

tops. K Hill (Figure 1.5B) is an anomalous karst mound located in the central portion of the study area that is much more complex, consisting mainly of upper Rustler and Salado formations, including matrix-supported, cobble- to boulder-size breccia clasts of Culebra and Magenta members of the Rustler. The eastern portion of K Hill is an adjacent, rotated and down-dropped karst block preserving the Dewey Lake Formation in contact with the Cox Formation. At 17 m tall, K Hill is significantly larger than other erosional remnants in the area (Crawford, 1993) and is located within one of multiple solution-subsidence troughs across the study area that form straight depressions ranging in length from 80 m to 16 km and 100 m to 1.6 km wide.

Solution-subsidence troughs are sites of localized subsurface dissolution where subsequent collapse has diverted and captured surface streams, allowing for further dissolution of adjacent areas and formation of large topographic lows, as evident today (Olive, 1957). Troughs of this type are common across the Gypsum Plain and form along northeast trending joint sets and graben fault boundaries consistent with regional Basin and Range deformation (Crawford and Wallace, 1993; Hentz and Henry, 1989). Olive (1957) postulated that the source of subsurface dissolution was the nearby aquifer of the reef escarpment, the Delaware Mountain Group aquifer, or a subsurface paleostream. Cave and karst features are common along trough scarp boundaries, as well as the occurrence

of calcitization, native sulfur and selenite bodies (e.g. Yeso Hills Selenite Mine) discussed later.

Epigene Caves

Epigene caves exist as numerous, isolated, well-developed yet laterally-limited groundwater recharge features manifesting as solutional conduits connected to incised sinkholes within the Castile outcrop. Massive, nodular and laminated gypsum fabrics have been identified to host epigene caves, as well as surficial gypsite deposits. Due to the low permeability of gypsum, fluids preferentially migrate along preexisting joint and fracture planes, resulting in strong structural passage control (Figure 1.6A) (Klimchouk, 2000a; Stafford,



Figure 1.6: Classic examples of epigene morphological features associated with gypsum caves: A) scallops lining the floor and ceiling (white circle) as well as visible dissolution within the ceiling exhibiting strong fracture control; B) Example of rapid decrease in aperture of epigene cave passage seen by the extreme drop in ceiling height over only a few m; C) Example of visible meandering of passage created by fluid flow and entrenchment along dashed lines on the lower portion of the wall.

2008b). Due to the high solubility and near-linear solution kinetics of gypsum, meteoric fluids quickly approach saturation during overland flow events across the Gypsum Plain. Therefore, fluids are often highly saturated upon entering the subsurface, thus limiting further dissolution potential and resulting in a rapid decrease in cave passage aperture/cross-sectional area (Figure 1.6B) away from cave entrances (Stafford, 2015). Rapid narrowing of passages often prevents exploration and survey of more than a few tens of m in length. Common morphological features of epigene caves include well-developed, small-scale scallops on bedrock surfaces (Figure 1.6A) and vertical entrenchment of passage floors (Figure 1.6C); indicating that formation dominantly occurs during large-scale rain events transmitting high flow volumes (Stafford, 2008b; White, 1988). Typical examples that display the variability of epigene caves within the study area include Lost Cave, Horseshoe Cave, Big Room Cave, Death Crack Cave, Quill Soil Cave and Nicholl's Cave.

Lost Cave is a typical small epigene recharge feature located within a shallow soil and bedrock sinkhole (Figure 1.7A) in the central portion of the study area, with a surveyed length and depth of 12 and three m, respectively (Figure 1.7B). The cave features extreme fracture control with a classic epigene decrease in passage size over a very short distance. In contrast, Horseshoe Cave is one of the more complex epigene caves. The entrance is formed within a massive soil and bedrock sinkhole connected to a large bedrock entrance of



Figure 1.7: Lost Cave: A) sinkhole and entrance to Lost Cave (Eddy County, New Mexico); B) simplified map of Lost Cave.

residual collapse (Figure 1.8A). The first half of the cave is classic entrenched epigene passage of relatively constant dimensions (Figure 1.8B) with regions of floor entrenchment that have undercut to induce wall collapse (Figure 1.8C), while later portions of the cave rapidly decrease in size to less than one m in diameter (Figure 1.8D) and were sumped at the time of exploration (Figure 1.8E).

Separating the Guadalupe Mountains and the Gypsum Plain is the Black River Valley (a major tributary of the nearby Pecos River), forming a gravel plain along which the solutional margin of the Castile Formation outcrop has developed. Within this gypsum escarpment, a series of epigene cave passages occur that have undergone recent catastrophic failure, today manifesting as unstable mounds of collapse, hosting extensive breakdown and unstable residual caves. These solutional margin karst features include Big Room Cave and Death Crack Cave, which form an interconnected system proximal to the escarpment where overland flow is focused as epigene recharge through the escarpment to

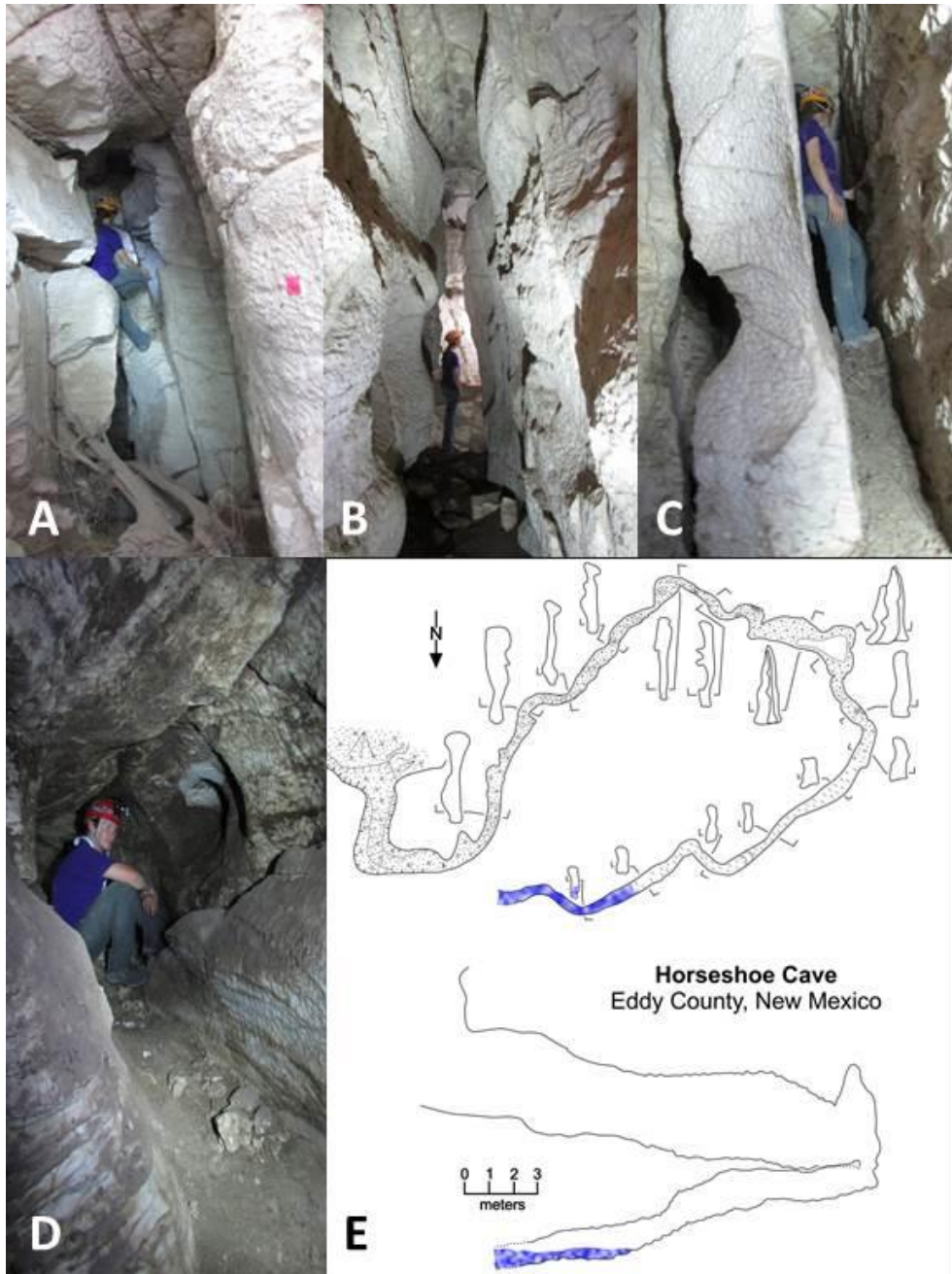


Figure 1.8: Horseshoe Cave, Eddy County: A) entrance to Horseshoe Cave and associated residual collapse; B) narrow, entrenched epigene passage forming the first half of Horseshoe Cave; C) large block of bedrock rotated in passage as result of undercutting during floor entrenchment; D) rapid decrease in passage diameter at the back of Horseshoe Cave; and E) simplified map of Horseshoe Cave.

the topographic low of the Black River Valley. The entrance to Big Room Cave is approximately 100 m distal from the solution collapse scarp and formed 15 m below its crest, with a five-m-tall headwall within a large, multi-hectare watershed. The entrance area is heavily modified by collapse but within 10 m it connects to a seven-m-diameter room approximately five m tall. The cave is formed within gypsum bedrock collapse (Figure 1.9A, B) while gypsite forms the majority of the main room's ceiling. The floor is composed of collapse material mantled with organic-rich soil excluding an unstable central floor opening through breakdown that acts to drain intense recharge events (Figure 1.9C). 35 m northwest of Big Room Cave, approximately mid-way to the scarp margin, is the entrance to Death Crack Cave (Figure 1.9D), a vertical, multi-level, solutionally-widened fracture complex located within the ridge of the gypsum escarpment. Death Crack Cave is the product of multiple episodes of collapse, with minor solutional widening as scarp erosion proximal to the Black River Valley continues to erode and destabilize the scarp margin. Sound is easily carried between the two caves through collapse material, confirming connectivity but unstable breakdown prevents physical connection.

Suffosion processes are often responsible for the creation of pseudokarst within gypsite and gypsic soil throughout the Gypsum Plain where fluid migration has produced piping features and tubular cave passages (Halliday, 2004; Palmer, 2009). Gypsite caves are often similar in scale to classic epigene

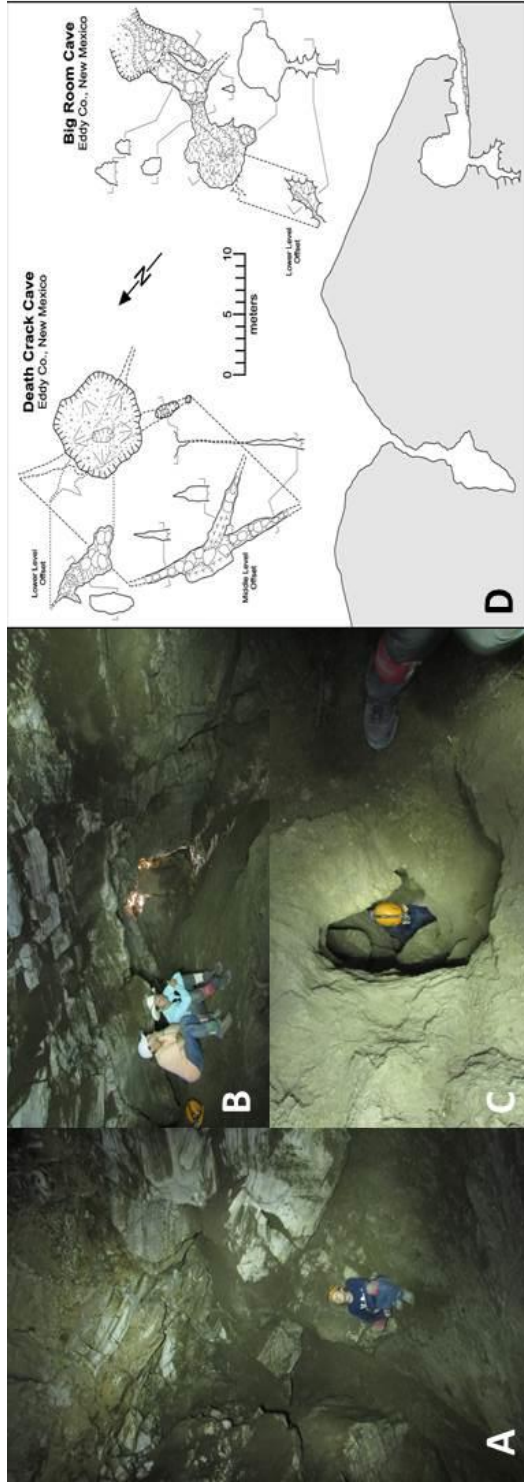


Figure 1.9: Big Room and Death Crack caves, Eddy County: A) main room of Big Room Cave showing the soil floor and collapse breccia walls and ceiling; B) main room of Big Room Cave showing the relation of the entrance to the soil floor and brecciated walls of the cave; C) vertical, mud-draped drain within the floor of Big Room Cave formed completely within loosely consolidated collapse breccia by flow of waters into the cave primarily by large-scale rain events; and D) simplified map of Big Room Cave and Death Crack Cave.

gypsum bedrock features, generally being small and laterally-limited, although usually shorter because of matrix instability—gypsite caves commonly terminate in collapse. Often, entrances are relatively small compared to typical epigene caves, and are formed adjacent to shallow sinkholes filled primarily by similar indurated gypsic soil. Quill Soil Cave (Figure 1.10A) is the largest of several gypsite caves surveyed within the study area, at 49 m long and four m deep. The cave is largely horizontal with sections approximately 10 m long that are interrupted by small collapse chambers—the cave likely extends beyond the more extensive collapsed zone at the end of the surveyed limits in a similar fashion. Generally, gypsite caves appear to transport shallow groundwater laterally above the contact with underlying gypsum bedrock and are usually associated with bedrock caves at depth (Stafford, 2008b), as illustrated by Nicholl’s Cave. Nicholl’s Cave (Figure 1.10B) exhibits a small entrance and associated room within gypsite that is connected to an epigene conduit

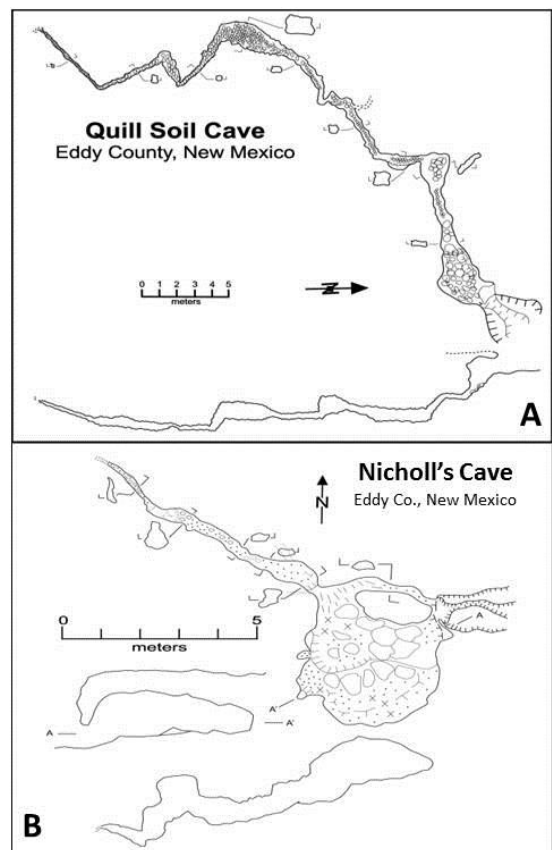


Figure 1.10: Soil caves, Eddy County: A) simplified map of Quill Soil Cave; B) simplified map of Nicholl's Cave.

passage that extends approximately 10 m before becoming narrow and largely plugged by suffosion products. Nicholl's Cave, and other similar features within the Gypsum Plain, indicate that most gypsite caves are suffosion features coupled to either bedrock conduits or solutionally-widened fractures at depth and appear to represent reactivation of karst features intermittently plugged by surficial deposits.

Hypogene Karst

While epigene karst are directly coupled to meteoric processes, hypogene cave features are formed at depth, within semi-confined zones by fluids migrating upward by both forced and free convection/brine density flow (Stafford, 2008b; Klimchouk, 2000b). Discontinuous fracture and joint sets throughout the Castile Formation initially provide limited connectivity for upward migrating fluids to penetrate otherwise impermeable formations, acting to dissolve adjacent bedrock and form void space (Stafford, 2008b). Despite this limited initial permeability, well-developed hypogene cave systems show more complex and extensive dissolution patterns than epigene caves as a result of non-competitive, solutional flow (Stafford, 2013).

Evidence of widespread hypogene processes is common across the Gypsum Plain, indicated by manifestations of the typical morphological suite of rising fluids described by Klimchouk (2007): risers, cupolas, and half-tubes.

Additionally, hypogene cave passages generally feature smooth walls or common pendent structures due to sluggish formational fluid flow. Hypogene caves exhibit small drainage areas compared to passage length, further indicating that passage development predates surficial breaching. Passages are often elliptical, rarely entrenched and increase, rather than decrease, in average aperture diameter away from entrances. Access to hypogene features requires that they must be breached by surface denudation and meteoric flow, inevitably resulting in a variable epigenic overprinting often acting to complicate speleogenetic interpretations. Overall morphological features, spatial patterns and cave extent, in relation to drainage area, are used to confidently classify features as either originating as epigenic or hypogenic, despite the degree of epigene overprinting (Stafford, 2008b).

Numerous hypogene caves have been reported across the Gypsum Plain, but Black Dog Cave, a hypogene feature in the focus areas of this study, is one of the largest and most complex that has been documented in the region, with a surveyed length of 684 m and 34 m deep. Black Dog Cave (Figure 1.11) is located at the base of a large sinkhole, filled by quaternary alluvium, and formed entirely within laminated gypsum. The cave is split into multiple levels with two dominant passage trends (northeast/southwest and northwest/southeast). The cave features numerous prominent diagnostic hypogene features, including spherical tube-like passages with ceiling half-tubes, risers and pendent

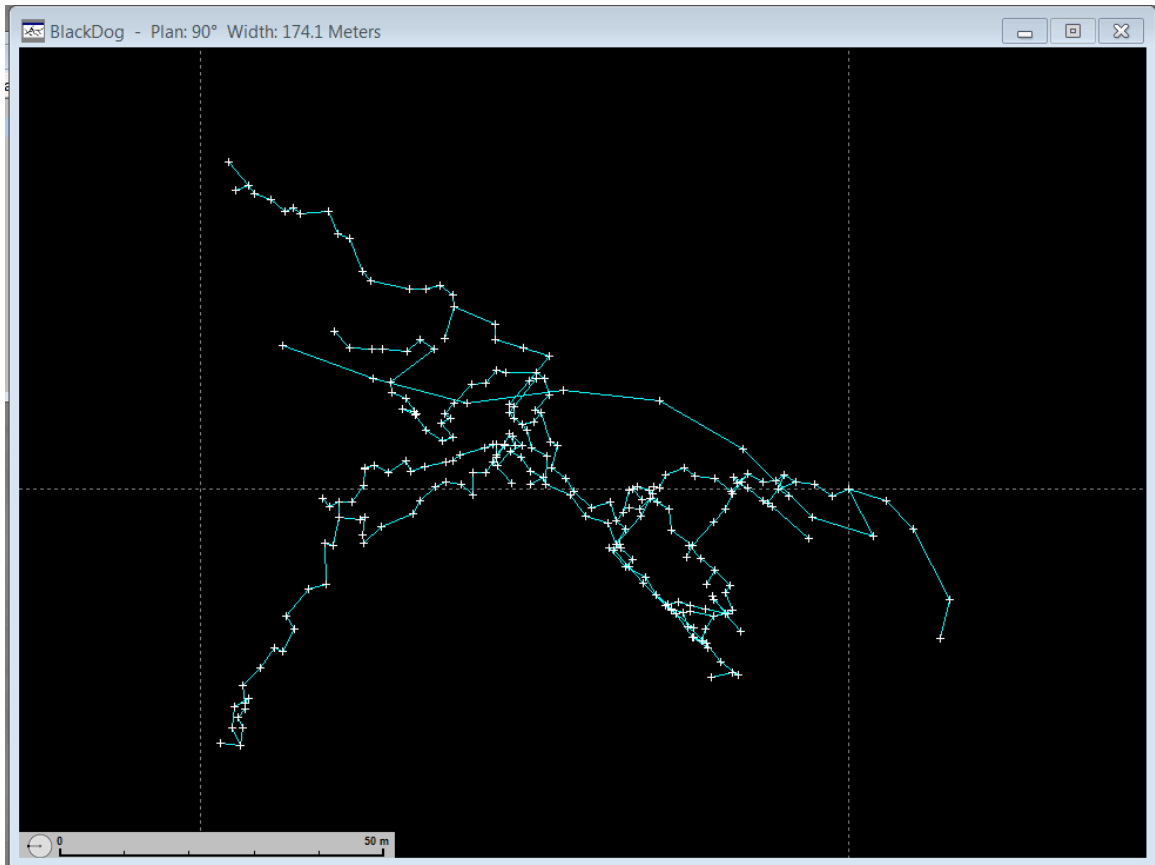


Figure 1.11: Simplified line map of Black Dog Cave (Eddy County, New Mexico).

structures. However, significant epigene overprinting has occurred, evident by areas of floor entrenchment and prolific scalloping. The complex pattern of passages, which exhibits an inverse dendritic pattern of passage divergence from the entrance, and passage morphology indicate solution conduits formed under semi-confined conditions while epigene overprinting is associated with more recent development of proximal solution-subsidence troughs.

In addition to hypogene caves, zones of solutional brecciation are common throughout the entire Castile Formation, usually manifesting either as

vertical breccia pipe structures or horizontal blanket breccias (Stafford et al., 2008a). Vertical breccia pipes are columnar bodies often penetrating hundreds of m through the subsurface within Castile, Salado, and Rustler formations across the Delaware Basin (Stafford, 2008a; Bachman, 1980; Anderson and Kirkland, 1980). Pipes may be identified at the surface either as negative relief features due to subsurface collapse or as positive relief features of previous collapse that have been heavily recemented and altered to form erosionally-resistant remnants (Bachman, 1980; Adams, 1944). These brecciated zones are paleokarst remnants where original hypogene voids at depth, most commonly originating at the basal contact of the Castile Formation with the underlying Bell Canyon aquifer, have collapsed and stopped upwards. Similarly, blanket breccias developed when undersaturated fluids migrated laterally through halite deposits inducing intrastratal dissolution to produce brecciated, residual, subangular clasts suspended in an impure matrix of anhydrite, calcite and organic matter, which was further enhanced by additional sulfate dissolution adjacent to halite horizons (Anderson et al., 1978; Anderson et al., 1972). Generally, resulting blanket breccias are usually dm to c m thick but may represent several m of vertical collapse (Stafford, 2008a).

Across the Delaware Basin, ascending fluids necessary for hypogene speleogenesis and formation of brecciated zones are commonly associated with hydrocarbon migration paths. Methane derived from the lower Delaware

Mountain Group has been found to migrate in conjunction with brine waters through Ochoan strata throughout the Delaware Basin. Formational crosscutting of faults and zones of brecciation enabled hydrocarbons to penetrate evaporite strata and supply light hydrocarbons that fueled sulfate reduction. As a byproduct, evaporites are variably calcitized and hydrogen sulfide byproducts often formed deposits of native sulfur (Kirkland and Evans, 1976; Stafford et al., 2008d); economically viable native sulfur bodies have been exploited across the Delaware Basin, usually filling vugs within brecciated, calcitized zones (Wallace and Crawford, 1992).

Calcitized zones have been attributed to bacterial sulfate reduction (BSR) (Hill, 1996) and thus are commonly termed bioepigenic limestone. It is also possible that calcitization is the product of thermal sulfate reduction (TSR) or a combination of sulfate reduction processes—current data is not conclusive as to the dominant mechanism of sulfate reduction (Stafford et al., 2008d). Calcitized zones can form lateral sheets (Figure 1.12A) or vertical structures most often associated with breccia zones. Kirkland and Evans (1976) documented calcitized breccia pipes as “Castile Buttes” forming positive surficial erosional remnants, while Adams (1944) documented subsurface calcitized



Figure 1.12: Features associated with dissolution breccias that have undergone calcitization: A) exposed area of secondary calcite as a blanket breccia; B) small Castile Buttes within the study area; C) zone of calcitization intersected during epigenic formation of Green Moss Cave; and D) calcitized zone of brecciation in Green Moss Cave.

breccia pipes as “Castile Masses”. Stafford et al. (2008d) documented more than 1,000 individual calcitized zones across the Gypsum Plain, and several of these manifest as small Castile Buttes within the focus area of this study (Figure 1.12B). Occasionally, calcitized zones are found in association with cave development, as seen in Green Moss Cave, where the main passage intersects a Castile Mass, resulting in abrupt changes in passage architecture (Figure 1.12C, D), but clearly demonstrating that much, if not most, cave development within the Gypsum Plain post-dates major calcitization.

Large selenite bodies have been characterized as hypogene sulfur ore bodies that were subsequently oxidized by oxygen-rich groundwater migration. The Yeso Hills Selenite Mine, located along the northern boundary fault of the solution-subsidence trough containing K Hill, features “high-purity, complexly interlocking, cleavable masses of selenite exposed sporadically” (Hill, 1996). Generally, areas of large accumulations of selenite crystals are in close relation to native sulfur deposits and calcitization, as is the case at Yeso Hills Selenite Mine, where significant calcitized zones and minor native sulfur are proximal, suggesting that these selenite masses are alteration products of native sulfur oxidation (Yushkin, 1969; Hill, 1996).

Along the western edge of the study area, adjacent to the Black River Valley, sulfide-rich, artesian discharge exhibits a strong fetid odor and hosts extensive white, filamentous microbial masses. The spring is located near a large

calcitized mass and selenite body and proximal to a series of basaltic dikes emplaced through Castile evaporites. The spring is located approximately 20 m above and 300 m away from the Black River Valley and features persistent, low discharge that does not appear to fluctuate in response to seasonal precipitation changes. This spring and others across the Gypsum Plain indicate that ascending fluid flow remains common within the area indicating hypogene processes remain active within the current geomorphic setting.

SPELEOGENETIC EVOLUTION

The speleogenetic evolution of the Gypsum Plain, as evidenced by analyses in this study and previous investigations of the region, is the result of multiple, complex episodes of solutional enhancement and diagenetic modification of bedrock which continues in the current climatic regime. A variety of epigene and hypogene karst features have been produced over time, as well as features that represent aspects of both processes. These karst phenomena are the result of a long and extensive history of Mesozoic burial diagenesis, Laramide compression, magmatic emplacement, Basin and Range extension and Quaternary climate change.

The collision of Gondwana and Laurasia to form Pangea, or Ouachita Orogeny led to the formation of the Delaware Basin as an intracratonic, deep water basin for Permian deposition. Series of shales, siltstones, sandstones and limestone beds were deposited within the basin during the early to mid-Permian, followed by the organic-rich siltstone to fine-grained sandstones, under- and overlain by dark limestone units, of the Guadalupian Delaware Mountain Group. Late Ochoan deposition consisted of anywhere from several hundred to 1,000 m of Castile evaporites within the Delaware Basin, followed by additional evaporites, carbonates and continental red beds of the Salado, Rustler and

Dewey Lake formations, respectively (Hill, 1996). Post-Castile deposition covered basinal facies, as well as the surrounding marginal carbonates of the fore-reef, reef and shelf for most of the following 250 million years (Kirkland, 2014), effectively isolating this region from major karst processes throughout the Mesozoic.

Major sedimentation within the basin ceased after the Permian with thin, sporadic deposition of limestones, sandstones and conglomerates associated with transgression and regression of shallow seas and fluvial processes (Hill, 1996). During periods of exposure, it is probable that erosion of exposed upper Ochoan strata occurred, but no definitive evidence has been documented indicating that this was extensive enough to penetrate Castile strata. Beyond minor solutional porosity associated with endokinetic fissuring during early burial

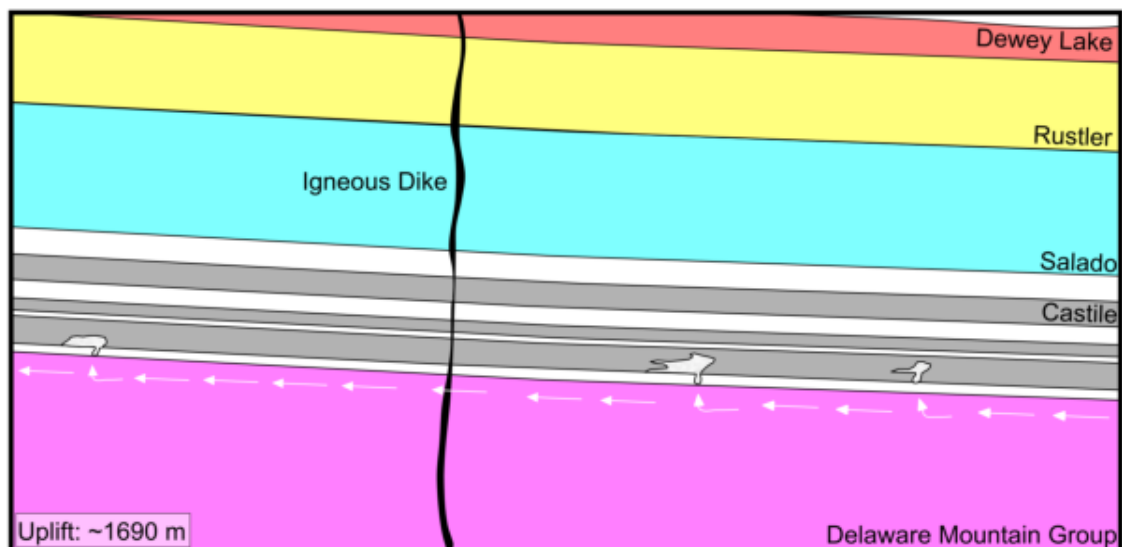


Figure 1.13: Diagram depicting the uplift and tilting experienced by the Delaware Basin tectonic block due to tectonic activity originating at the Rio Grande Rift during the early late Miocene.

and associated sulfate fabric alteration (Dean et al., 1975; Klimchouk and Andrejchuk, 1996; Stafford, 2008b), speleogenetic phenomena observed across the Gypsum Plain today most likely did not form until the late Miocene.

Uplift and tilting of the Delaware Basin tectonic block, due to Basin and Range deformation of the Rio Grande Rift west of the Delaware Basin, is thought to have begun in the early late-Miocene (Figure 1.13), with an additional intense pulse occurring again 6-4 million years ago (Figure 1.14), during the latest Miocene-earliest Pliocene (Kirkland, 2014; Lueth et al., 2005; Lindsay, 1998; DuChene and Cunningham, 2006). These values are based on radiometric dating of alunite ($^{40}\text{Ar}/^{39}\text{Ar}$) from a series of major caves within the adjacent Guadalupe Mountains corresponding to episodes of cave enlargement at these times (Polyak et al., 1998; Polyak and Provencio, 2000; Kirkland, 2014).

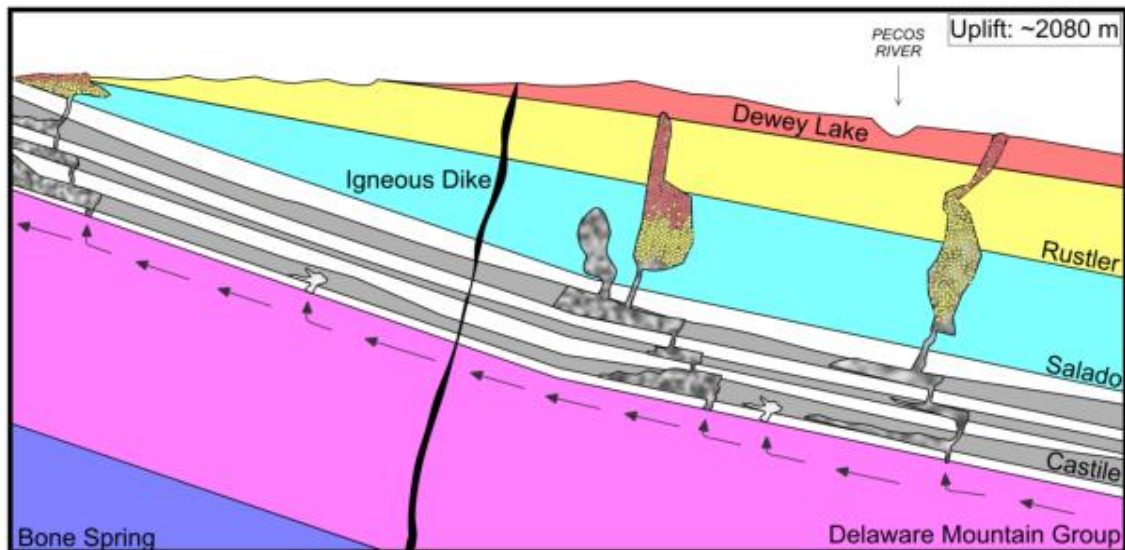


Figure 1.14: Diagram depicting the second pulse of uplift and tilting experienced by the Delaware Basin tectonic block during the late Miocene.

Episodes of increased regional speleogenesis are the byproduct of rapid uplift, allowing for correlation of similar results obtained through the same radiometric dating of alunite deposits along the southern Rio Grande Rift (Lueth et al., 2005; Seager and Morgan, 1979). Tilting induced the flow of groundwater down-dip to the east-northeast, originating from the uplifted Guadalupe Mountains area along the western margin of the basin and resulting in recharge of artesian aquifers located in pre-Ochoan strata, including the Delaware Mountain Group (King, 1948; Kirkland and Evans, 1976; Kirkland, 2014; Lindsay, 1998; DuChene and Cunningham, 2006). Free convection due to differences in brine density, as well as high aquifer pressure heads, promoted the upward migration of fluids from the Delaware Mountain Group aquifer along fractures and joint sets within the overlying Castile's basal Anhydrite I Member (fracturing and joint sets are largely due to the Cenozoic uplift and tilting of the basin and reef margin). Fluid migration resulted in caverns formed by extensive, localized, hypogene dissolution at the lower Castile contact that became large enough to collapse and stope upwards to create vertical dissolution pipes through Castile strata (Anderson, 1981; Kirkland, 2014; Anderson and Kirkland, 1980). Rising, unsaturated fluids moved along fractures and joints, dissolved adjacent host rock, became saturated by salt dissolution and the resultant density increase forced fluids to sink back down into lower clastic strata beneath the Castile

Formation to be replaced by unsaturated, rising fluids (Anderson and Kirkland, 1980).

Eventually, rising hypogene fluids completely penetrated the Anhydrite I Member to contact the Halite I Member of the Castile Formation. The higher solubility of the sodium chloride led to an increase in dissolution rates and free convection, allowing rapid acceleration of upward migration. The overlying Anhydrite II Member of the Castile was virtually impermeable, except by migration along similar joint sets as seen in the Anhydrite I Member, and in most areas acted to block further vertical migration. Rising fluids were forced to migrate laterally along the base of the Anhydrite II Member, forming horizontal chambers as fluids convected up dip to the west before growing saturated with respect to sodium chloride, too dense for continued dissolution, and returned to deeper levels through density convection via flow down dip to the east (Kirkland, 2014; Anderson and Kirkland, 1980). Hypogene dissolution, intrastratal blanket breccias and vertical dissolution pipes continued to develop and stope upwards repeatedly to encounter subsequent Halite and Anhydrite Members of the Castile over time (Anderson and Kirkland, 1980; Kirkland and Evans, 1976; Stafford, 2008b; Stafford, 2008d).

Large scale collapse has been recorded along dissolution horizons between Castile members, due to extensive localized dissolution, such as Big Sinks depression, 55 km northeast of the study area. Big Sinks has been

characterized as an “eastward-advancing dissolution front where down dip-moving water has produced extensive dissolution at horizons in the Castile and Salado formations (Hill, 1996; Anderson, 1982). Vertical collapse pipes extensive enough to incorporate late Ochoan rock (e.g. Rustler strata) into Castile breccia zones have been identified, indicating extensive, repetitive collapse structures. Due to the presence of Cretaceous Cox strata and the vast size of K Hill, it is likely that collapse associated with breccia pipes in the Gypsum Plain began to occur soon after, or penecontemporaneously with, uplift and tilting which initiated upward migration of fluids. Multiple, discontinuous episodes of collapse and subsidence associated with upward breaching of Castile anhydrite members were induced over time. Rustler karst mounds that are less extensive than K Hill likely formed at the same time but represent smaller-scale, vertical, pipe structures. As collapse material associated with breccia pipes, and the residual hills evidenced in the Gypsum Plain today, continued, further dissolution dissolved intermediate evaporite strata within the Rustler Formation allowing Magenta dolomite to lie directly above Culebra dolomite in contact with lower Castile gypsum (Hill, 1996), as seen at the Rustler karst mounds.

The period of volcanism, coincident with the shift from Laramide compression to Basin and Range extension during the late Eocene to mid-Oligocene marked an increase in the regional geothermal gradient (Price and Henry, 1985; Hill, 1996). Crustal thinning allowed plutons to rise to the surface,

evident today as northeast trending dikes across the northwestern portion of the basin. The emplacement of dikes thermally altered the surrounding area and likely influenced subsurface fluid flow as a barrier or drainage structure and likely introduced juvenile waters into the system (Custodio, 2007; Ernst, 2014; Comte et al., 2017). Evidenced by alteration of igneous dikes in outcrop, they most likely became fluid migration pathways due to fracturing of host rock during emplacement and cooling (Singhal and Gupta, 1999; Bromley et al., 1994; Sami and Hughes, 1996; Wilkes et al., 2004; Vittecoq et al., 2015; Comte et al., 2017). Transient heating further increased due to Basin and Range extension until it reached latest Miocene peak values, coincident with a second major phase of uplift and tilting (Kirkland, 2014; Hill, 1996). Increased late Neogene geothermal gradients are widely considered as the source of methane generation associated with calcitization of Castile Buttes/Masses and brecciated zones, as well as sulfur ore emplacement (Kirkland and Evans, 1976; Stafford, 2008d; Kirkland, 2014; Hill, 1996). Castile Buttes, massive selenite deposits and a sulfur mineral spring are located proximal to the series of igneous dikes, suggesting TSR may have been more dominant than BSR processes associated with calcitization within the Gypsum Plain.

A second phase of hypogene karstification would have also been initiated with peak heat values and the second pulse of uplift and tilting, as well as hydration of shallow anhydrite and oxidation of near surface sulfur deposits to

form large concentrations of selenite in outcrop. As more oxygen-rich groundwater recharged surficial exposures of clastics within the Delaware Mountains, higher pressure heads were induced and introduced into the western portions of the Delaware Basin, further occluding pore structures within calcitized regions and promoting additional hypogene cave development.

It is likely that Black Dog Cave was formed during this second episode of renewed hypogene activity due to the largely intact nature of the cave. Most largely intact hypogene caves within the Gypsum Plain commonly have portions of passage development that cut across calcitized zones and often through selenetic masses. This suggests that the second pulse of hypogene cave formation likely occurred during the Pliocene, as permeability decreases induced by extensive calcitization within older hypogene-induced brecciated zones began to occlude vertical and lateral permeable zones previously established through the Castile Formation.

The Pleistocene was a time of major surface denudation and epigene cave development across the Gypsum Plain (Figure 1.15). The climate transitioned from semi-arid to arid conditions of middle to late Miocene to a fluctuation between colder, wetter glacial periods and warmer, drier interglacial periods, evidenced by various isotope data (Bachman, 1980; Hill, 1996; Hill, 1987; Harris, 1985; Van Devender, 1980). Glacial periods resulted in rapid erosion and dissolution of Permian strata, with the middle Pleistocene (during the

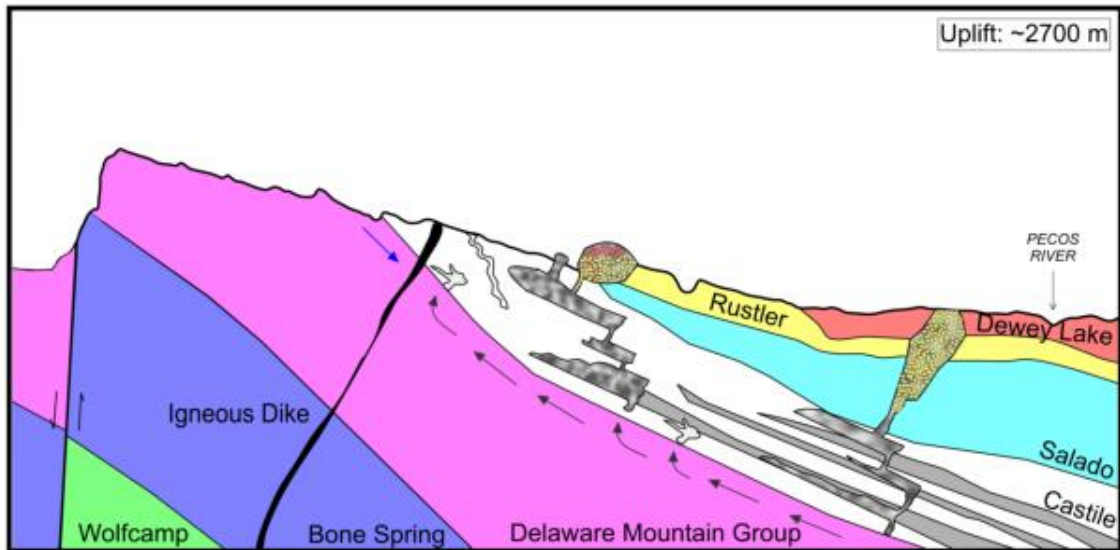


Figure 1.15: Diagram depicting the beginning of epigene cave formation and denudation of the Gypsum Plain induced by the higher moisture contents of glacial periods occurring during the Pleistocene.

Kansan glacial, ~600,000 to 800,000 ybp) being the most humid period and likely time of greatest surface denudation (Hill, 1996). Epigene cave features, such as Lost Cave, Horseshoe Cave and Green Moss Cave, began to form with denudation of the Gypsum Plain and increased overland flow coupled with shallow vadose dissolution. Pleistocene timing of major epigene cave development is further evidenced by development of passages through brecciated/calcitized zones, as in Green Moss Cave and similar to that observed in hypogene caves. Most of the hypogene caves currently documented across the Gypsum Plain were likely intercepted at this time by surface denudation and epigene overprinting began.

Migration of the Pecos River across the Delaware Basin from early Paleogene to today resulted in concentrated fluid flow toward this potentiometric

low (Thomas, 1972; Stafford, 2008d). Solution-subsidence troughs across the basin likely formed as a result of directional flow towards the migrating potentiometric low of the Pecos River during the late Pleistocene, causing intense areas of localized dissolution, leading to collapse and infilling by Quaternary sediments (Stafford, 2009; Malley and Huffington, 1953; Olive, 1957), contemporaneous with epigene karst development. The solution troughs of K Hill and Yeso Hills Selenite Mine began to experience increased dissolution as the Pecos River migrated east across the Gypsum Plains. Once the Pecos River was established within its current location by the end of the Neogene (Thomas, 1972) and the Black River began to develop as a tributary along the base of the Guadalupe Mountains, caves and associated collapse structures found along the escarpment delineating the solutional edge of the Gypsum Plain evolved with continued degradation of the updip margin of Castile strata.

During the last 10,000 years (Figure 1.16), Holocene climate in the Delaware Basin has shifted to arid/semiarid conditions (Hill, 1996), with associated infilling of many Pleistocene-formed sinkholes with alluvium/gypsic soil. Heavy precipitation events, such as those experienced during modern monsoonal seasons, produce karren within the current landscape on exposed bedrock surfaces as well as aiding in the development of gypsic crusts. Pseudokarst/gypsite caves have formed most recently in association with these intense storm events that induce soil piping and re-activation of soil-

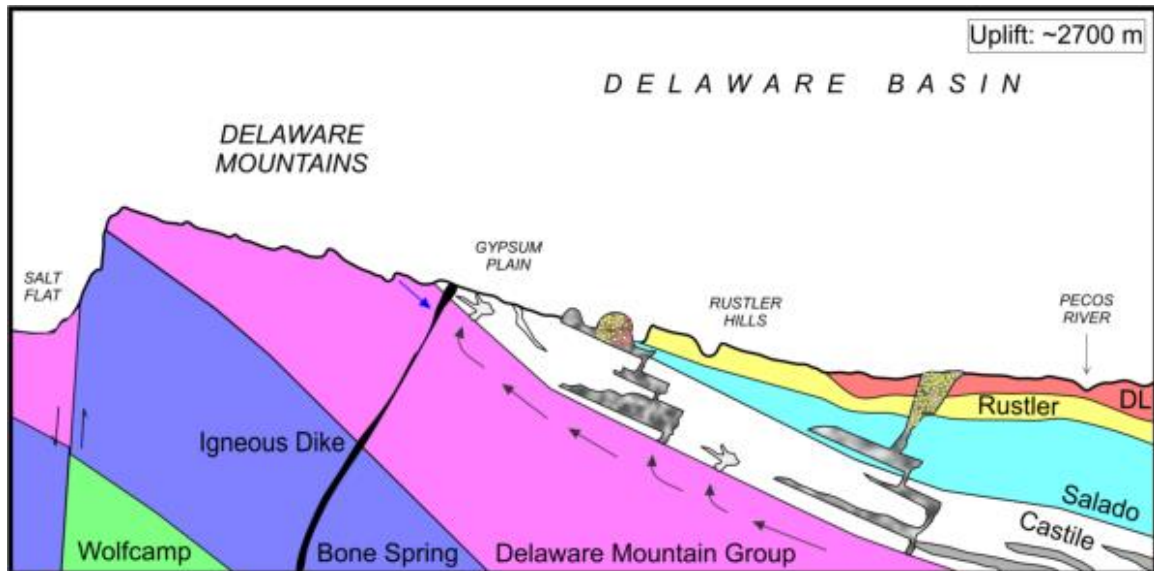


Figure 1.16: Diagram depicting the present day state of the Gypsum Plain through the Holocene. plugged/buried karst features. Sulfide-rich springs indicate that localized hypogene processes are still active in the Gypsum Plain, while epigene, and breached hypogene, caves continue to evolve.

The prominence of hypogene diagenetic patterns and manifestations across the Gypsum Plain indicates that hypogene speleogenesis is the dominant process that has affected the speleogenetic evolution of the area (Stafford, 2008a; 2008b). Continued migration of fluids along the dip of the Gypsum Plain allow for further hypogene dissolution and sulfate diagenesis to continue to form today with the migration of the Castile dissolution front to the east (Stafford, 2008d). Precipitation events, erosion and eolian processes have caused infilling of many voids and sinkholes with sediments during the Holocene; however, many of these features appear to be ephemerally active as soil/sediment obstructions at surficial interfaces are intermittently opened and closed. Many

features are undergoing various stages of fill, while subsequent remobilization of sediments is allowing for equilibration of the systems and reopening of previously blocked flow paths. Holocene processes are still active across the Gypsum Plain today, experiencing increasing and decreasing rates depending on the level of moisture and precipitation experienced and resulting in the formation of karren, gypsic crusts, gypsite, suffosion caves, epigene caves and variable solutional overprinting at a slower pace than wetter climates of the Pleistocene.

CONCLUSIONS

The large variety of karst features evident across the Gypsum Plain today are the result of a combination of complex hydrogeologic, tectonic and climate related processes primarily occurring within the last 10 million years. The speleogenetic system continues to evolve today, but based on current analyses of karst phenomena, major speleogenetic processes began in the Miocene, associated with the following speleogenetic sequence.

- Crustal extension due to the shift from Laramide compression to Basin and Range extension allowed for the rise of plutons to upper crustal levels across the Gypsum Plain during the mid-Oligocene, with brittle deformation and increased geothermal heating (e.g. igneous dike emplacement).
- Major uplift and tilting of the Delaware Basin tectonic block began as a result of Basin and Range deformation of the Rio Grande Rift in the early-late Miocene exposing updip portion of the far western Delaware Basin to surficial processes (Figure 1.13).
- Tilting induced migration of unsaturated water from the Delaware Mountain Group Aquifer upward via joints/faults within members of the Castile strata resulting in dissolution of salt beds to form early

phases of hypogene caves as well as vertical and lateral breccia zones (e.g. K Hill, Rustler karst mounds) (Figure 1.13).

- The regional geothermal heat gradient reached peak values (originally spurred by emplacement of Oligocene dikes and increased due to transient heating associated with Basin and Range deformation) during the latest Miocene, promoting maturation of hydrocarbons.
- A second intense pulse of uplifting and tilting in the latest Miocene-earliest Pliocene resulted in renewed karstification accompanied by light hydrocarbon (methane) migration that fueled calcitization and sulfur ore emplacement largely within calcitized zones (e.g. Castile Buttes, calcitized breccia blankets) (Figure 1.14).
- Pliocene exposure of clastics within the Delaware Mountains introduced oxic waters into the Delaware Mountain Group that induced oxidation of shallow sulfur ore deposits to selenite and a second phase of hypogene cave development induced by porosity occlusion of previous permeable breccias during calcitization (e.g. Black Dog Cave).
- Pleistocene shifts to more humid climates induced significant surface denudation, epigene cave development and breaching of hypogene caves (e.g. Lost Cave, Horseshoe Cave) (Figure 1.15).

- Pecos River migration during the Neogene created intense areas of localized dissolution and collapse due to preferential fluid flow toward the potentiometric low of the river (e.g. solution-subsidence troughs).
- Development of the Black River Valley along the western margin of the study area, induced karst development through destabilization and collapse along the solutional margin of the Castile outcrop area throughout the Holocene (e.g. Big Room Cave, Death Crack Cave and associated epigene features).
- Holocene shift to the warm, arid climate of the Delaware Basin today led to continued, although reduced, epigene karst development and denudation coupled with significant infilling of Pleistocene sinkholes with alluvium/gypsic soil (e.g. karren, gypsic crusts, gypsite, Quill Soil Cave, Nicholl's Cave) (Figure 1.16).

Karst processes initiating in the Miocene in the Gypsum Plain are likely occurring with the central Delaware Basin today while hypogene cave breaching and epigene karst development continue slowly with eastward migration of surface denudation throughout the Delaware Basin. Future studies in the region will continue to refine and restrain the timing of speleogenetic processes within the Gypsum Plain as this complex hydrogeologic system is better characterized.

REFERENCES

- Adams, J. E. (1944). Upper Permian Ochoa Series of Delaware Basin, West Texas and southeastern New Mexico. *Am. Assoc. Petroleum. Geol. Bull.*, 28, 1596-1625.
- Anderson, R.Y. (1981). Deep seated salt dissolution in the Delaware Basin. *In* Wells, S.G. and Lambert, W. (eds.), *Environmental geology and hydrology in New Mexico*. New Mexico Geological Society.
- Anderson, R.Y. (1982). Deformation- dissolution potential of bedded salt, Waste Isolation Plant site, Delaware Basin, New Mexico; *in* Lutze, W. (ed.), *Scientific Basis for Radioactive Waste Management*. New York, New York: Elsevier Science Publ. Co.
- Anderson, R. Y., Dean, W. E., Kirkland, D. W. and Snider, H. I. (1972). Permian Castile varved evaporite sequence, West Texas and New Mexico. *Geological Society of America*, 83, 59-85.
- Anderson, R. Y., Kietzke, K. K. and Rhodes, D.J. (1978). Development of dissolution breccias, northern Delaware Basin and adjacent areas. Socorro, New Mexico: *New Mexico Bureau of Mines and Mineral Resources*. 47-52.
- Anderson, R. Y. and Kirkland, D. W. (1980). Dissolution of salts by brine density flow. *Geology*, 8, 66-69.
- Bachman, G. O. (1980). Regional geology and Cenozoic history of Pecos Region, Southeastern New Mexico. *U.S. Geol. Surv.*, Open-file Rept. 116, 80-1099.

- Bromley, J., Mannstrom, B., Nisca, D. and Jamtlid, A. (1994). Airborne geophysics: Application to a ground-water study in Botswana. *Ground Water*, 32(1), 79–90.
- Canton, Y., Sole-Benet, A. and Lazaro, R. (2003). Soil geomorphology relations in gypsiferous materials of the Tabernas Desert (Almeria, SE Spain). *Geoderma*. 115(3-4), 193-222.
- Comte, J-C., Wilson, C., Ofterdinger, U. and González-Quirós, A. (2017). Effect of volcanic dykes on coastal groundwater flow and saltwater intrusion: A field-scale multiphysics approach and parameter evaluation. *Water Resources Research*, 53(3), 2171-2198.
- Crawford, J.E. (1993). K Hill and Yeso Hills selenite occurrence. *In* Love, D.W., Hawley, J.W., Kues, B.S., Adams, J.W., Austin, G.S., and Barker, J.M. (Eds.), *Carlsbad Region*. New Mexico Geol. Society. 8-10.
- Crawford, J.E. and Wallace, C.S. (1993). Geology and mineralization of the Culberson sulfur deposit. *In* Love, D.W. et al. (eds.), *Carlsbad region, New Mexico and West Texas*. New Mexico Geological Society Guidebook, 44th Annual Field Conference, 301-316.
- Custodio, E. (2007), Groundwater in volcanic hard rocks. *In* Krasny, J. and Sharp Jr, J.M. (eds.) *Groundwater in Fractured Rocks*, IAH Selec. Pap. Ser., 9. London, United Kingdom: Taylor and Francis.
- Dean, W.E., Davies, G.R. and Anderson, R.Y. (1975). Sedimentological significance of nodular and laminated anhydrite. *Geology*, 3, 367-372.
- Dickenson, W.R. (1981). Plate tectonic evolution of the southern Cordillera. *Arizona Geological Society Digest*, 14, 113-135.
- Du Chene, H.R. and Cunningham, K.I. (2006). Tectonic influences on speleogenesis in the the Guadalupe Mountains, New Mexico and Texas. *In* Land, L., Lueth, V.W., Raatz, W., Boston, P. and Love, D.L. (eds.),

Caves and karst of southeastern New Mexico. Midland, Texas: New Mexico Geological Society.

- Ernst, R. E. (2014). *Large Igneous Provinces*. Cambridge, U. K.: Cambridge Univ. Press.
- Halliday, W. R. (2004). Piping caves and badlands pseudokarst. In J. Gunn (Ed.), *Encyclopedia of caves and karst science*. New York, New York: Fitzroy Dearborn. 589-593.
- Harris, A.H. (1985). *Late Pleistocene vertebrate paleoecology of the west*. Austin, Texas: University of Texas Press.
- Henry, C.D. and Price, J.G. (1985). Summary of the tectonic development of Trans-Pecos Texas. *Bur. Econ. Geol.*,
- Hentz, T.F. and Henry, C.D. (1989). Evaporite-hosted native sulfur in Trans-Pecos Texas: relation to the late phase Basin and Range deformation. *Geology*, 17, 400-403.
- Hendrickson, G.E. and Jones, R.S. (1952). Geology and groundwater resources of Eddy County, New Mexico. *New Mexico Bureau of Mines and Mineral Resources*, Groundwater Report 3.
- Hill, C.A. (1987). Geology of Carlsbad Caverns and other caves in the Guadalupe Mountains, New Mexico and Texas. In *New Mexico Bureau of Mines and Mineral Resources Bulletin 117*.
- Hill, C. A. (1996). *Geology of the Delaware Basin, Guadalupe, Apache, and Glass Mountains: New Mexico and West Texas*. Midland, Texas: Permian Basin Section of the SEPM.
- King, P.B. (1948). Geology of the Southern Guadalupe, Texas. *United States Geological Survey*. Professional Paper 215. 183.

- Kirkland, D. W. and Evans, R. (1976). Origin of limestone buttes, Gypsum Plain, Culberson County, Texas: *American Association of Petroleum Geologists Bulletin*, 60, 2005-2018.
- Kirkland, D.W. (2014). Role of hydrogen sulfide in the formation of cave and karst phenomena in the Guadalupe Mountains and western Delaware Basin, New Mexico and Texas. *National Cave and Karst Research Institute, special paper 2*.
- Klimchouk, A. (2000a). Speleogenesis in gypsum. In: Klimchouk, A., Ford, D. C., Palmer, A. N. & Dreybrodt W. (Eds.) *Speleogenesis: evolution of karst aquifers*. Huntsville: National Speleological Society.
- Klimchouk, A. (2000b). Speleogenesis under deep seated and confined conditions. In Klimchouk, A., Ford, D. C., Palmer, A. N. and Dreybrodt W. (Eds.), *Speleogenesis: evolution of karst aquifers*. Huntsville, Texas: National Speleological Society. 244-260.
- Klimchouk, A. (2007). *Hypogene Speleogenesis: Hydrogeological and Morphogenetic Perspective*. Carlsbad: National Cave and Karst Research Institute.
- Klimchouk, A. and Andrejchuk, V. (1996). Breakdown development in cover beds, and landscape features induced by intrastratal gypsum karst. *International Journal of Speleology*, 35(3-4), 127-144.
- Lindsey, R.F. (1998). Meteoric recharge, displacement of oil columns and the development of residual oil intervals in the Permian Basin. In DeMis, W.D. and Nelis, M.K. (eds.), *The search continues into the 21st century*. Midland, Texas: West Texas Geological Society.
- Lueth, V.W., Rye, R.O. and Peters, L. (2005). "Sour gas" hydrothermal jarosite: ancient to modern acid-sulfate mineralization in the southern Rio Grande Rift. *Chemical Geology*, 215, 339-360.

- Machel, H.G. and Burton, E.A. (1991). Burial-diagenetic sabkha like gypsum and anhydrite nodules. *Journal of Sedimentary Petrology*, 61(3), 394-405.
- Maley, V.C. and Huffington, R.M. (1953). Cenozoic fill and evaporite solution in the Delaware Basin, Texas and New Mexico. *Geological Society of America*, 64, 539-546.
- Olive, W.W. (1957). Solution-subsidence troughs, Castile Formation of Gypsum Plain, Texas and New Mexico. *Geol. Soc. Am., Bull.*, 68, 351-358.
- Palmer, A. (2009). *Cave Geology*. R. A. Watson (Ed.) Lawrence, KS: Cave Books.
- Polyak, V.J. and Provencio, P.P. (2000). Summary of the timing of sulfuric-acid speleogenesis for Guadalupe caves based on ages of alunite. *Journal of Cave and Karst Studies*, 62(2), 72-74.
- Polyak, V.J., McIntosh, W.C., Guven, N. and Provencio, P. (1998). Age and origin of Carlsbad Caverns and related caves from $40\text{Ar}/39\text{Ar}$ of alunite. *Science*, 249, 1919-1922.
- Price, J.G. and Henry, C.D. (1985). Summary of Tertiary stress orientation and tectonic history of Trans-Pecos Texas. In Dickerson, P.W. and Muehlberger, W.R. (eds.), *Structure and tectonics of Trans-Pecos Texas*. Texas: West Texas Geological Society. Guidebook Publ. 85(81).
- Sami, K. and Hughes, D.A. (1996). A comparison of recharge estimates to a fractured sedimentary aquifer in South Africa from a chloride mass balance and an integrated surface- subsurface model. *Journal of Hydrology*, 179(1), 111-136.
- Scholle, P.A., Goldstein, R.H. and Ulmer-Scholle, D.S. (2004). *Classic upper Paleozoic reefs and bioherms of west Texas and New Mexico*. New Mexico Institute of Mining and Technology.

- Seager, W.R. and Morgan, P. (1979). The Rio Grande Rift in southern New Mexico, west Texas and northern Chihuahua. *In* Riecker, R.E. (ed.), *Rio Grande Rift, tectonics and magmatism*. Washington, D.C.: American Geophysical Union.
- Singhal, B. B. S. and Gupta, R. P. (1999). *Applied Hydrogeology of Fractured Rocks*. Dordrecht, Netherlands: Kluwer.
- Stafford, K. W. (2013). Evaporite Karst and Hydrogeology of the Castile Formation: Culberson County, Texas and Eddy County, New Mexico. *National Cave and Karst Research Institute*. 13th Sinkhole Conference. Symposium 2.
- Stafford, K.W. (2015) Evaluation of Existing Geologic Conditions along RM 652: Initial Characterization of Karst Geohazards Associated with RM 652 in Culberson County, Texas. TxDOT Rep.1–71.
- Stafford, K.W., Brown, W.A., Ehrhart, J.T., Majzoub, A.F. and Woodard, J.D. (2017). Evaporite karst geohazards in the Delaware Basin, Texas: review of traditional karst studies coupled with geophysical and remote sensing characterization. *International Journal of Speleology*, 46(2), 169-180.
- Stafford, K. W., Land, L., & Klimchouk A. (2008a). Hypogenic speleogenesis within Seven Rivers Evaporites: Coffee Cave, Eddy County, New Mexico. *Journal of Cave and Karst Studies*, 70(1), 47-61.
- Stafford, K. W., Nance, R., Rosales-Lagarde, L. and Boston, P. J. (2008b). Epigene and hypogene gypsum karst manifestations of the Castile Formation: Eddy County, New Mexico and Culberson County, Texas, USA. *International Journal of Speleology*. 37(2). 83-98.
- Stafford, K. W., Rosales-Lagarde, L. and Boston, P. J. (2008c). Castile evaporite karst potential map of the Gypsum Plain, Eddy County, New Mexico and Culberson County, Texas: A GIS methodological comparison. *Journal of Cave and Karst Studies*, 70(1). 35-46.

- Stafford, K. W., Ulmer-Scholle, D. & Rosales-Lagarde, L. (2008d). Hypogene calcitization: Evaporite diagenesis in the Western Delaware Basin. *Carbonates and Evaporites*, 23(2), 89-103.
- Thomas, R.G. (1972). The geomorphic evolution of the Pecos River system. *Baylor Geological Studies*, 22, 1-40.
- Van Devender, T.R. (1980). Holocene plant remains from Rocky Arroyo and Last Chance Canyon, Eddy County, New Mexico. *The Southwestern Naturalist*, 25, 361-372.
- Vine, J. D. (1963). Surface geology of the Nash Draw Quadrangle, Eddy County, New Mexico. *U.S. Geol. Surv., Bull.*, 1141-B, B1 to B46.
- Vittecoq, B., Reninger, P.A., Violette, S., Martelet, G., Dewandel, B. and Audru, J.C. (2014). Heterogeneity of hydrodynamic properties and groundwater circulation of a coastal andesitic volcanic aquifer controlled by tectonic induces faults and rock fracturing—Martinique Island (Lesser Antilles – FWI). *Journal of Hydrology*, 529, 1041-1059.
- Watson, A. (1982). The Origin, Nature and Distribution of Gypsum Crusts in Desert. D.Phil, Univ. of Oxford.
- Wallace, C.S. and Crawford, J.E. (1992). Geology of the Culberson Ore Body. In Wessel, G.R. and Wimberly, B.H. (Eds.), *Native sulfur—Developments in geology and exploration*. Phoenix, Arizona: Society of Mining and Metallurgy Exploration.
- White, W. B. (1988). *Geomorphology and hydrology of karst terrains*. New York, New York: Oxford University Press.
- Wilkes, S.M., Clement, T.P. and Otto, C.J. (2004). Characterization of the hydrogeology of the Augustus River catchment, Western Australia. *Hydrogeology Journal*, 12(2), 209-223.

Yushkin, N.P. (1969). The metastomatic type of native sulfur deposits and its place in the general scheme of catagenesis. Izdatel'stvo "Nedra". 36-64.

A Novel Approach to Delineating Lithologic Variability of a Karsted Landscape Utilizing CIR Imagery and GIS Analyses, Eddy County, New Mexico

ABSTRACT

Traditional characterization of karsted terrains involves costly field studies that require months, if not years, of physical field mapping and data collection in order to complete, which can be made more efficient by the preliminary identification of areas of interest through careful analysis of geologic maps. Karst features of the Gypsum Plain of southeastern New Mexico and West Texas range from dm to tens of m in scale, requiring highly detailed maps in order to be of use. However, maps of the area currently available feature little to no detail of lithologic variability or mineralization. Advances in remote sensing technologies allow for the production of geologic maps from satellite imagery, most often based on hyperspectral data, due to an increased ability in mineral identification. However, commercially available hyperspectral sensors offer extremely low spatial resolution compared with the 50 cm resolution multispectral data available, as well as being more costly and difficult to process. The following novel approach to delineating detailed lithologic variability of a landscape may be employed through the performance of a maximum likelihood classification of

color infrared imagery. WorldView-2 satellite imagery was used in this study for its high 50 cm spatial resolution, in order to provide a more efficient and cost effective method of karst identification and lithologic characterization for use in research and natural resource management. Based on comparison with control points acquired in the field and extensive a priori knowledge of the study area, results were deemed highly accurate and are currently being used to aid in ongoing karst studies.

INTRODUCTION

Traditional characterization of karsted terrains entails the costly, time-consuming process of physical field mapping in order to identify and collect data concerning landscape features. Consequentially, remote sensing methodologies are actively being pursued as a more cost effective means of resource management. The Gypsum Plain of southeastern New Mexico and West Texas is the site of extensive karst development within Permian evaporite facies, hosting variable karst manifestations ranging in scale from mm to km (Stafford, 2008a). Specific features are often associated with unique lithologies or topographic features, allowing for preliminary identification through the use of surficial geologic maps. However, existing geologic maps of the area have poor resolution, featuring the general expected lithology with little detail and no variation in mineralogy (Figure 2.1). Advances in satellite imaging technology have allowed for the possibility of land mapping and feature extraction to be performed by image classification of raster cells based on their corresponding radiometric properties, often reducing the need for extensive groundwork while allowing for coverage of greater areas (Hamideh, 2014).

Commonly, hyperspectral data is used in studies concerning the delineation of surface geologic materials due to increased spectral resolution and

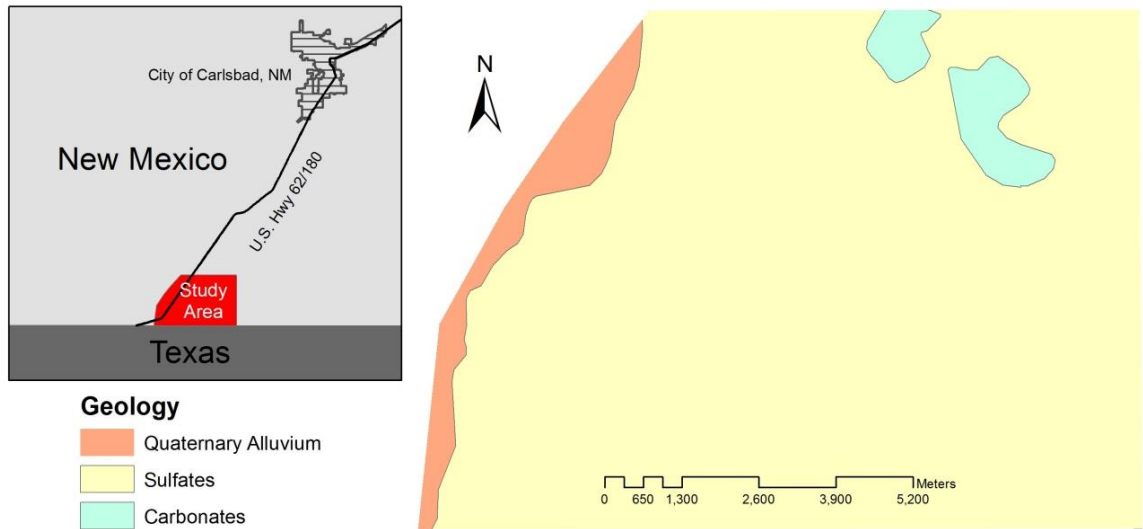


Figure 2.1: Traditional geology map of the study area created on a small-scale of 1:500,000 (adapted from Green and Jones, 1997).

number of channels with extremely narrow bandwidths, allowing for greater accuracy in the identification of specific mineral types (Harris et al., 2011).

However, commercially-available hyperspectral sensors lack refined spatial resolutions necessary in the identification of small karst features and lithologic variability (less than a few m² in size) across a landscape, while commercially-available, multispectral sensors offer increased spatial resolutions of 50 cm or less (Table 2.1). The Gypsum Plain consists primarily of evaporite and carbonate facies with little vegetation as it is located in the semi-arid, southwestern United States. Top-of-atmosphere reflectance values of the main lithogroups (e.g. sulfates, carbonates and siliciclastics) present exhibit significant enough variation that increased spectral ranges and concentrated values of the hundreds of bands

Table 2.1: Primary satellite sensors offering commercially-available imagery data and corresponding relevant technical specifications (adapted from Harris et al., 2011).

Sensor Name	Type	Spectral Range	Spectral Resolution	Spatial Resolution
LANDSAT 7	Optical-Multispectral; Satellite-borne	0.4 to 2.35 μm and 10.4 to 12.5 μm	65 to 260 nm and 380 nm (pan)	30 m (60 m TIR; 15 m Pan)
ASTER	Optical-Multispectral; Satellite-borne	0.52 to 0.86 μm ; 1.60 to 2.43 μm ; 8.125 to 11.65 μm	60 to 100 nm; 40 to 70 nm; 350 nm	15, 30 and 90 m
QuickBird	Optical-Multispectral; Satellite-borne	0.45 to 0.90 μm		0.60 m Pan; 2 and 44 m Mss
WorldView-2	Optical-Multispectral; Satellite-borne	Pan. 0.45-0.8; VNIR 0.4 to 1.0 μm		0.5 m
HYPERION	Optical-Hyperspectral; Satellite-borne	0.35 to 2.5 μm	~ 15 nm	30 m
CASI	Optical-Hyperspectral; Airborne	0.4 to 1.1 μm	~ 20 nm	up to 1.23 m (crosstrack)
HyMap	Optical-Hyperspectral; Airborne	0.4 to 2.5 μm	~ 20 nm	3 to 10 m
PROBE-1	Optical-Hyperspectral; Airborne	0.4 to 2.5 μm	~ 20 nm	3 to 10 m

comprising hyperspectral data are not required for the basic discrimination of major features across the study area.

This study is a novel approach to the production of classified satellite imagery displaying surface geologic features using WorldView-2 color-infrared imagery products of the visible and near-infrared spectrum due to the commercial

availability of 50 cm spatial resolution. Computer assisted processing of color-infrared (CIR) satellite imagery was performed in order to produce a surface geology map through a supervised maximum likelihood classification of surface reflectance values for the entire study area in order to delineate lateral variations

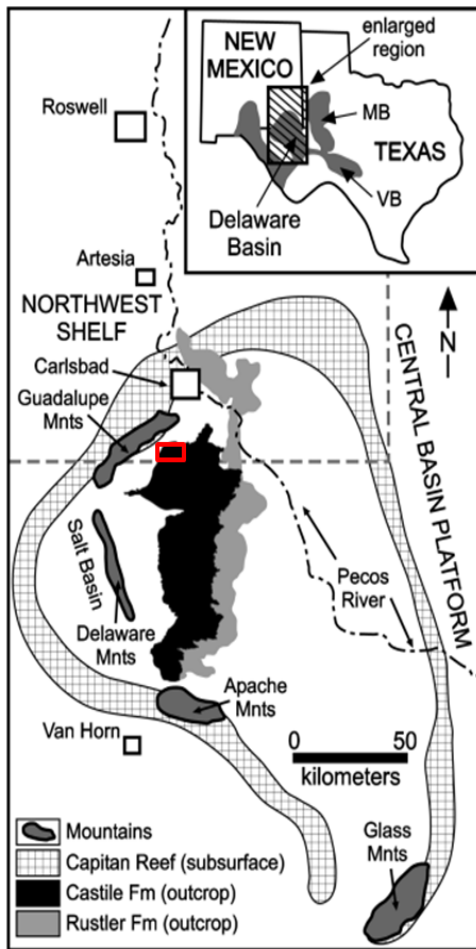


Figure 2.2: Location of the study area in relation to the surrounding Gypsum Plain comprised of the Rustler and Castile formations, and the greater Delaware Basin, delineated by the subsurface extent of the Capitan Reef and associated outcrops in various mountain ranges. Study area outlined in red (modified from Stafford, 2008a).

in lithology less than one m wide and aid in the identification of corresponding karst features across the Gypsum Plain. This study is the first of its kind to use WorldView-2 high-resolution multispectral satellite imagery to map the lithologic variability of the Gypsum Plain and based on published literature review, the first to be attempted in any evaporite karst terrain.

The study area is located in southeastern Eddy County, New Mexico and encompasses approximately 100 km² of land managed by the U.S. Department of the Interior, Bureau of Land Management (BLM). The area is commonly referred to as the Yeso Hills area of the Gypsum Plain in the

northwestern portion of the Delaware Basin (Figure 2.2) and is situated along the northern edge of the Chihuahuan Desert, along the southwestern margin of the Great Plains physiographic region. The Gypsum Plain is dominated by evaporites of the Ochoan Castile Formation, as well as residual remnants of the Salado and Rustler formations and minor secondary limestones (Hill, 1996). Annual precipitation in the region ranges from 150 to 400 mm, with an average temperature of 24°C, resulting in sparse, drought-tolerant vegetation (Stafford, 2015). Evaporite karst features, including surficial karren, sinkholes, and caves are abundant within the Castile Formation due to the high solubility of gypsum which results in a complex karst system that presents unique land management concerns.

GEOLOGIC SETTING

The assimilation of Pangea during the late-Paleozoic led to the division of the Permian Basin and formation of the intracratonic Delaware Basin (see Figure 2.2 inset) with limited connection to the open marine sea (Dickenson, 1981; Hill, 1996). The Gypsum Plain is developed within the northwestern portion of the Delaware Basin and consists primarily of varved, laminated to massive anhydrite/gypsum, interbedded with halite, of the late Permian (early Ochoan) Castile Formation (Dietrich et al., 1995; Hill, 1996; Stafford 2008b). The Castile represents a classic deep-water deposit within a large, stratified, brine-water basin (Adams, 1944) formed following marine disconnectivity at the end of Guadalupian time (Adams, 1972). The Castile overlies the sandstone/siltstone of the Bell Canyon Formation, and was deposited beneath the Salado and Rustler evaporite formations of the basin (Figure 2.3). Residual remnants of the continental Dewey Lake Red Beds, subsequently deposited above the Rustler Formation at the end of the Permian, mark the end of Permian marine deposition within the Delaware Basin and the transition to a combination of sabkha to delta-eolian like environmental fluctuations until subaerial exposure dominated throughout the Mesozoic.

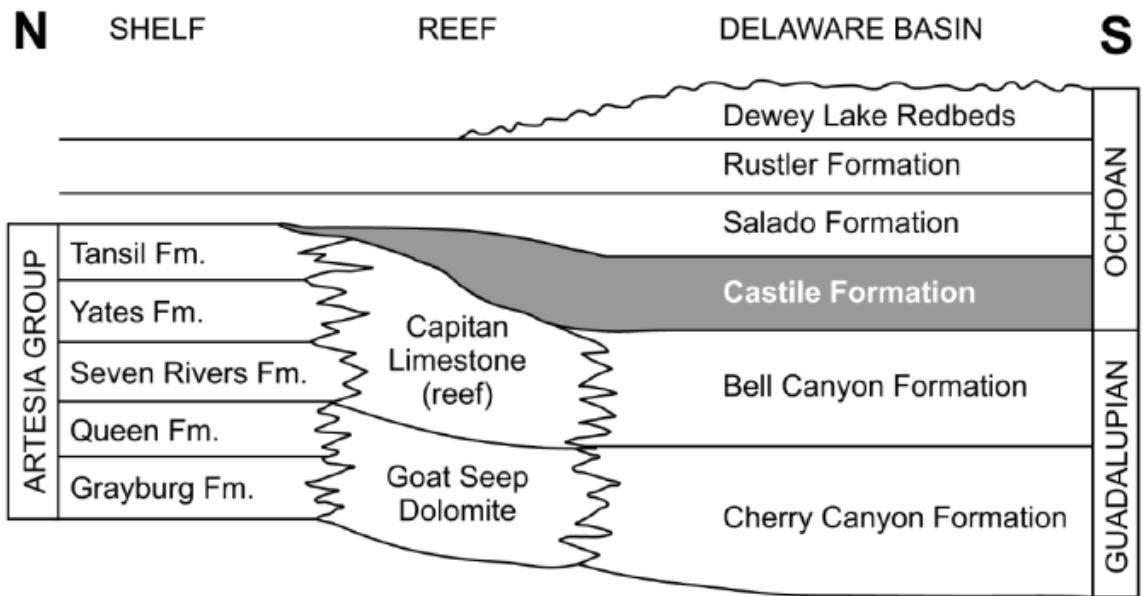


Figure 2.3: Major lithologic units of the Delaware Basin deposited during the middle- to late-Permian with the dominant karst-bearing unit, the Castile Formation, highlighted in grey (adapted from Scholle et al., 2004).

Cretaceous deposition of siliciclastics within the basin included the interbedded sandstone/conglomerate of the Cox Sandstone, anomalously located within the study area (Hill, 1996). Until the late Cenozoic, the basin experienced little tectonic activity and limited, sporadic deposition of sediments, followed by a period of aerial exposure, uplift and erosion of the late-Miocene associated with the formation of the western Rio Grande Rift (Kirkland, 2014). Therefore, surface exposures within the Gypsum Plain consist of the following lithologies: gypsum, calcite (limestone), dolomite (dolostone), siliciclastics (sandstone and conglomerates), gypsic soils and weathering byproducts of all lithologies.

Gypsum, the most common bedrock in the study area, promotes extensive karst development due to its high solubility (2.53 g/L) combined with near-linear solution kinetics. While most bedrock in the study area is covered by a thin, secondary gypsic crust (Figure 2.4A), a variety of surficial karren occurs in areas of exposed bedrock, including: rillenkarren (Figure 2.4B), spitzkarren (Figure 2.4D), kamenitzas, and tumuli. Karren may crop out across a few mm² to m² in area but is generally limited in size. Sinkholes are prolific, appearing as the dominant geomorphic karst manifestation and ranging in average size from dm to tens of m in diameter. Filled sinkholes, formed either by collapse of subsurface features or transport of sediment manifest as closed depressions (Figure 2.4C). Open sinkholes (Figure 2.4E) are generally connected to solutional conduits or cave entrances and may range from shallow, elliptical depressions to laterally elongated, incised arroyos. Sinkholes are commonly associated with partial to complete infilling by alluvium deposits and associated dense vegetation due to the higher moisture content available in these unconsolidated fill materials (Figure 2.4F). Caves and solutional conduits are widespread and often fracture controlled, ranging from small isolated features to complex forms that may significantly extend, both laterally and vertically, beneath the land surface (Stafford, 2008a). For a general review of hydrologically active karst manifestations within the Gypsum Plain, see Stafford et al. (2008a).



Figure 2.4: Common surficial karst manifestations within lithologies of interest across the study area: A) gypsic crust precipitate commonly deposited across a large portion of the study area; B) example of rillenkarren formed within exposed bedrock of the Castile gypsum; C) small-scale closed sinkhole formed due to subsurface collapse within alluvium; D) example of spitzkarren formed on an exposed surface of a gypsum breccia boulder of the Castile Formation; E) open sinkhole containing the entrance to Green Moss Cave formed within bedrock of the Castile gypsum; and F) closed sinkhole formed within alluvium acting as host to a dense cluster of grasses native to the Gypsum Plain.

Karst mounds, paleokarst erosional remnants formed by the collapse and infill of strata overlying subsurface karst voids (Bachman, 1980), sporadically occur across the Gypsum Plain, including several mounds that have been identified in the eastern portion of this study area. Karst mounds represent areas of cavernous porosity within the Castile gypsum and overlying Salado salts that underwent collapse in the past and experienced infilling by overlying strata that subsequently created topographic highs by differential weathering of surrounding gypsum during more recent surface denudation (Bachman, 1980; Hill, 1996). Karst mounds are generally less than 100 m in diameter with a low relief of 3 to 9 m (Hill, 1996). Steep sided hills composed of Rustler strata (Figure 2.5A) are found clustered along the periphery of the eastern half of the study area, at an average height and diameter of five m. K Hill (Figure 5B) provides a more complex example of this paleokarst phenomena and consists of karstic slump debris from the Rustler Formation, in addition to rotated and down dropped blocks of the Dewey Lake and Cox formations, creating an erosional positive relief structure approximately 18 m high in the central portion of the study area (Crawford, 1993). The Cox, Dewey Lake Red Beds, and Rustler formations within the study area solely manifest as karst mounds and have not been identified in situ at any localities.

Areas of the Gypsum Plain have undergone significant mineralogic diagenesis resulting in calcitized evaporites, which generally manifest as isolated

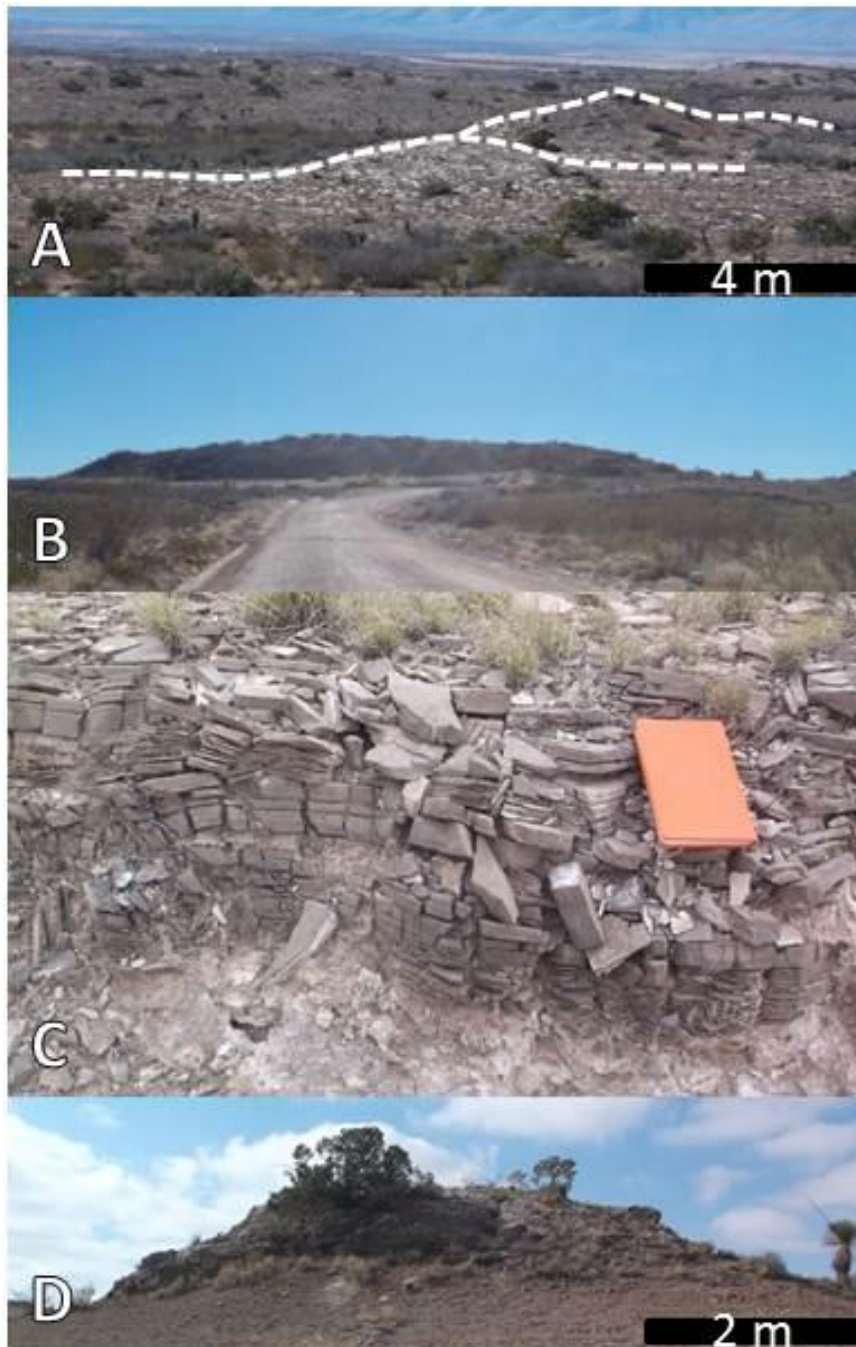


Figure 2.5: Karst mounds and areas exhibiting secondary calcitization: A) karst mounds (delineated with dashed white lines) primarily consisting of Rustler strata; B) K Hill, the largest karst mound in the study area consisting of Rustler, Dewey Lake Red Beds and Cox strata; C) laterally extensive calcitized blanket breccia; and D) small Castile butte located within the study area consisting of brecciated Castile gypsum that has been calcitized.

masses at the land surface or laterally extensive surface horizons (Figure 2.5C). Ascending light hydrocarbons, likely methane, reduced calcium sulfate to limestone throughout the Ochoan evaporites via either Bacterial Sulfate Reduction or Thermal Sulfate Reduction (Stafford, 2008c; Kirkland and Evans, 1976). Isolated limestone buttes, also known as “Castile Buttes” (Figure 2.5D), crop out across the Gypsum Plain as a product of differential weathering of these calcitized zones, creating topographic highs ranging from a few m² to tens of thousands of m² in area, and a maximum height of 40 m (Kirkland and Evans, 1976; Stafford, 2008c). Laterally extensive limestone sheets are present as residual brecciated clasts at the surface or as intact linear sheets dipping into the subsurface, generally where surrounding gypsum has been dissolved leaving less soluble calcitized residuum. Limestone sheets may range from a few dm to up to two m in thickness and can crop out over thousands of m² (Stafford, 2008a). Float of secondary limestone, small clasts of brecciated rock displaced by surface processes, may be localized to areas where the limestone is exposed at the surface or may cover wide areas of the landscape. Calcitization processes and mineral conversion of associated sulfur-ore deposits have also produced secondary selenite occurrences through near-surface oxidation which manifest as linear features, fracture fillings and lenticular masses (Stafford, 2008c).

MULTISPECTRAL IMAGERY DATASET AND CHARACTERIZATION

The use of remote sensing data to discriminate between and identify surficial lithologies for the purpose of geologic mapping is a well-established practice (Van der Meer et al., 2012). A variety of optical sensor data are available for this purpose, featuring varying spectral and spatial ranges and resolutions appropriate for different purposes and methodologies (Table 1). Today, hyperspectral data is most commonly employed in regional bedrock characterization due to greater spectral resolution and range allowing for increased ability and accuracy for identifying earth materials, such as mineral groups and lithotypes, across lithologically variable landscapes for the purpose of mineral mapping and exploration (Harris, et al., 2011; Kruse, 2015; Van der Meer, 2012). However, limited spatial resolution of commercially/publicly available data from hyperspectral sensors prevents small-scale outcrops and features from being discernible across an image, making it unsuited for the identification of small lithologic changes associated with karst features such as those present within the study area investigated and greater Gypsum Plain. Hyperspectral imagery data is also difficult to obtain and process, costly, and exhibits great redundancy in data (Kruse, 2015). Currently, the highest resolution, commercially-available hyperspectral data is 30 m Hyperion satellite-

borne data or that obtained via unmanned aerial vehicles (UAVs) equipped with a camera capable of collecting hyperspectral data. The use of UAVs in conjunction with hyperspectral cameras pose their own set of problems, including the high cost of both the platform and camera, time and possible travel required for collection of data and the ability of the user to operate the UAV effectively, to name a few. Conversely, multispectral data is less expensive/often free, less redundant and widely publically-available in increased spatial resolutions of up to 50 cm or less.

Karstic features targeted by this study generally occur on the cm to m scale and associated surficial lithologic variability is common over short lateral distances; therefore, more refined spatial resolution was required for lithologic mapping for improved natural resource management. As seen in Table 2.1, of commercial imagery available for purchase, WorldView-2 satellite imagery features the highest multispectral resolution available at 0.5 m (Harris et al., 2011). Traditionally, CIR imagery is used to differentiate vegetation health across a target area through the use of band rationing techniques (Wolf, 2010; Hamideh et al., 2014). However, the geologic remote sensing community has traditionally utilized visible to near-infrared imagery for lithologic and structural mapping. Additionally, working with a limited number of bands such as only those present within CIR datasets reduces extraneous data redundancy brought on by the overlap of adjacent channels in each sensor (van der Meer et al., 2012).

WorldView-2 CIR satellite imagery, acquired on September 27, 2016, was purchased by Stephen F. Austin State University, Department of Geology for use in this study, chosen for its 50 cm spatial resolution of generated products. Orthorectification and radiometric corrections were performed prior to purchase and imagery acquisition, including a dark offset subtraction and non-uniformity correction (Updike and Comp, 2010). Atmospheric corrections were performed, including conversion of raw digital numbers to top-of-atmosphere spectral radiance, and subsequently top-of-atmosphere reflectance using ArcGIS 10.2 following the process outlined by Updike and Comp (2010).

IMAGE CLASSIFICATION

Before performing image classification, a control point database was established for all documented surficial lithology types and karst features present within the study area. 10, one km² grids divided into traverse lines spaced at 50 m intervals were randomly selected across the study area and systematically mapped in order to develop detailed representative maps of lithologic and geomorphic variability. Based upon data collected through field mapping of each gridded control site, combined with a priori knowledge of the area and known geology, 10 unique sample classes were established for image analyses comprising the majority of the surface lithologies and features within the study area: 1) alluvium, 2) algal crust, 3) surficial gypsite precipitates, 4) dense vegetation manifesting usually as bushes one-quarter to several m² in area, 5) calcitized breccia zones or float, 6) exposed Castile gypsum bedrock, 7) residual Cox strata, 8) residual Dewey Lake Red Beds strata, 9) residual Rustler strata, and 10) surface bodies of water. Subsequent to field mapping, additional areas suspected of representing each of the 10 established classes were systematically identified across the entirety of the study area in order to evaluate feature class variability using Google Earth Pro. Locations of identified features were recorded and physically verified in the field to supplement field data

attained from detailed physical mapping of gridded sites. Once verified for accuracy, GPS coordinates were established for 106 control points representing each lithology or lithologic feature of interest across the entire study area, not including bushes/large vegetation features (Figure 2.6). These control points were utilized to create training samples and establish reflectance values of the corresponding CIR raster cells. Vegetation related control points were established directly within the original CIR imagery products in order to account for the temporal change associated with vegetation life cycle and actual physical existence of features both on the ground and within the image.

Computer assisted processing was employed via ArcGIS for Desktop 10.2 software in order to produce a maximum likelihood classification (MLC) of the CIR imagery acquired for use within this study. Based on the control points previously established in the field, areas corresponding to each lithology type were specified and surface reflectance values extracted in the form of training samples. A signature file was created, in which each individual class was assigned the mean vector and covariance matrices of the collective cells comprising the specific training sample, and used to perform a maximum likelihood classification of each raster cell within the study area. The final product consisted of an output classified raster in which each cell was assigned a class based on the value of the cell.

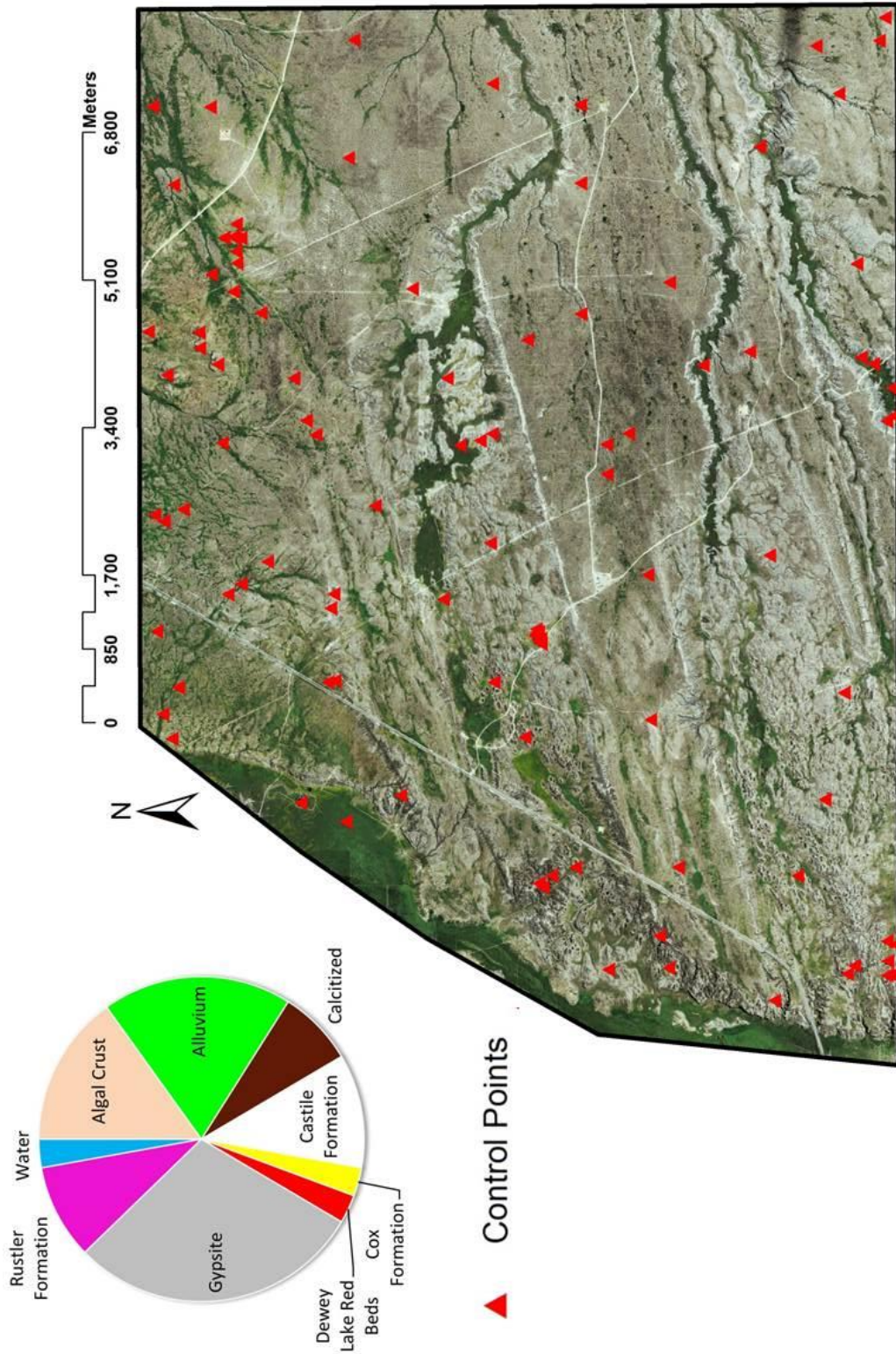


Figure 2.6: Location of each control point identified and field checked for nine of the 10 classes used for later classification of the color-infrared data set (control points were not established for "Vegetation"). Chart (top left) details the number of control points across the landscape corresponding to each class identified in the field.

Parameters specified for the creation of the MLC included a priori probability weighting and specification of a reject fraction. The number of cells comprising the training samples was used to produce the signature file for raster cell classification was specified to be proportional to the number of cells of that class in the output classification raster; this was based on the relative number of control points corresponding to each class recorded across the study area as proportional percent of the study area covered by that lithology. A “confidence value” was calculated during MLC ranging from 0.05% to 100%, indicating the confidence with which each raster cells is assigned a class value. Those cells with a confidence value of 5% or less were rejected and assigned no cell value during image classification. Vegetation masks the individual spectra of the rock or soil in which it is growing, therefore requiring values identified as ‘Vegetation’ to be reclassified relevant to this study. Further processing of the MLC raster was performed by assigning ‘Vegetation’ values to the class of their nearest neighbor based on Euclidean distance.

Three sites of specific interest were selected for more detailed assessment within the study area (Figure 2.7A) based on the presence of multiple significant karst related manifestations and a high density of control points present in order to assess method accuracy. Site one (Figure 2.7B) features large areas of exposed calcitized blanket breccias, a Castile butte, small mounds covered by algal crust and grass-filled depressions separated by a

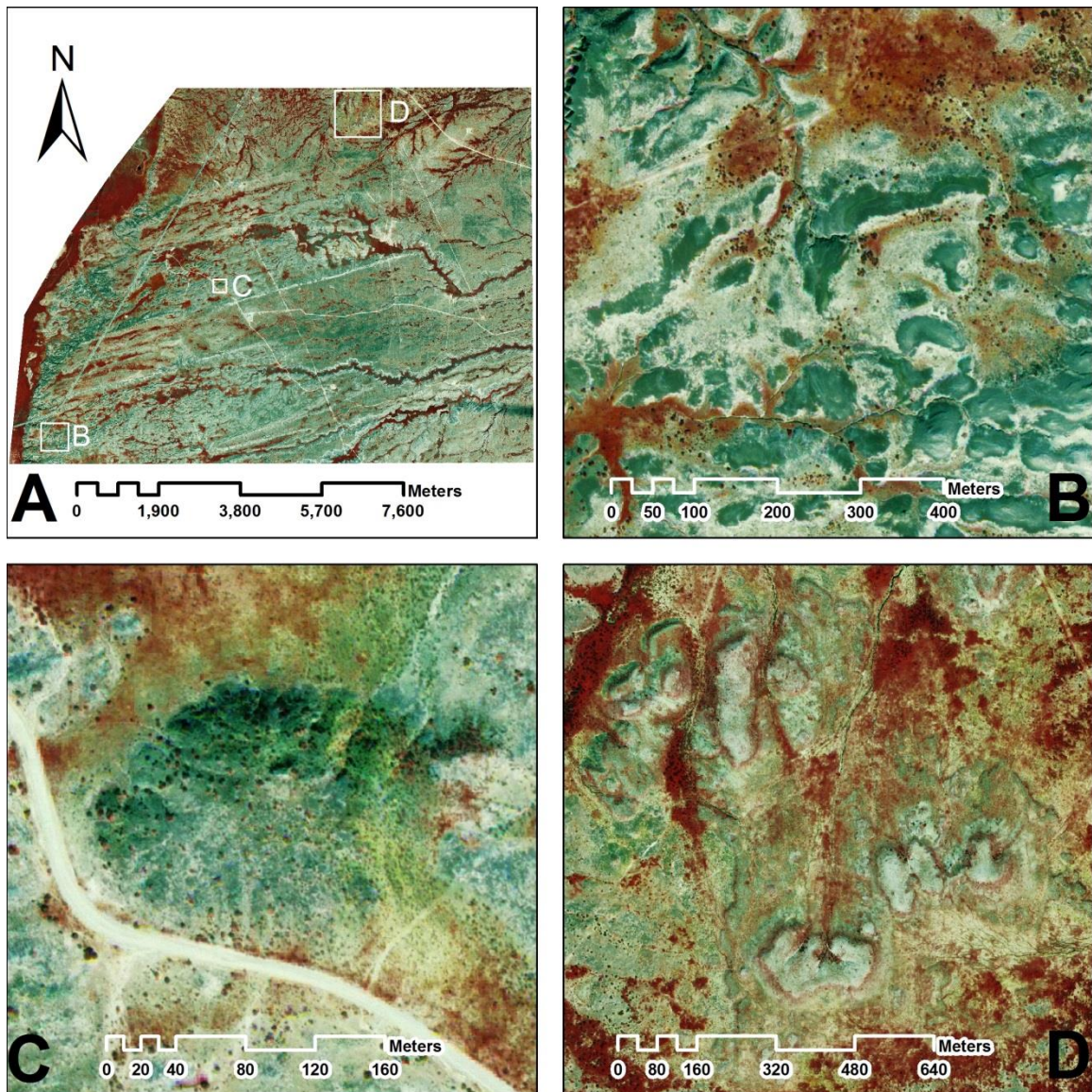


Figure 2.7: Color-infrared imagery of selected sites of interest evaluated, including: A) relative location of three sites within larger study area (see figure 1 for reference location of Figure 8A); B) clustered area of exposed calcitized breccia and one of the two Castile buttes located in the study area; C) K Hill karst mound remnant of paleocavern breccia infilling; and D) clustered area of karst mounds composed of Rustler collapse strata.

significant amount of gypsite in which several karstic sinkholes have been identified. The second site (Figure 2.7C) is focused on the carbonates of K Hill, surrounded by gypsite and exposed gypsum containing multiple small epigene

karst features. Site three (Figure 2.7D) was chosen for the presence of several karst mounds of the Rustler Formation separated by gypsite.

Figure 2.8 displays the final classified images produced for the three sites of specific interest, while Figure 2.9 is that of the entire study area. Correlation of the control points used to create training samples indicates that 61% of points were classified with absolute accuracy. Discrepancies in lithologies most often occurred between cells classified as the Rustler Formation and Gypsite, which is consistent with field observations where Rustler Hills are almost always capped by well-developed gypsite. Figure 2.10 indicates that this is due in part to the similarity in reflectance values indicated by the two lithologies. Areas of gypsite not associated with Rustler across the study area, but classified as so are due to the similar reflectance values. Additionally, the Cox Formation and Dewey Lake Red Beds are difficult to distinguish from one another due to the same similarity in mean reflectance values exhibited between classes. Both the Cox and Dewey Lake are carbonates with similar chemical compositions, thus similar reflectance values. Visual comparison with Google Earth Pro imagery was used to evaluate the overall accuracy of the area which showed strong a priori agreement with knowledge of the study area. All control point values misclassified were clusters of only a few cells, less than a few m², located within a greater area of the control point lithology.

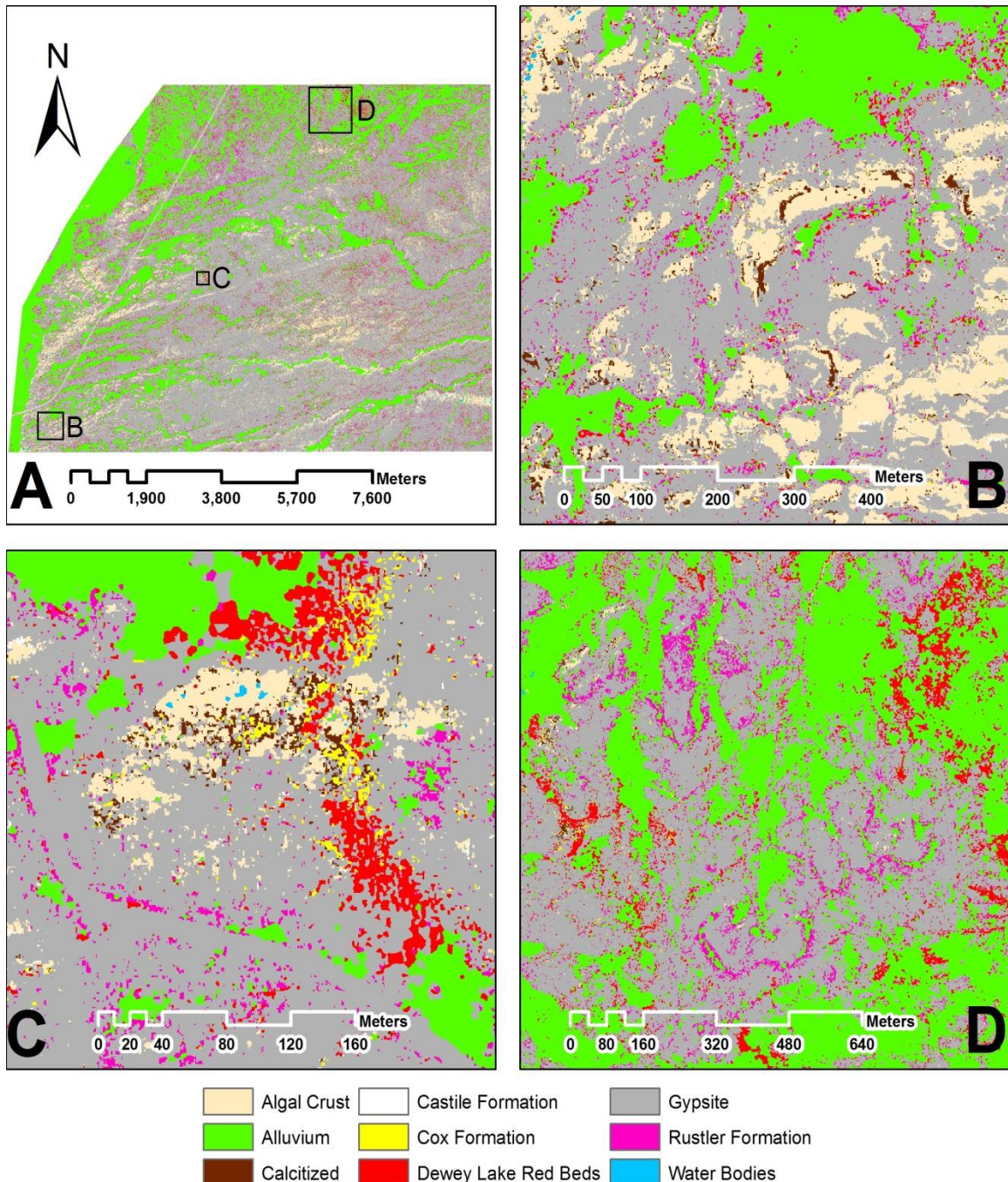


Figure 2.8: Final Maximum Likelihood Classification rasters produced for each of the three areas of interest from figure 2-7: A) relative location of three sites within larger study area (see figure 1 for reference location of Figure 8A); B) clustered area of exposed calcitized breccia and one of the two Castile buttes located in the study area; C) K Hill karst mound remnant of paleocavern breccia infilling; and D) clustered area of karst mounds composed of Rustler collapse strata.

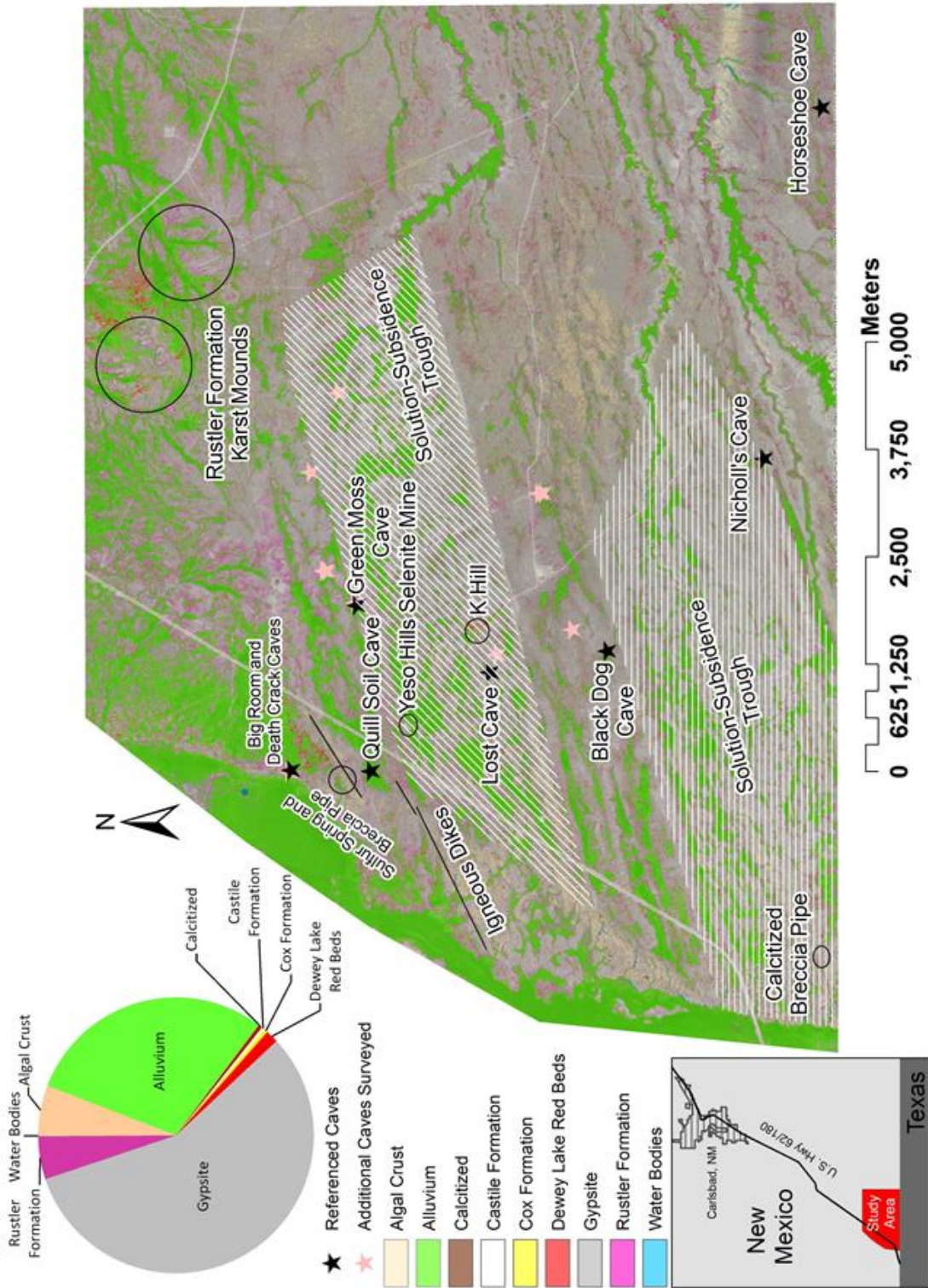


Figure 2.9: Final lithologic surface map of the study area based on the maximum likelihood classification performed.

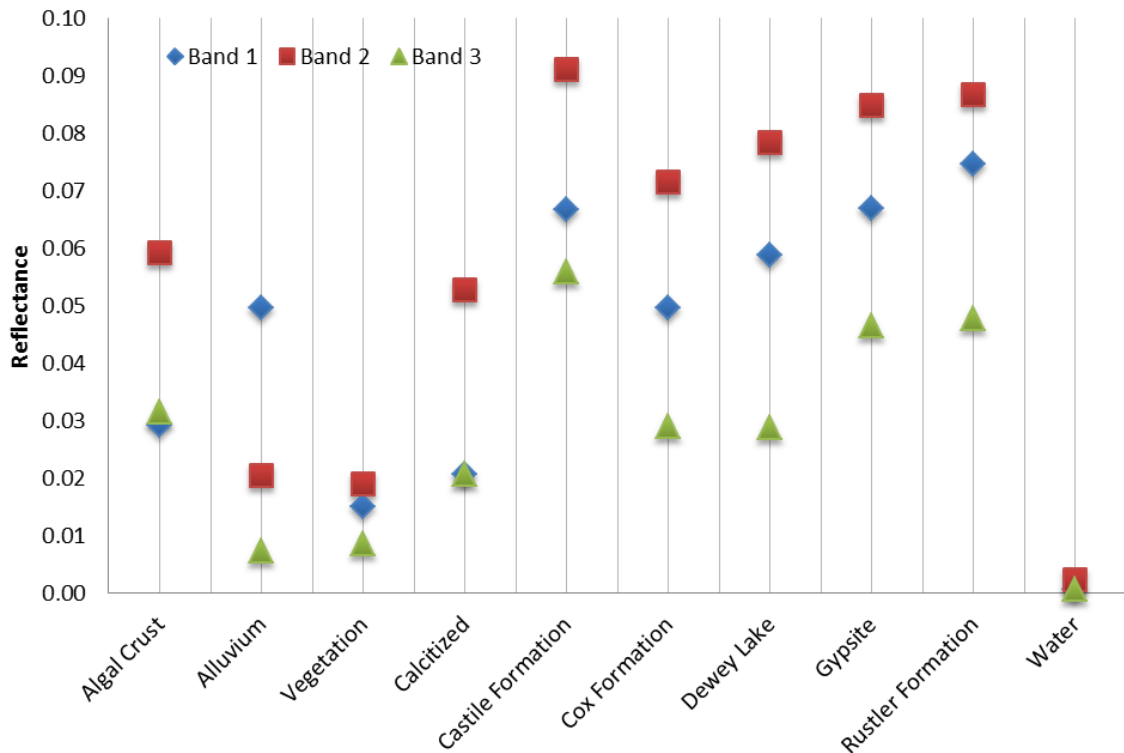


Figure 2.10: Graph displaying the mean reflectance value of each band for the corresponding class' training samples. Note distinct reflectance values for most sample classes.

Post-depositional alteration of gypsum due to high solubility and ease of weathering has resulted in the existence of a thin gypsic residue across the landscape of the Gypsum Plain (Watson, 1982). Spectral sensors employed in the collection of CIR data only collect data concerning surface reflectance characteristics, indicating that many of the signatures collected have been influenced by the weathered, surficial residue (Harris et al., 2011) inhibiting the comparison of values across the image observed with standard laboratory-based values for carbonates and evaporites for accuracy.

CONCLUSIONS

Surface geologic maps created through the classification of spectral reflectance values across a landscape via satellite imagery is a more efficient approach to characterization of the lithologic variability within the karsted landscape of the Gypsum Plain of the Delaware Basin than traditional methods commonly employed. Results of this study enabled efficient and largely effective geologic mapping of the entire 100 km² study area (Figure 2.10), which could be extended throughout the entire Gypsum Plain and is currently being utilized for improved delineation of likely regions of more intense karst development, including caves and paleokarst features. High spatial resolution is especially important in the creation of such products, resulting in the use of multispectral data rather than hyperspectral data in this study based on current technology of commercially-available data. Based on the training sample values and classification parameters used, the methods employed in this study produced a more accurate representation of the study area based on comparison with control points, Google Earth Pro imagery and familiarity with the area, than traditional, published geologic maps of the region indicate (Figure 2.1).

Differences in control point values and classified cell values were the product of extremely similar reflectance values across multiple bands of the CIR

imagery due to similar chemical composition of actual or constantly associated lithologies and were almost always individual to small clusters of cells located in a greater area of the correct lithology; the confusion between Rustler and gypsite lithologies, where gypsite thinly mantles Rustler strata, being the exception. The use of such remotely-sensed map products as those developed in this study allows for targeted survey and identification of karst features, rather than methodical surveys that often take months to years of field observations to complete, thus increasing field efficiencies and reducing potential assessment costs.

The creation of surface geologic maps via less expensive, less time consuming processes such as satellite image classification for the characterization and use in identification of geologic variability across a karsted landscape is useful to entities such as the Bureau of Land Management or other agencies for a more efficient approach to natural resource management. Greater availability and decreased cost of multispectral data than that of hyperspectral, as well as simplified pre- and post-classification image processing allows for the use of proposed methods by a greater community and lower skill and experience levels with remote sensing. As technologies increase, hyperspectral imagery analyses will likely be used for even greater accuracy (especially of cells pertaining to Rustler/gypsite and Cox/Dewey Lake issues) of remotely sensed geologic mapping within the Gypsum Plain and similar arid environments, but

currently, commercially-available, satellite-based hyperspectral imagery resolution is too poor. New and rapidly advancing UAV technologies will provide significant opportunities for improved geologic characterization within complex karst systems such as the Gypsum Plain in the near future, but likely require a significantly higher cost to be obtained, as well as all issues previously specified.

REFERENCES

- Adams, J.E. (1944). Upper Permian Ochoa series of Delaware Basin, West Texas and southeastern New Mexico. *Am. Assoc. Petroleum Geol. Bull.*, 28, 1596-1625.
- Adams, J.E. (1972). Semi-cyclicality in the Castile anhydrite; in Elam, J.G. and Chuber, S. (eds.), *Cyclic sedimentation in the Permian Basin*. Texas: West Texas Geol. Soc.
- Bachman, G. O. (1980). Regional geology and Cenozoic history of Pecos Region, Southeastern New Mexico. *U.S. Geol. Surv.*, Open-file Rept. 116, 80-1099.
- Crawford, J. E. (1993). K Hill and the Yeso Hills selenite occurrence. in Love, D.W., Hawley, J.W., Kues, B.S., Adams, J.W., Austin, G.S. & Barker, J.M. (Eds.), *Carlsbad Region, New Mexico and West Texas*. New Mexico: New Mexico Geological Society.
- Dickenson, W. R. (1981). Plate tectonic evolution of the southern Cordillera. *Arizona Geological Society Digest*, 14, 113-135.
- Dietrich, J. W., Owen, D. E., Shelby, C. A., & Barnes, V.E. (1995). *Geologic atlas of Texas: Van Horn- El Paso sheet*. Austin: University of Texas Bur. Econ. Geol.
- Green, G.N. and Jones, G.E. (1997). The Digital Geologic Map of New Mexico in ARC/INFO Format: U.S. Geological Survey Open-File Report 97-0052.
- Harris, J., Wickert, L., Lynds, T., Behnia, P., Rainbird, R., Grunsky, E., McGregor, R., & Schetselaar, E. (2011). Remote Predictive Mapping 3.

Optical Remote Sensing - A Review for Remote Predictive Geological Mapping in Northern Canada. *Geoscience Canada*, 38(2), 49-84

- Hamideh, N., Beecham, S., Anderson, S., and Nagler, P. (2014). High spatial resolution WorldView-2 imagery for mapping NDVI and its relationship to Temporal Urban Landscape Evapotranspiration Factors. *Journal of Remote Sensing*, 6, 580-602.
- Hill, C. A. (1996). *Geology of the Delaware Basin, Guadalupe, Apache and Glass Mountains: New Mexico and West Texas*. R. F. Lindsay & R. A. Garber (Eds.). Midland, Texas: Permian Basin Section- SEPM.
- Kirkland, D.W. (2014). Role of hydrogen sulfide in the formation of cave and karst phenomena in the Guadalupe Mountains and western Delaware Basin, New Mexico and Texas. *National Cave and Karst Research Institute, special paper 2*.
- Kirkland, D.W. and Evans, R. (1976). Origin of limestone buttes, Gypsum Plain, Culberson County, Texas. *Am. Assoc. Petroleum Geol. Bull.*, 60(11), 2005-2018.
- Kruse, F. A. (2015). Integrated visible and near-infrared, shortwave infrared, and longwave infrared full-range hyperspectral data analysis for geologic mapping. *Journal of Applied Remote Sensing*, 9(1), 096005-1-096005-17.
- Stafford, K.W.(2015). Evaluation of Existing Geologic Conditions along RM 652: Initial Characterization of Karst Geohazards Associated with RM 652 in Culberson County, Texas: TxDOT rep.,1–71.
- Stafford, K., Nance, R., Rosales-Lagarde, L., and Boston, P. (2008a). Epigene and hypogene gypsum karst manifestations of the Castile Formation: Eddy County, New Mexico and Culberson County, Texas, USA. *International Journal of Speleology*, 37(2), 83–98.

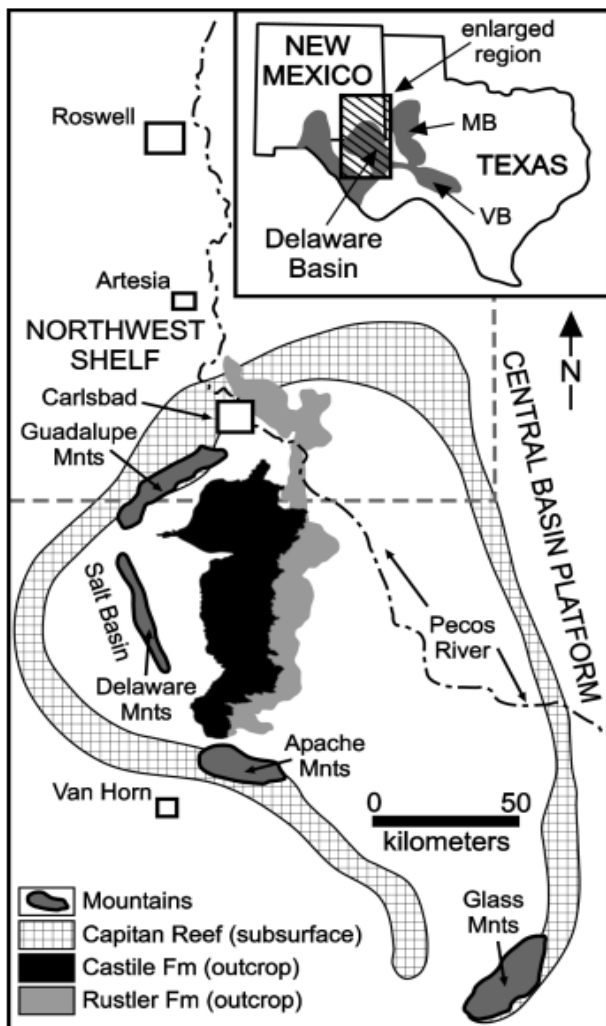
- Stafford K.W., Rosales-Lagarde L. and Boston P.J. (2008b). Castile evaporite karst potential map of the Gypsum Plain, Eddy County, New Mexico and Culberson County, Texas: a GIS methodological comparison. *J. Cave and Karst Studies*, 70(1), 35-46.
- Stafford, K.W., Ulmer-Scholle, D., and Rosales-Lagarde, L. (2008c). Hypogene calcitization: Evaporite diagenesis in the western Delaware Basin. *Carbonates Evaporites*, 23(2), 89–103
- Urdike, T. and Comp, C. (2010). Radiometric use of WorldView-2 imagery. Digital Globe. Tech. Rept.
- Van der Meer, F.D., van der Werff, H.M., van Ruitenbeek, F.J., Hecker, C.A., Bakker, W.H., Noomen, M.F., van der Meijde, M., Carranza, E.J.M., de Smeth, J.B., Woldai, T. (2012). Multi- and hyperspectral geologic remote sensing: A review. *Int. J. Appl. Earth Obs. Geoinf*, 14, 112-128.
- Watson, A. (1982). The origin, nature and distribution of gypsum crusts in deserts. University of Oxford.
- Wolf, A. (2010). Using WorldView 2 VIS-NIR MSI Imagery to Support Land Mapping and Feature Extraction Using Normalized Difference Index Ratios. *Proc.SPIE*, 8390.

APPENDIX A

DETAILED LITERATURE REVIEW

INTRODUCTION

The Delaware Basin of southeast New Mexico and West Texas is the site of extensive karst development within evaporite strata. The presence of karst creates complex natural resource management problems for the region. Oilfield



drilling and exploration operations have increased recently due to advances in hydrocarbon extraction abilities, placing additional environmental pressures on the natural resources of the area, including water resources and associated karst.

The Delaware Basin is located within the western portion of the Permian Basin of southeastern New Mexico and West Texas (Figure A1). The basin occupies an area of approximately

Figure A1: Extent and location of the Delaware Basin in the Trans-Pecos Region (MB-Midland Basin; VB-Val Verde Basin) (from Stafford, 2015).

33,500 km² and is an irregular,

north-northwest trending, inverted pear-shaped depression 250 km long and 180 km wide. Approximately 7,315 m of Phanerozoic sediments reside within this depression (Hill, 1996); the inner basin area is surrounded by the Capitan Reef complex. The Delaware Basin is primarily situated within the Chihuahuan Desert in the Pecos River section of the Great Plains, receiving on average 150 to 400 mm of precipitation per year and maintaining an average temperature of 24 C° (Stafford, 2015).

During Guadalupian time, a thick sequence of siliciclastic sediments was deposited within the Delaware Basin as the Cherry Canyon and Bell Canyon formations, as well as limestone as reef material with interbedded carbonates and siliciclastics of the shallow lagoonal shelf formed inland. The basin was the last site of deep water sedimentation and massive reef growth in the area (Hill, 1996). Following this, the Ochoan Series of the Late Permian saw deposition of thick sequences of evaporites caused by the closing of the Hovey Channel and the Delaware Basin to marine waters marking the beginning of the continental regime within the Delaware Basin. The Castile, Salado, Rustler, and Dewey Lake continental red beds were all deposited sequentially throughout Ochoan time (Hill, 1996)

GEOLOGIC HISTORY

The structural history of the Delaware Basin may be divided into a series of phases beginning with the passive margin phase (Horak, 1985). Initially, a peninsular spur originated off of the Transcontinental Arch which covered areas of southeastern New Mexico and western Texas. Sagging of this peninsular spur, due to cooling and shrinking of underlying crust and mantle rocks, created the negative axis of the Tobosa Basin (Adams, 1965). The Tobosa Basin developed as a broad, shallow, gently dipping depression characterized by weak crustal extension and low rate subsidence (Galley, 1958; Horak, 1985). The Early Ordovician Ellenberger Sea slowly transgressed over this flattened coastal plain from the Marathon Embayment to the south (Adams, 1965). Aside from minor periods of exposure, deposition began and continued for almost 300 million years. Crustal warping led to a series of sags and arches throughout the basin that were further intensified by block-faulting (Hill, 1996). The largest of the sags consists of a 563 km wide depression between the Texas Arch to the east and the Diablo Arch to the west (Adams, 1965).

The collision phase began with the formation of the supercontinent of Pangea through the collision of Laurasia and Gondwana (Hill, 1996). This collision caused the originally negative axis of the Tobosa Basin to be lifted to

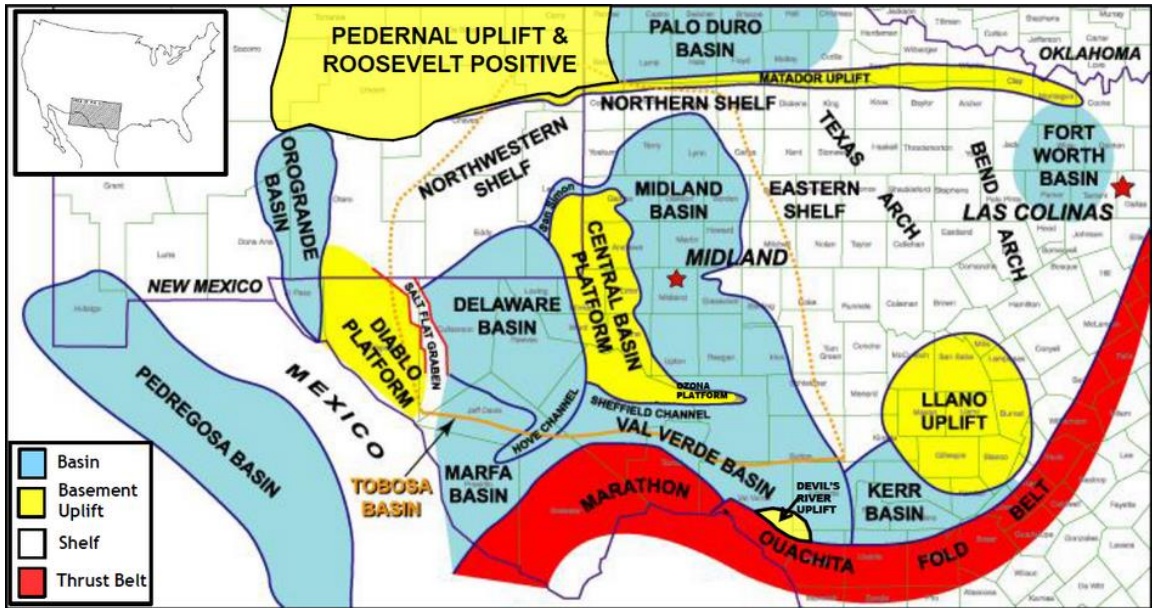


Figure A2: Location and relationship of major sedimentary basins associated with study (from Pioneer Natural Resources, 2016).

form the Central Basin Platform, leading to the structural separation seen today of the Delaware and Midland basins (Figure A2). Additionally, the Ouachita-Marathon fold belt was formed along high-angle basement faults and pre-existing zones of weakness (Horak, 1985). The early Pennsylvanian was a time of rapid subsidence within the western Delaware Basin, which remained a deep water site until at least the end of Guadalupian time (Adams, 1965; Hill, 1996). The eastern portion of the Delaware Basin experienced a deepening due to vertical movement followed by a tilting to the east (Hills, 1984).

These events carried into the Permian Basin phase, when tectonic stability was achieved. At this time, the region was part of the southern flank of the North American craton, on the western margin of Pangea (Hill, 1996). The Early

Permian Wolfcampian experienced rapid filling of the previously formed sags with clastics from nearby mountain ranges and the formation of reef fringed carbonate/evaporite platforms (Horak, 1965). The Leonardian saw a decrease in the extreme rate of subsidence previously experienced (Adams, 1965). With the Guadalupian came a shift in sediment deposition to siliciclastic accumulations, while the platforms and shelves experienced carbonate deposition (Adams, 1965). Uplift of the basin eventually caused the Hovey Channel, the source of marine waters within the Delaware Basin, to close (Hill, 1996).

The Mesozoic marked the beginning of the stable platform phase. During this period all elements of the Permian Basin remained intact and acted as a single unit (Horak, 1965). The restricted seas of the Ochoan expanded eastward and northward with a new epoch of sagging (Adams, 1965). The surrounding Southern Cordillera experienced a much different history, with rifting acting to separate North and South America. The Marathon region also experienced similar rifting and spreading related to the Yucatan's separation from Texas (Hill, 1996). As the rifted margin of the Gulf of Mexico subsided, a transgression of marine waters was able to spread across Texas and portions of the western United States. This transgression led to additional sediment deposition within the Delaware Basin and surrounding areas (Keith, 1982).

The stable platform phase followed the Permian Basin phase. Little movement occurred during this phase, causing few new structures to be formed

within the basin. The Laramide Orogeny occurred approximately 150 million years later, causing little deformation to the basin. Volcanic deposits originated in six centers within West Texas and adjacent portions of Mexico, ushering in the volcanic phase of the Late Eocene to Late Oligocene. This volcanic phase produced intrusive and extrusive volcanism in the Glass Mountains and deposited dikes within basinal areas (Hill, 1996). This led to a large increase in heat flow in the Delaware Basin: the cause of this activity is a matter of speculation. Finally, the Basin and Range phase saw extensive tectonism in the southwestern United States, primarily leading to additional uplift in the Delaware Basin (Horak, 1985). Block faulting and jointing on the western side of the Delaware Basin caused the adjacent Salt Basin to dropdown. Tensional stress produced high-angle normal faulting and fracturing (Hill, 1996).

Guadalupian Series Stratigraphy

Guadalupian time marked the end of normal marine carbonate deposition in the Delaware Basin. Extensive reefs composed of organic-inorganic, long, linear, wave-resistant structures, characterized this eight to nine million-year-long period. The deep basin consisted of a dense sequence of siliciclastics while limestone was deposited as reef material around the periphery. The shallow shelf lagoon was made up of interbedded carbonates, evaporites and siliciclastics. The decrease in areal extent of the Delaware Basin occurring throughout this time

resulted in the isolation of the Midland Basin, leaving the Delaware Basin as the final site of deep water sedimentation and massive reef-structure growth in the late Permian (Hill, 1996).

Cherry Canyon Formation

At the southern end of the Guadalupe Mountains, making up the upper half of the slope below the Capitan Limestone cliffs, the Cherry Canyon (Figure A3) comprises the middle formation of the Delaware Basin (King, 1942). This formation averages 300 to 400 m in thickness, and consists of thin-bedded, finely-laminated, fine-grained sandstone and siltstone. A cyclic deposition of sedimentation is evident in the repetition of shaly sandstone, followed by thin-bedded sandstone, concluding with lenticular or nodular sandstone before the three types are repeated every 3 to 6 m. Tongues of limestone that may be

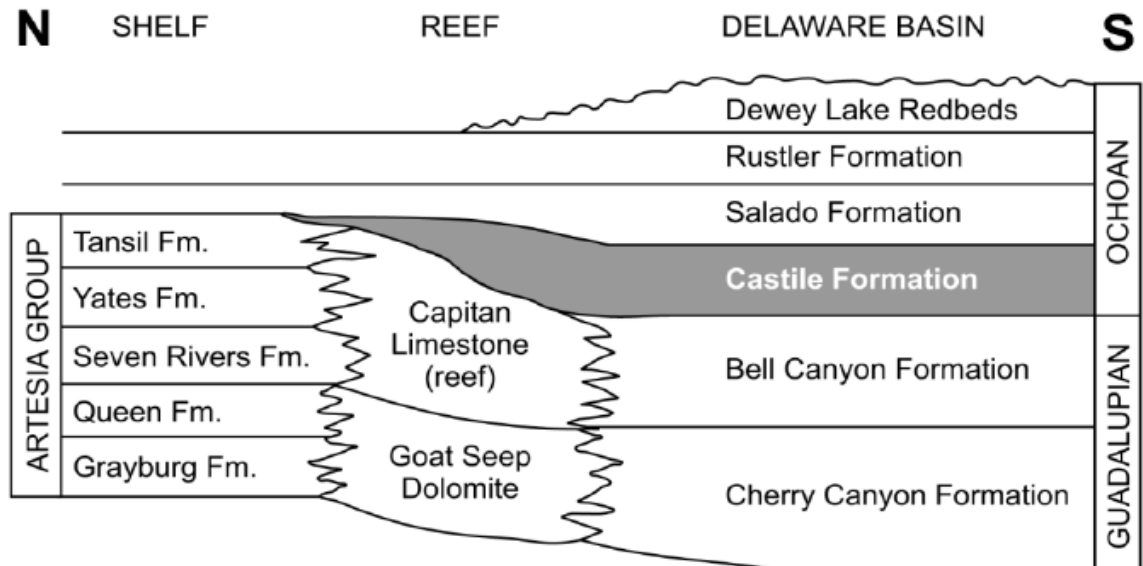


Figure A3: Lithologic units of the Delaware Basin and associated cross-section (adapted from Scholle et al., 2004).

traced or correlated with reef and shelf rocks of the Delaware Basin are also present within the Cherry Canyon Formation (Hill, 1996).

A few km shelfward, making up the lower quarter of the Cherry Canyon, is a sandstone tongue varying from 30 to 60 m in thickness. Above this lies the Getaway Limestone Member which varies from 60 to a few m in thickness. The Getaway Limestone is a black to dark-gray, thinly-bedded, dolomitic limestone. Often, silty locales may be found containing some lighter gray, granular, very fossiliferous units. Carbonate debris flow deposits are also common. Approximately 180 m above the base of the Cherry Canyon is the South Wells Limestone Member. Thin- to medium-bedded, black to gray, fossiliferous, dolomitic limestone is interbedded with buff to brown, fine-grained sandstone beds for a total thickness of 20 to 25 m. Laminated beds and current ripple marks are common here (Hill, 1996).

The uppermost member of the Cherry Canyon Formation is the Manzanita Limestone Member. This is a dense, buff-colored to earth gray dolomite ranging from 20 to 45 m in total thickness. Several layers of waxy, green, bentonite ash beds and pale apple-green, siliceous shale or chert beds may be found throughout the member (Beck, 1967). King (1948) speculated that these volcanic ash layers present over the entire outcrop area may have originated from a volcanic area to the south. The Manzanita Member also features a paleontologic gap that extends to the base of the Hegler Member of the Bell Canyon

Formation. Only poorly preserved fossils may be found here. This may be due to the nature of the late Cherry Canyon Formation as that of a period of transition for invertebrates within the Delaware Basin and an abrupt and substantial drop in sea level (Hill, 1996).

Bell Canyon Formation

Between the Delaware Mountains and the Gypsum Plain to the east, the Bell Canyon Formation crops out as a broad belt. The uppermost formation of the Delaware Mountain Group, the Bell Canyon, ranges anywhere from 200 to 300 m thick (King, 1942; Henrickson and Jones, 1952). The Bell Canyon Formation is lithologically similar to the Cherry Canyon Formation, consisting of fine-grained sandstone and coarse-grained siltstone with some interbedded, thin limestone. The sands present are extremely well-sorted, fine-grained quartz (Hill, 1996). In addition, the formation exhibits high feldspar content (Jenkins, 1961). Carbonate tongues existing near reef margins exhibit abundant fossil content while deeper basin waters were not able to support life; therefore, they contain low, restricted fossil quantities. As seen in the Cherry Canyon Formation, carbonate tongues of the Bell Canyon interfinger with sandstone units along the margin of the basin, continue to thicken in the reefward direction and finally merge with the Capitan Limestone. These carbonate tongues are correlative with upper Guadalupian shelf units (Hill, 1996).

The Bell Canyon Formation consists of five formally named carbonate members of the marginal facies, all exhibiting a strongly calcitic nature. The lowest member, the Hegler Limestone, consists of a dark gray slabby limestone up to 75 m thick in certain areas (King, 1942). The Hegler Limestone may range from the properties seen at the type locality of a dark gray, fine-grained limestone made up of closely-spaced nodules a few cm thick, to a dense, light gray, thinly-bedded, spotty limestone containing vugs filled with spar as seen on the western face of the Guadalupe Mountains (King, 1948). These limestones stand in two distinct groups of ledges with a total thickness of three to six m, separated by a break consisting of sand or marl. Directly above the Hegler Limestone Member lies the Pinery Limestone Member, in areas as much as 45 m thick. The Pinery Limestone is a dark gray, fine-grained, somewhat cherty limestone of thin straight beds containing several thicker, light-colored layers near the base (Hill, 1996). Thinning of the member occurs from about 35 m at the basin margin to about five m approximately 20 km basinward (Koss, 1977).

Following this is the Rader Limestone Member. The Rader Limestone is a massive, light gray limestone ranging from 10 to 40 m thick and darkening in the basinward direction (King, 1942). Outcrops tend to contain reef and upper slope-derived, poorly-sorted, pebble to boulder sized lithoclasts set in a sandstone matrix (Scholle and Halley, 1980). Sheet-like megabreccias of a mixed-debris flow/turbidite origin are also commonly found within the Rader (Lawson, 1989 a,

b); at least one apple-green, volcanic ash layer of bentonite also exists here. The McCombs Limestone Member, usually less than five m thick, follows the Rader as a very thin and flaggy limestone (King, 1942). A thick, 120 m sequence of sandstone occurs between the Rader and Lamar members. This sandstone interfingers with the McCombs; sands equivalent to the informal member of the Ramsey Sand of the deep basin and Yates reside on the shelf (Hill, 1996).

Finally, the last of the formally named carbonate members and uppermost limestone tongue of the Bell Canyon Formation is the Lamar Limestone Member. This is an extremely useful correlation unit. The Lamar is black in color with an approximately uniform thickness of eight m across the entire Delaware Basin. As a dense, flaggy, gray to black, fossiliferous limestone, the member contains a significant amount of organic matter. Some areas exhibit laminations or high chert content. As the five marginal carbonate members pinch out basinward, they are replaced by a series of sandstone units in the deeper water basin.

Depositional water depths have been speculated to range from 100 m (King, 1934) to 730 m (Adams, 1936), and close to 500 m near the end of the Bell Canyon time (Williamson, 1980). These deep water sands include the Hayes Sand, Olds Sand, Ford Shale, Ramsey Sand, and Lamar (or Trap) Shale (Hill, 1996).

Ochoan Series Stratigraphy

The Ochoan series marks the ending stage of the Permian Sea and the marine events occurring from Precambrian to Guadalupian time. The shift from limestones, siltstones, and sandstones to thick sequences of evaporites and thinner sequences of red beds signifies the closing of the Delaware Basin to marine waters. The following continental regime created 1200 to 1500 m of strata over the 500,000 to 600,000 year period (Hill, 1996). A soluble, friable nature exists here causing outcrops of Ochoan age rock to be more common in the subsurface (Jones, 1954). Formations present within the Ochoan series include the Castile, Salado, Rustler, and Dewey Lakes. The Castile consists mainly of anhydrite, the Salado of halite, the Rustler of dolomite and anhydrite, and the Dewey Lakes of continental red beds (Hill, 1996). Each of these formations indicates the existence of an interior continental desert with a very arid climate in West Texas and eastern New Mexico (Scholle et al., 1992).

Castile Formation

The oldest unit of the Ochoan Series consists of massive to laminated anhydrite and gypsum interbedded with halite that is completely devoid of fossils (Henrickson and Jones, 1952). The Castile crops out from the Delaware Mountains to the Rustler Hills, from west to east, on the Gypsum Plain. Thickness varies from areas completely lacking the formation to areas exhibiting

480 m of Castile thickness in the subsurface: at the surface it weathers to form a grayish-white gypsite. Dissolution of halite has caused breccia zones, initiated by the uplift and tilting of the west side of the basin (Hill, 1996).

Essentially, non-evaporite deposits are nonexistent within the Castile Formation and it is almost clastic free (Kerr and Thompson, 1963; Kelley, 1972). A common geomorphologic feature found in the Castile is the existence of Castile buttes. These are circular hills of limestone that may be found to extend as high as 30 m above the Gypsum Plain. When present in the subsurface, the accumulations are known as “Castile masses” (Adams, 1944). Sulfate reduction common during the Tertiary led to bioepigenetic replacement of anhydrite by calcite, forming these secondary limestones. These features may range anywhere from a few m² to a few hundred m². Nine informal units comprise the Castile: Basal Limestone, Anhydrite I, Halite I, Anhydrite II, Halite II, Anhydrite III, Halite III, Anhydrite IV, and the Painthorse members (Hill, 1996).

Salado Formation

The Salado is a halite formation with supplementary beds of anhydrite, polyhalite, potash salts and occasionally red sandy clay layers (Henrickson and Jones, 1952). These halite beds are composed of fine- to coarse-grained, clear halite with disseminated clay and polyhalite, in addition to laminae (Linn and Adams, 1966). The anhydrite beds present are gray, fine- to medium-grained and generally laminated with varves approximately five mm thick (Lang, 1935). Brick-

red, massive, and fine-grained polyhalite beds exist here, with potash salts occurring locally within the northern section of the Delaware Basin (Hill, 1996). Magnesite is also abundant within the Salado Formation (Stein and Krumhansl, 1988).

The three informal members of the Salado Formation include various formal members within their sequences. The Lower Member ranges in thickness from 100 to 300 m throughout the basin. This member contains the Fletcher Anhydrite, a 45 m thick halite zone, the La Huerta Siltstone, and the Cowden Anhydrite. The Fletcher Anhydrite and La Huerta Siltstone are each only found on the shelf today. Overlying these key beds is a zone 60 m in thickness consisting of alternating halite and anhydrite beds. The McNutt Potash Member, the middle section of the Salado Formation, consists of commercially valuable potash ore found mainly in the Carlsbad potash district near Carlsbad, New Mexico (Hill, 1996). The Upper Member consists of bedded halite, anhydrite, polyhalite, and clay approximately 150 m thick (Gard, 1968).

Rustler Formation

Extending from the Apache Mountains in the south to southeastern New Mexico in the north, the outcrop belt of the Rustler Formation displays the alternating transgressions and regressions of the Rustler Sea. Concurrent deepening and shallowing of the low-relief basin over multiple 20,000 year periods is visible (Lowenstein, 1987). Mudflat and saltpan environments were

created following a series of five major transgressions and episodes of isolation and evaporation (Powers and Holt, 1990; Holt and Powers, 1993). The Rustler Formation consists of dolomite, siltstone, anhydrite and halite (Mercer and Gonzalez, 1981). This lithology is similar to that of the Salado Formation, only with greater levels of dolomite and terrigenous clastics (Hentz et al., 1989). The total thickness is highly variable, ranging anywhere from 50 to 450 m (Hill, 1996).

The Rustler is separated into the Virginia Draw, Culebra Dolomite, Tamarisk, Magenta Dolomite, and Forty-Niner Members. The Virginia Draw Member occupies the lowest 20 to 50 m of the Rustler Formation (Hill, 1996). The first 15 m consist of dark reddish-brown to olive-gray siltstone, overlain by 10 m of gray brown, thin-bedded, finely-crystalline dolomite, followed by five m of amygdaloidal dolomite, siltstone and limestone (Miller 1992). This is often a cavernous unit filled with Cretaceous paleokarst. The Culebra Dolomite Member is approximately six to nine m thick, yellowish-gray to light gray, thin-bedded, laminated to finely-crystalline dolomite (Hill, 1996). This member is characterized by tiny, spherical vugs, two to 10 mm in diameter, which often contain selenite crystals (Snyder and Gard, 1982). The Tamarisk Member consists of halite and anhydrite, with minor siltstone and traces of polyhalite in the subsurface. At the surface this member is fairly undistinctive, light-gray, massive, coarsely-crystalline gypsum which appears to be severely altered by dissolution. The Magenta Dolomite Member is a reddish-brown dolomite, six to eight m thick,

alternating with gray anhydrite and buff siltstone-sandstone (Hill, 1996). The member is magenta in color, just as the name suggests, hosting thin, undulatory or wavy (Bachman, 1984) laminae 0.2 to five mm thick (Vine, 1963). The Forty-Niner Member is the uppermost portion of the Rustler. This member consists of anhydrite, siltstone and halite in the subsurface, with outcrops of massive gypsum interbedded with thin, reddish siltstone (Hill, 1996). Small caves, solutionally-enlarged joints and sinkholes are common in the surface (Vine, 1963).

Dewey Lake Red Beds Formation

Poorly-indurated, earthy, unfossiliferous, well-laminated, thin-bedded, reddish-brown to reddish-orange siltstone, followed by claystone and lenticular fine-grained sandstone make up the Dewey Lake Red Beds Formation. This unit is characterized by numerous light greenish-gray reduction spots, in addition to the occurrence of exceptionally-large, frosted quartz grains. Small-scale, cross-laminated, fine-grained sandstone becomes common in the upper part of the formation (Hill, 1996). The Lower Sequence is 28 m of mostly siltstone and mudstone with some interbedded claystone and sandstone, while the Upper Sequence is 115 m of thinly-laminated to cross-laminated sandstones and siltstones (Holt and Powers, 1990).

Post-Ochoan Stratigraphy

Anomalous occurrences of post-Ochoan age strata have been identified within the study area as paleokarst erosional remnants. The Cretaceous age Cox Formation is a brownish, thin- to massively-bedded quartz-pebble conglomerate. Additionally, the unit is made up of fine- to medium-grained sandstone. Gravel remnants of this formation have been found scattered in various locations across the Delaware Basin (Hill, 1996).

Tertiary intrusive bodies have also been identified as a series of northeast trending dikes (Hill, 1996). The dikes are considerably decomposed but, upon examination, have been described as lamprophyre of basaltic habit by C. S. Ross (Darton, 1928). The position of observed dikes appears to be controlled by joint orientations, as is the case in the Yeso Hills area (Hill, 1996). The dikes appear as rust colored, earthy material, occasionally containing small, sharp fragments of dark-colored, fine-grained igneous rock (Austin et al., 1993).

KARST AND SPELEOLOGY

Sinkholes, karren and surficial precipitates are common manifestation of surficial karst within the Gypsum Plain. Sinkholes are usually the most abundant karst geomorphic manifestation (Figure A4) (Stafford, et al. 2008A); these usually consist of shallow, surficial dissolution hollows formed by the collapse of bedrock

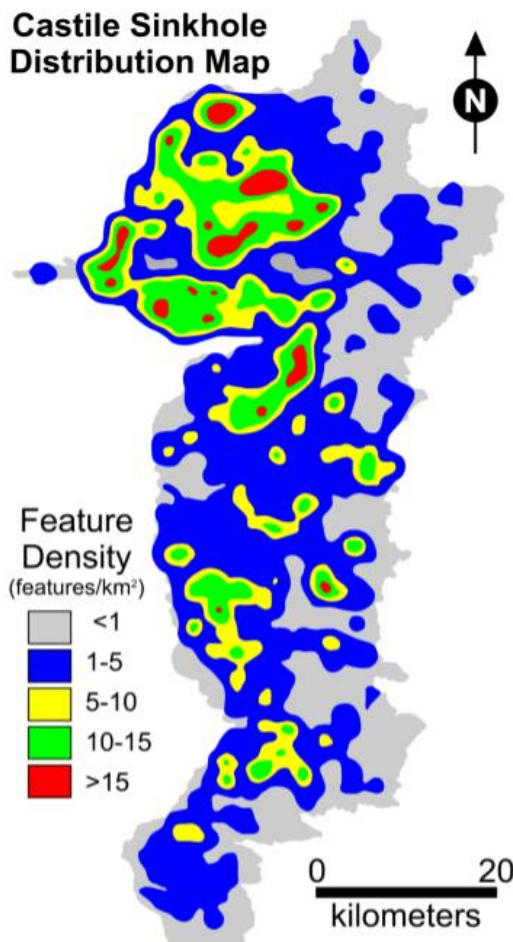


Figure A4: Example of the spatial distribution of karstic depressions within the Castile Formation (from Stafford, 2015).

into an underground void, and may be observed in both open and filled forms (Hill, 1996). Sinks are almost always the site of water percolating through the soil or bedrock into solutionally-enlarged drains (Palmer, 2007). Two dominant mechanisms control the formation of sinks; collapse of subsurface voids or the drainage of surficial waters. Sites due to collapse tend to appear as near-circular or elliptical features with walls that are near vertical. Sites created due to drainage of water from the surface consist of well-developed arroyos that converge to the

site of a central drain (Stafford et al., 2008A). Broad subsidence sinkholes and valleys may be caused by the dissolution of salt beds at depth (Smith and Veni, 1994). Another common type of sink present within the study area is a cenote, which appears as a sinkhole rimmed by steep, overhung, bedrock walls extending down to ponded water (Palmer, 2007).

Runoff may deeply etch exposed, bare, soluble bedrock. Steep slopes feature straighter rills, while sinuous channels are found on more gentle slopes. These surficial karst features are known as karren (Palmer, 2007). Various forms of karren are present within the study area, including: rillenkarrren, spitzkarren, and kamenitzas. Surficial precipitates are largely found as mm to cm thick crusts of gypsite covering exposed bedrock surfaces. This crust is due to the dissolution of the exposed gypsum. Macroflora are rarely found here, but lichen and microbial colonies are abundant (Stafford, et al., 2008A).

Epigene caves usually form a network of enlarged fissures and pores that take on a branchwork or dendritic design (Palmer, 2007). Epigene features are primarily isolated occurrences that tend to be well-developed, solutional, closed depressions which often form large, incised sinkholes connected to small solution conduits (Stafford et al., 2008A; Klimchouk, 2000). A common feature of the epigene caves located in the Gypsum Plain is well-developed, small-scale scallops along the walls, ceilings and floors. These scallops indicate the transport of large amounts of water at significant velocities through the cave passages

(White, 1988). Shallow groundwater recharge features are often associated with cave passages in the area (Stafford et al., 2008A). It is common for cave passages to initially open to a very limited size and narrow with length (Smith and Veni, 1994). This is caused by the fluids flowing through bedrock, forming the conduits described, quickly approaching saturation, making them unable to dissolve additional bedrock with depth.

Most observed epigenetic caves within the Gypsum Plain are laterally-limited, with development following prominent joint sets. With areas that have experienced higher levels of tectonism, caves may form along the fold axis of anticlines. Here rock compressions have produced fractures along the fold axis; both types previously described are small and laterally limited. Epigene caves may also form in the tabular gypsum fabrics found throughout the study area. These are the least common type, and are similar to those found in the gypsum bedrock in that they are also small. Gypsite epigene caves are also present, although these are usually too small to enter and plugged with soil (Stafford et al., 2008A).

In contrast, hypogene caves form below the surface of the earth, involving water at depth. Undersaturated reservoirs below the earth's surface deliver rising fluids, which cause dissolution of soluble rock units. Forced and free convection are the primary agents causing the rise of these fluids. Fluids deeper within the earth reside at a higher pressure, causing them to travel upward, to regions of

lower pressure. This movement by forced convection is driven by differences in hydraulic potential across the region. Free convection involves aggressive waters of a less saturated nature to rise via convection as more saturated waters descend deeper below the surface (Stafford et al., 2008A). The moment the waters come into contact with soluble rock, dissolution begins. Length of flow over which cave development takes place is often short, with a large ratio of discharge to flow length. Patterns have no or limited relation to surface karst features or recharge.

Hypogene caves include several types, but are most commonly seen as maze caves (Palmer, 2007). Morphometric features most often found include risers, outlets and half-tubes. Preferential flow paths connecting transmissive zones to soluble zones are indicated by cusped wall and floor features known as risers or feeders, respectively. Outlets, also known as cupolas, are ceiling structures that form domes. Ascending fluids continue to move to higher elevations and lower pressures by dissolving soluble rock in these areas. Where undersaturated fluids migrate from risers to outlets, concave, semi-circular channels are developed known as half-tubes. These tubes form vertically along walls or horizontally along ceiling passages. When each of these elements is found within a cave, it is reasonably assumed that the cave is of hypogene origin. Dense clusters of caves and sinkholes indicate similar derivation (Stafford et al., 2008A).

Direct evidence of the widespread occurrence of hypogene speleogenesis within the Delaware Basin is provided by the extensive brecciation and calcitization present. Both vertical breccia pipes and horizontal blanket breccias are widespread throughout the Castile, Rustler and Salado formations (Stafford, 2015). Lateral

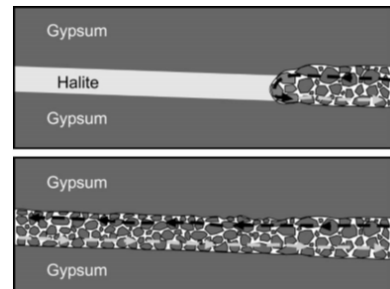


Figure A5: Diagram illustrating the formation of blanket-dissolution breccias through the dissolution of halite. Arrows represent fluid movement (from Stafford, 2015).

dissolution begins in the western portion of the basin, moves downdip, and dissolves salt horizons in the subsurface. Overlying strata collapse over time into

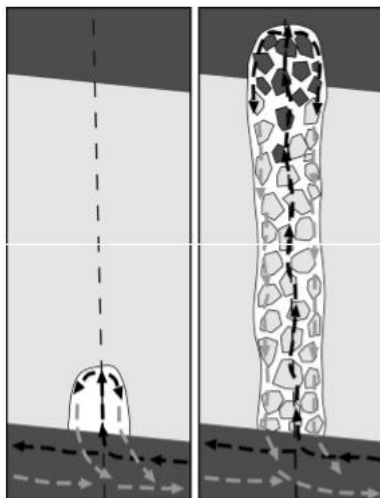


Figure A6: Diagram illustrating the formation of breccia pipes through the dissolution of halite. Arrows represent fluid movement (from Stafford, 2015).

these blanket void spaces, creating the blanket breccias observed (Figure A5). Vertical dissolution occurs in a similar manner as water moves up or down along vertical structures in a brine-density flow mechanism (Figure A6) (Stafford et al., 2008A).

These intrastratal breccia zones are often associated with calcitization. Bacterial Sulfate Reduction (BSR), Thermochemical Sulfate Reduction (TSR), and meteoric calcitization have all been attributed as the cause of calcite occurrences

within Delaware Basin strata. Commonly, these masses are found in conjunction with areas featuring hypogene karst or large amounts of selenite within the study

area. Native sulfur bodies are also in close proximity. Massive limestone buttes and laterally extensive limestone sheets are the general surface manifestations (Stafford et al., 2008c).

REMOTE SENSING

There are various advantages to using CIR (color infrared) imagery over other types of remotely-sensed imagery. Shorter, easily scattered wavelengths are filtered out using CIR. This allows for better penetration through atmospheric haze than normal color imagery. Stress levels of vegetation, moist areas and plant identification can all be revealed using CIR, which are undetectable on normal color imagery. Essentially, CIR was developed during World War II so that camouflaged tanks could be differentiated from the surrounding vegetation (Thompson, 2011).

Color infrared imagery is used to delineate surface features, such as sinkholes, vegetation types, lineaments, and major lithologies. CIR is a false color photograph that shows reflected electromagnetic waves from an object. Near infrared (NIR) is assigned to the red color band, green light is assigned to blue, and red light is assigned to green; blue light is completely filtered out, causing blue objects to appear black. Each object included in land cover absorbs a particular portion of the electromagnetic spectrum such that a portion of the light coming into contact with an object is transmitted and the remainder is reflected. This reflectance is recorded with a passive image system, most often

stationed on a satellite platform. These passive image systems act to detect and record specific wavelength ranges of reflected solar radiation (Thompson, 2011).

REFERENCES

- Adams, J. E. (1936). Oil pool of open reservoir type. *American Association of Petroleum Geology Bulletin*, 20, 780-796.
- Adams, J. E. (1944). Upper Permian Ochoa Series of Delaware Basin, West Texas and Southeastern New Mexico. *American Association of Petroleum Geologists*, 28, 1596-1625.
- Adams, J. E. (1965). Stratigraphic- Tectonic Development of Delaware Basin. *Bulletin of the American Association of Petroleum Geologists*, 49(11), 2140-2148.
- Austin, G. S., et al. (1993). First day road log from Carlsbad to White City, Orla, Loving, potash enclave and return to Carlsbad; in Love, D. W. et al. (eds.), *Carlsbad region, New Mexico and West Texas*. New Mexico Geol. Soc., Guidebook, Ann. Field Conf., 1-39.
- Bachman, G.O. (1984) Regional geology of Ochoan Evaporites, Northern Part of Delaware Basin. *New Mexico Bureau of Mines and Mineral Resources*, Open File 184
- Beck, R. H. (1967) Depositional mechanics of the Cherry Canyon Formation, Delaware Basin, Texas: Unpubl. MS thesis, Texas Technological College, 107.
- Darton, N. H. (1928). "Red Beds" and associated formations in New Mexico. *United States Geological Survey Bulletin*, 794, 356.
- Galley, J. E. (1958). Oil and geology in the Permian Basin of Texas and New Mexico. (L. G. Weeks, Ed.) *Habitat of Oil*, 395-446.

- Gard, L. M. (1968). Geologic studies, Project Gnome, Eddy County, New Mexico. *U.S. Geol. Surv., Prof. Paper* 589, 33.
- Henrickson, G. E., and Jones, R. S. (1952). Geology and groundwater resources of Eddy County, New Mexico: New Mexico Bur. Mines Mineral Resources, Groundwater Rept. 3, 109 pp.
- Hill, C. A. (1996). *Geology of the Delaware Basin, Guadalupe, Apache and Glass Mountains*. New Mexico and West Texas. Midland, Texas: Permian Basin Section- SEPM.
- Hentz, T. F., Price, J. G., and Gutierrez, G. N. (1989). Geologic occurrence and regional assessment of evaporite- hosted native sulfur, Trans-Pecos Texas. *Bur. Econ. Geol., Univ. Texas Austin, Rept. Invest.* 184, 70.
- Holt, R. M., and Powers, D.W. (1990). The Late Permian Dewey Lake Formation at the Waste Isolation Pilot Plant (WIPP); *in* Powers et al. (field trip leaders), *Geological and hydrological study of evaporites in the northern Delaware Basin for the Waste Isolation Pilot Plant (WIPP), New Mexico*. Geol. Soc. Am., Field Trip no. 14, 107-129.
- Holt, R. M., and Powers, D.W. (1993). Summary of the Delaware Basin endstage deposits; *in* Love, D. W., et al. (eds), *Carlsbad region, New Mexico and West Texas*. New Mexico Geol. Soc., Guidebook, 44th Ann Field Conf.90-92.
- Horak, R. L. (1985). Trans-Pecos tectonism and its affects on the Permian Basin. In P. W. Dickerson, & W. R. Muelberger, *Structure and Tectonics of Trans-Pecos Tecas* (pp. 81-87). Midland: West Texas Geological Society.
- Jenkins, R. E. (1961). Characteristics of the Delaware Formation *Jour. Petroleum Technology*, December, 1230- 1236.
- Jones, C. L. (1954). The occurrence and distribution of potassium minerals in southeastern New Mexico. *New Mexico Geol. Soc., 5th Field Conf.*, 107-112.

- Keith, S.B. (1982). Paleoconvergence rates determined from K₂O/SiO₂ ratios in magmatic rocks and their application to Cretaceous and tertiary tectonic patterns in southwestern north America. *Geological Society of America Bulletin*, 93, 524-532.
- Kelley, V. C. (1972). Geometry and correlations along the Permian Capitan escarpment, New Mexico and Texas. *Am. Assoc. Petroleum Geol., Bull.*, 56(11), 2192-2211.
- Kerr, S. D., and Thomson, A. (1963). Origin of nodular and bedded anhydrite in Permian shelf sediments, Texas and New Mexico. *Am. Assoc. Petroleum Geol., Bull.* , 47(9),1726- 1732.
- King, P. B. (1934). Permian stratigraphy of Trans-Pecos Texas. *Geol. Soc. Am., Bull.*, 45(4), 697-798.
- King, P. B. (1942). Permian of West Texas and southeastern New Mexico. *Am. Assoc. Petroleum Geol.*, 26(4), 535-763.
- King, P. B. (1948). Geology of the southern Guadalupe Mountains, Texas. *U.S. Geol. Surv., Prof. Paper* 215, 183.
- Klimchouk, A. (2000). Speleogenesis in gypsum; *in* Klimchouk, A., Ford, D. C., Palmer, A.N. and Dreybrodt, W. (eds.), *Speleogenesis: evolution of karst aquifers*. Hunstville, National Speleological Society.
- Koss, G. M. (1977). Carbonate mass flow sequences of the Permian Delaware Basin, West Texas; *in* Hileman, M. E. and Mazzullo, S. J. (eds.), *Upper Guadalupian facies, Permian Reef Complex*: Soc. Econ. Paleontol. Mineral., Permian Basin section, Publ. 77-16.
- Lang, W. B. (1935). Upper Permian Formation of Delaware Basin of Texas and New Mexico. *Am. Assoc. Petroleum Geol.*, 19(2), 262-270.

- Lawson, E. C. (1989a). Megabreccias and associated carbonates of the Rader Member, Capitan Reef Complex (Permian), Delaware Mountains, West Texas (abs.); *in* Pray, L. C. and Harris, P. M. (eds.), *The Capitan Reef Complex, West Texas and New Mexico*: Soc. Econ. Paleontol. Mineral., Permian Basin section, Field Trip Sem. No. 1.
- Lawson, E. C. (1989b). Subaqueous gravity flows in the Rader Member, Capitan Reef Complex (Permian), Delaware Mountain, West Texas; *in* Harris, P. M. and Grover, G. A. (eds.), *Subsurface and outcrop examination of the shelf margin, northern Delaware Basin*. Soc. Econ. Paleontol. Mineral., Core Workshop no. 13.
- Linn, K. O., and Adams, A. A. (1966). Barren halite zones in potash deposits, Carlsbad, New Mexico; *in* Rau, J. L. (ed.), *Second Symposium on Salt*. Northern Ohio Geol. Soc., Cleveland, OH, v. 1.
- Lowenstein, T. K. (1987). Depositional cycles in the Permian Salado Formation, southeastern New Mexico; *in* Powers, D. W. and James, W. C. (eds.), *Geology of the western Delaware Basin, West Texas and southeastern New Mexico*. El Paso Geol. Soc., Guidebook 18.
- Mercer, J. W., and Gonzalez, D. D. (1981). Geohydrology of the proposed Waste Isolation Pilot Plant Site in southeastern New Mexico; *in* Wells, S. G. and Lambert, W. (eds.), *Environmental geology and hydrology in New Mexico*. New Mexico Geol. Soc., Spec. Publ. 10.
- Miller, L. J. (1992) Sulphur ore controls within the Salado and Castile Formations of West Texas; *in* Wessel, G. R., and Wimberly, B. H., (eds.), *Native sulfur – developments in geology and exploration*. Soc. Mining, Metallurgy, Exploration, Proc., Phoenix, AZ, Ch 1.
- Palmer, A. N. (2006). *Cave geology*. Dayton, OH: Cave Books.
- Powers, D. W., and Holt, R. M. (1990). Sedimentology of the Rustler Formation near the Waste Isolation Pilot Plant (WIPP) site; *in* Powers et al. (field trip leaders), *Geological and hydrological studies of evaporites in the northern*

Delaware Basin for the Waste Isolation Pilot Plant (WIPP), New Mexico.
Geol. Soc. Am., Field Trip no. 14.

Scholle, P. A., and Halley, R. B. (1980). Upper Paleozoic depositional and diagenetic facies in a mature petroleum province (a field guide to the Guadalupe and Sacramento Mountains). *U.S. Geol. Surv.*, Open-file Rept. 80-383.

Scholle, P. A., Ulmer, D. S., and Melim, L. A. (1992). Late-stage calcites in the Permian Capitan Formation and its equivalents, Delaware Basin margin, West Texas and New Mexico—evidence for replacement of precursor evaporites. *Sedimentology*, 39, 207- 234.

Smith, A. R., and Veni, G. (1994). Karst Regions of Texas; *in The caves and karst of Texas: a guidebook for the 1994 Convention of the National Speleological Society with emphasis on the Southwestern Edwards Plateau*. Brackettville, TX: National Speleological Society.

Snyder, R. P., and Gard, L. M. (1982). Evaluation of breccia pipes in southeastern New Mexico and their relation to the Waste Isolation Pilot Plant (WIPP) site. *U.S. Geol. Surv.*, Open-file Rept. 82-968.

Stafford, K. W. (2013). Evaporite karst and hydrogeology of the Castile Formation: Culberson County, Texas and Eddy county, New Mexico; *in* Land, L., Doctor, D. H., and Stephenson J. B., (eds.), *NCKRI Symposium 2: Proceedings of the 13th Multidisciplinary Conference on Sinkholes and the Engineering and Environmental Impacts of Karst*. Carlsbad, NM: National Cave and Karst Research Institute.

Stafford, K.W. (2015). Evaluation of Existing Geologic Conditions along RM 652: Initial Characterization of Karst Geohazards Associated with RM 652 in Culberson County, Texas. *TxDOT* rep.

Stafford, K., Nance, R., Rosales-Lagarde, L., and Boston, P. (2008a). Epigene and hypogene gypsum karst manifestations of the Castile Formation:

Eddy County, New Mexico and Culberson County, Texas, USA.
International Journal of Speleology, 37, 83–98.

Stafford K.W., Rosales-Lagarde L. and Boston P.J. (2008b). Castile evaporite karst potential map of the Gypsum Plain, Eddy County, New Mexico and Culberson County, Texas: a GIS methodological comparison. *J. Cave and Karst Studies*, 83-98.

Stafford, K.W., Klimchouck, A.B., Land, L., and Gary, M.O. (2009). The Pecos River hypogene speleogenetic province: a basin-scale karst paradigm for eastern New Mexico and west Texas, USA, *In* Stafford, K.W., Land, L., and Veni, G. (eds), *NCKRI Symposium 1: Advances in Hypogene Karst Studies*. Carlsbad, New Mexico: National Cave and Karst Research Institute.

Stafford, K.W., Ulmer-Scholle, D., and Rosales-Lagarde, L. (2008c). Hypogene calcitization: Evaporite diagenesis in the western Delaware Basin. *Carbonates and Evaporites*, 23, 89–103.

Stein, C. L., and Krumhansl, J. L. (1988). A model for the evolution of brines in salt from the lower Salado Formation, southeastern New Mexico: *Geochim. Acta*, 52, 1037-1046.

Thompson, G. (2011). Using Color Infrared (CIR) Imagery: A Guide for Understanding, Interpreting, and Benefiting from CIR Imagery. *Statewide Mapping Advisory Committee*, 22 pp.

Vine, J. D. (1963). Surface geology of the Nash Draw Quadrangle, Eddy County, New Mexico. *U.S. Geol. Surv.*, Bull 1141-B, B1-B46.

White, W. B. (1988). *Geomorphology and Hydrology of Karst Terrains*. New York: Oxford University Press.

Williamson, C. R. (1980). Sedimentology of Guadalupian deep-water clastic facies, Delaware Basin, New Mexico and West Texas; *in* Dickerson, P.

W., and Hoffer J. M. (eds.), *Trans-Pecos Region*. New Mexico Geol. Soc., Guidebook, 31st Field Conf., pp. 195-204.

APPENDIX B

DETAILED METHODOLOGY

IMAGE ANALYSES

Cave and karst phenomena of the Gypsum Plain are commonly present in an area associated with certain lithologies, especially that of paleokarst features. Recent advances in available resolution of commercial Color Infrared (CIR) imagery have enabled large-scale characterization of geologic variability, that, when coupled with geospatial analyses, allows features of interest to be more readily and accurately identified than ever before. Fifty cm resolution WorldView-2 CIR satellite imagery of the study area totaling approximately 100 km² (Figure B1), shot on September 27, 2016, was purchased by Stephen F. Austin State University, Department of Geology for use in this study.

Before beginning analyses of the CIR imagery, control points were established during fieldwork using a Garmin Rino 650 handheld GPS unit. Areas suspected of representing each type of lithology present within the study area were systematically identified using Google Earth Pro, locations noted, and physically surveyed in the field. Those locations were verified to contain karst-related features or lithologies, such as sinkholes or areas of calcitized gypsum were photographed, detailed descriptions were recorded, and GPS locations obtained. This resulted in a control point database of locations of each type of lithology, water body, and anthropogenic feature found within the study area

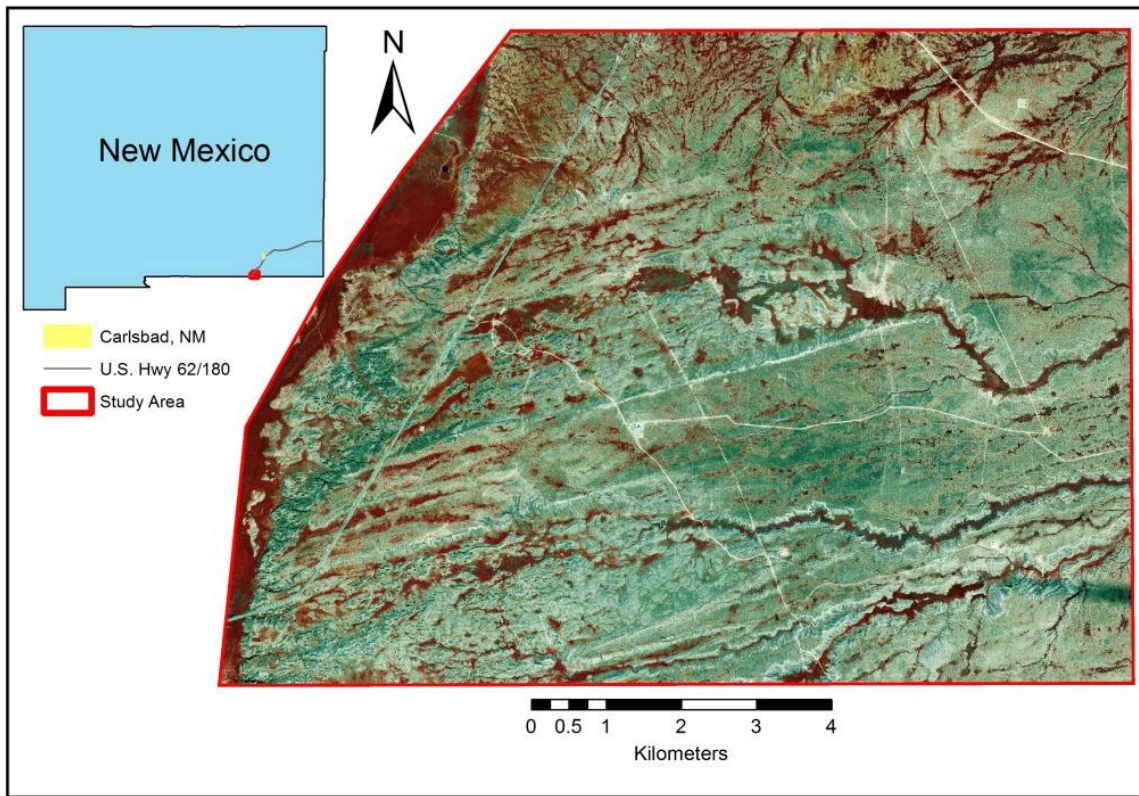
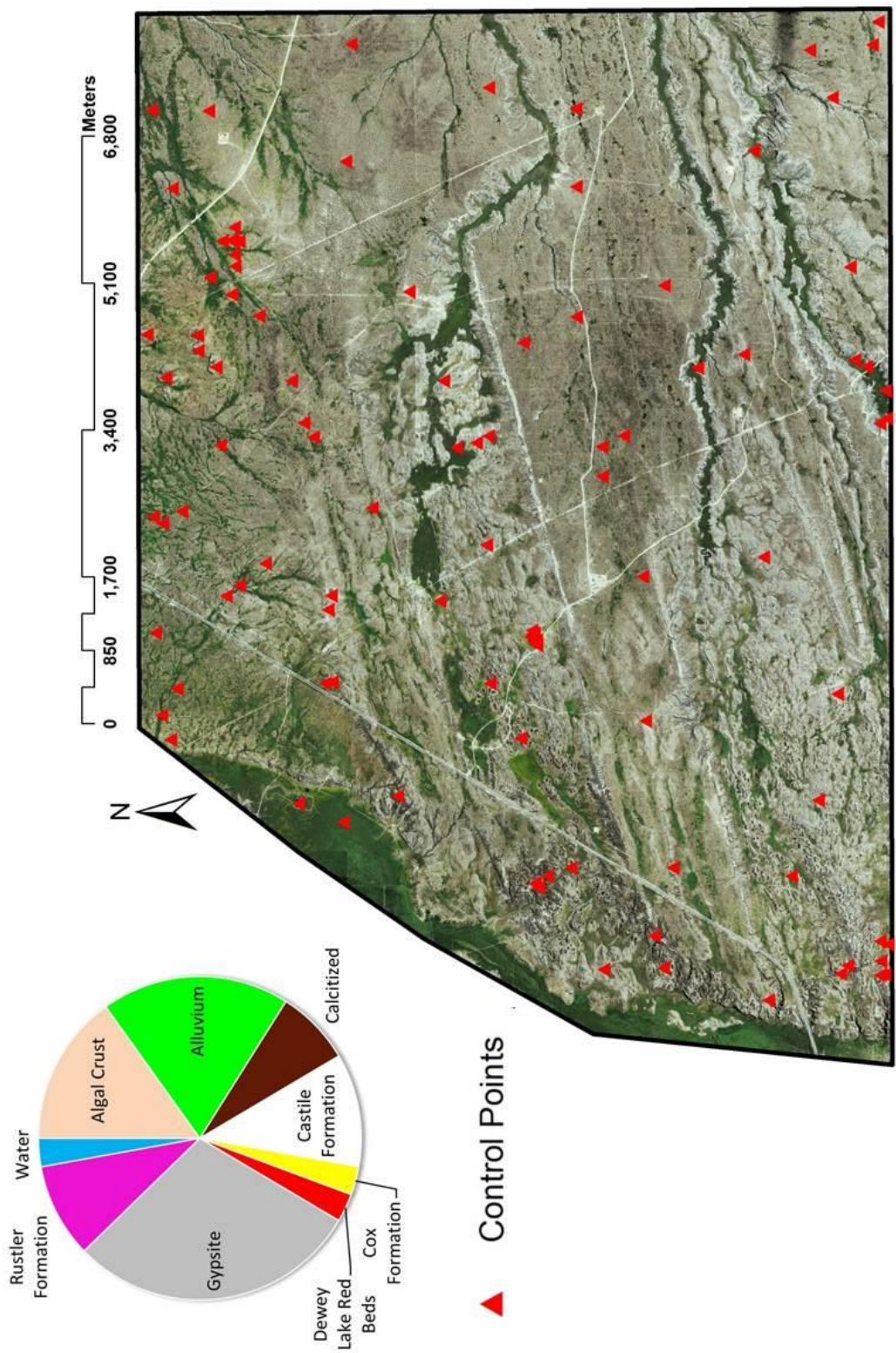


Figure B1: Index map of study area showing WorldView-2 CIR imagery

(Figure B2). Features corresponding to ‘Vegetation’ such as bushes and trees were selected directly within the color infrared image, rather than as control points in the field to account for any temporal change in the presence of vegetation between the time that the imagery was captured and field checks were performed.

Pre-processing of the image was performed before purchase of the CIR product, including orthorectification, a dark object subtraction and atmospheric corrections related to haze and visibility of the image in accordance with DigitalGlobe’s Atmospheric Compensation (AComp) model. Further processing



▲ Control Points

Figure B2: Location of each control point identified and field checked for nine of the 10 classes used for later classification of the color-infrared data set (Not including control points established for "Vegetation"). Chart (top left) details the number of control points across the landscape corresponding to each class identified in the field.

performed on the CIR image before it could be classified involved a conversion of the raw digital number (DN) values of the raster into top-of-atmosphere spectral radiance, followed by a conversion to top-of-atmosphere reflectance as outlined by Updike and Comp (2010).

The CIR file was imported into ESRI ArcGIS for Desktop in the form of an enhanced compression wavelet (ECW) in order to identify areas correlating to the control points documented in the field. Using the Training Sample Manager within the Image Classification Toolbar in ArcGIS, training samples were created by drawing polygons around areas corresponding to the control points that were taken in the field. Once several training samples had been established for each type of control point, the training samples were converted into a Signature File using the Create Signature File Tool within the Image Classification Toolbar. The generated signature file associated the number of cells within each of the polygons of the associated training sample, along with the mean and covariance matrices to the corresponding class type. The statistical values were computed based on the spectral signature cell value for each of the bands within the CIR image (Figure B3). A signature file is necessary to run a Maximum Likelihood Classification on the image.

Classification classes consisted of: 1) alluvium, 2) algal crust, 3) dense vegetation manifesting usually as bushes one-quarter to several m² in area, 4) calcitized breccia zones or float, 5) exposed Castile gypsum bedrock,

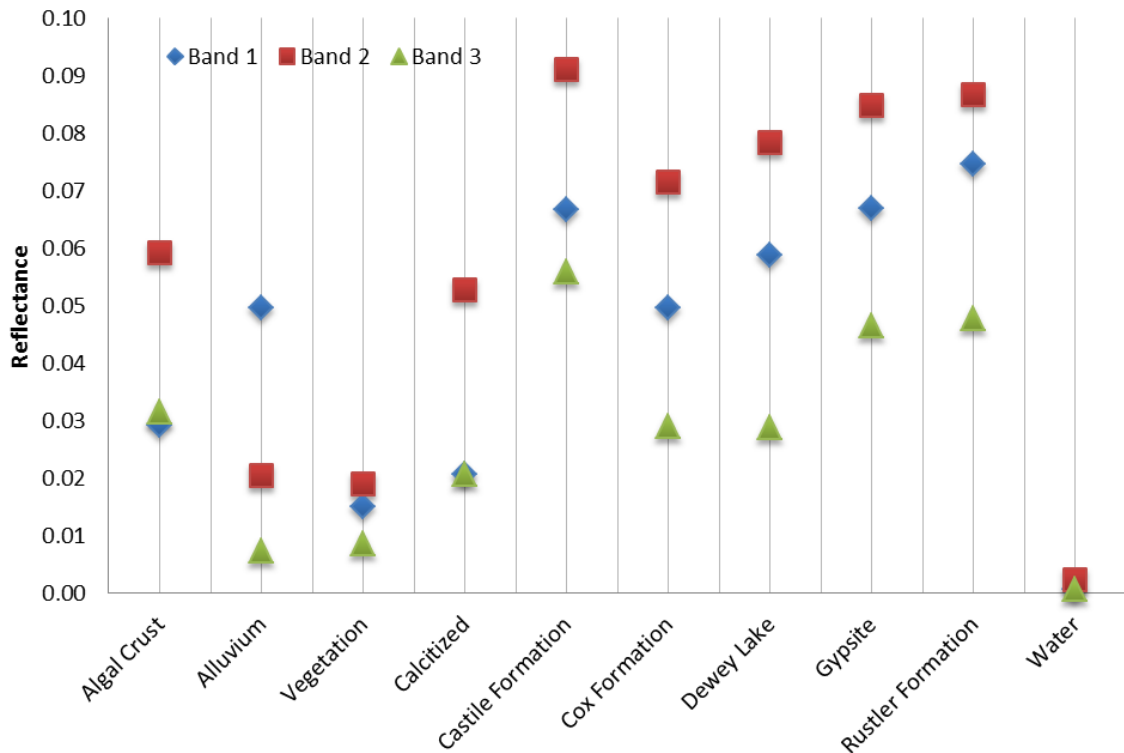


Figure B3: Graph displaying the mean reflectance value of each band for the corresponding training samples, calculated and assigned within the Create Signatures File tool.

6) residual Cox strata, 7) residual Dewey Lake Red Beds strata, 8) surficial gypsite precipitates, 9) residual Rustler strata, and 10) surface bodies of water. 'Bushes' values include all forms of vegetation large enough to be identified by the resolution of the original CIR image, including trees. Major anthropogenic features such as roads and wastewater evaporation ponds were originally classified by their major lithology types, but removed from the Training Sample Manager due to their spectral signature statistics being slightly different (due to human activity) than that of unmodified rock of the same type elsewhere within the study area. The output signature file created from each of the two training

samples was then used to perform a Maximum Likelihood Classification, found in the ArcGIS Multivariate toolset within the Spatial Analyst Toolbox, on the entire CIR image. The tool employs an algorithm that considers the variance and covariance of each cell within an image and assigns it to one of the classes represented in the input signature file that it most likely corresponds to. The algorithm operates on the principle of Bayes' theorem of decision making where cells in each class sample are normally distributed, allowing them to be characterized by their corresponding mean vector and covariance matrix (ArcGIS Resources, 2014).

Tool parameter options include the ability to specify a priori probabilities of each class if the likelihood of the occurrence of some classes is higher, or lower than others. A SAMPLE a priori option was used within this study, assigning the probability of each class' occurrence as proportional to the number of cells that make up the training sample class relative to the total number of cells in the image. Consequently, those classes more common across the study area (gypsite, algal crust) that correspond to training samples made up of a greater number of cells than those classes less common across the study area (Cox and Dewey Lake carbonates) were assigned a greater probability of occurrence (Figure B2). For the purpose of eliminating extraneous noise from the final classified image, a reject factor was also specified as a tool parameter. During classification the Maximum Likelihood Classification tool calculates a confidence

value directly correlating the distance to the mean vector of the assigned class with the percent confidence in which the cell is classified by the program. Those cells with less than or equal to 5% confidence in the assigned value were not classified and received a “No Data” value.

The output classification file was a raster file with each cell of greater than 5% confidence assigned a class value from the input signature file. With the purpose of classifying the entire study area by lithology, vegetation was then assigned to a corresponding lithology in which it is growing. It may logically be assumed that the lithology from which plants originate is that of their nearest neighbor based on observations recorded within the field and verified within the output classified images. Using the Reclassify tool, located within the Spatial Analyst Toolbox’s Reclass Toolset in ArcMap, all values identified as ‘Bushes’ were also assigned a ‘NoData’ value.

The Nibble Tool, also located in the Spatial Analyst Toolbox, in the Generalization toolset, was used to replace the original cell values of ‘Bushes’ and those cells classified as ‘No Data’ in the original classification , with the corresponding values of their nearest neighbor according to Euclidean distance. An algorithm used by the tool first identifies all cells within a mask raster with a value of ‘NoData’ (ArcMap, 2016). Those cells in the original raster corresponding to the ‘NoData’ values of the mask raster were then “nibbled” and replaced by their nearest neighbor value; the output “nibbled” raster is the final

product classifying the entire image by lithology (Figure B4). Once all values within the classified raster have been assigned a lithology, the map produced may be used for field studies or further processing depending on the goals of the user.

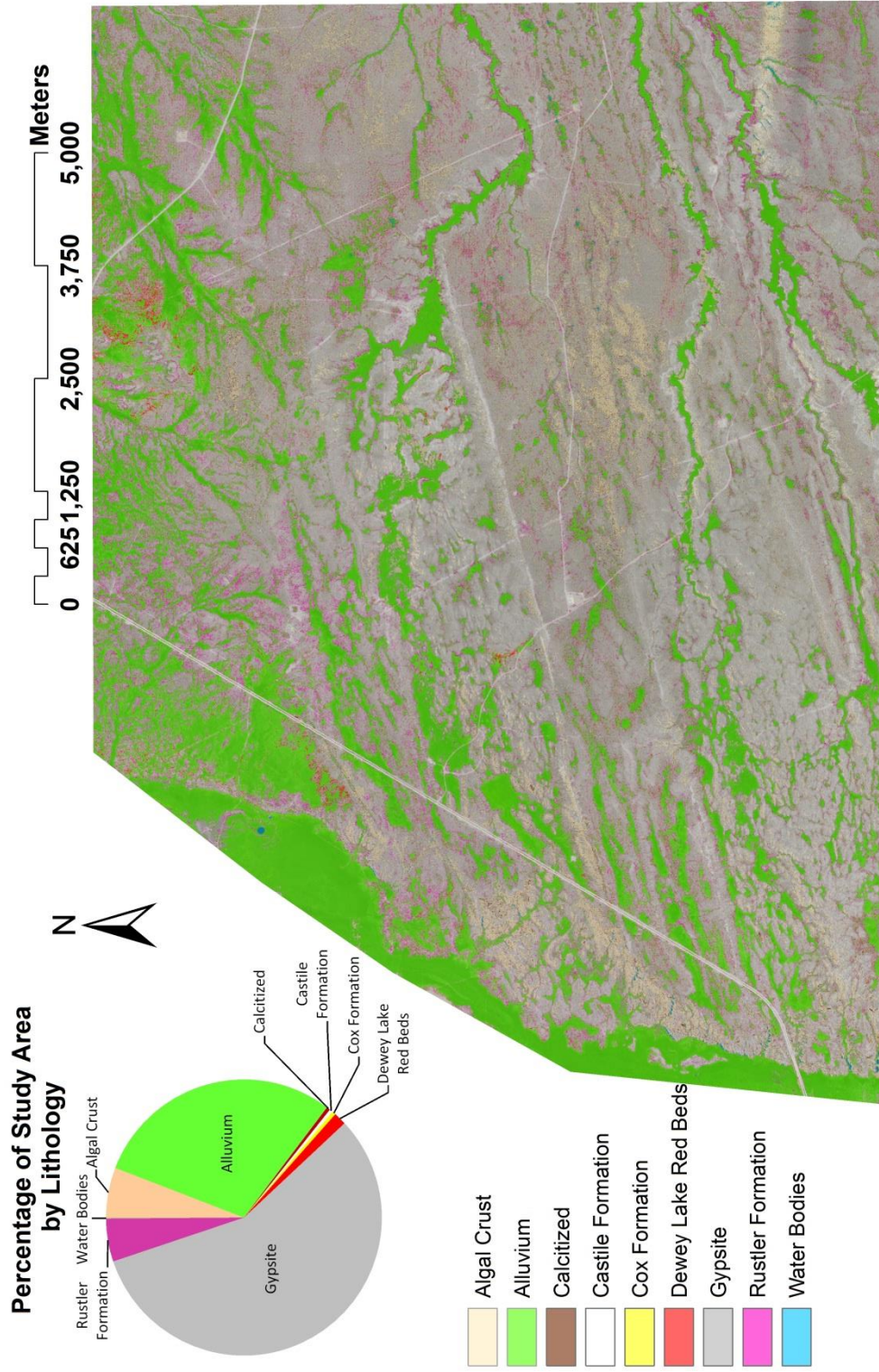


Figure B4: Final lithologic surface map of the study area based on the maximum likelihood classification performed.

KARST SURVEY

In order to understand the speleogenetic evolution of the study area and greater Gypsum Plain, spatial analyses of cave features discovered was performed through physical cave mapping and the production of illustrated cave maps. Through these processes structural controls, general trends, flow paths and morphology were identified and recorded. Spatial distribution of features is important to establishing the hydrogeologic framework and controls present.

Before any survey of cave features began, features were systematically identified by teams physically traversing 10, one km² grids placed strategically across the 100 km² study area (Figure B5). Grid locations were based on known areas of interest and areas expected to contain significant numbers of features. Each grid was converted into a series of traverse lines approximately 50 m apart. Equipped with a camera, Rite in the Rain All Weather Universal field notebook, and Garmin Rino 650 handheld GPS unit, each traverse line was slowly walked and any feature of interest indicating the presence of karst was photographed, documented, and its GPS location recorded. Features of interest documented along the traverse lines included sinkholes, cave entrances, solutional conduits, vent structures, calcitized areas, and changes in lithology.

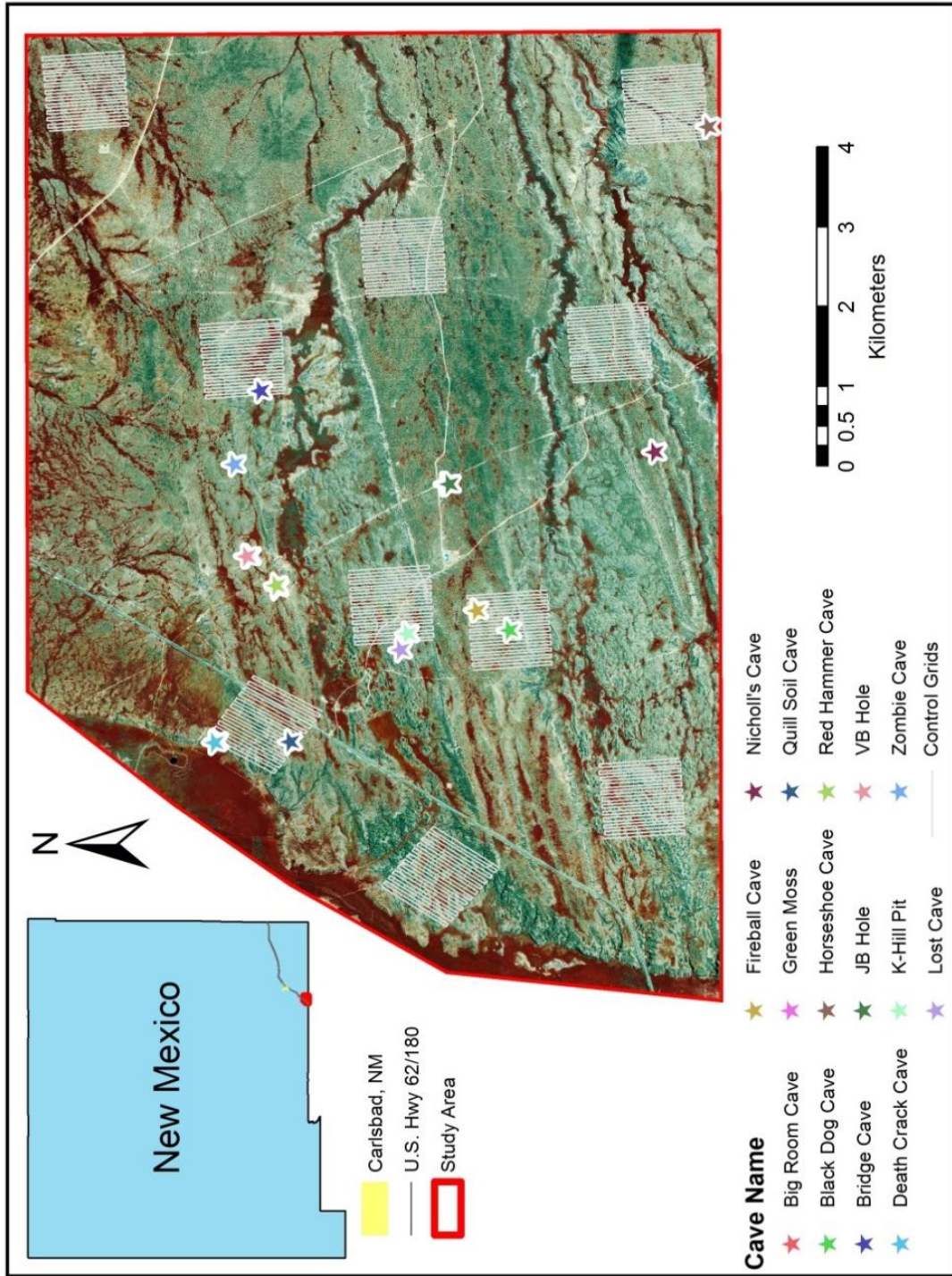


Figure B5: Location map of control grids walked to identify cave and karst features. Caves that were surveyed are marked by a star symbol.

All humanly enterable cave features identified within each of the 10 control grids, in addition to a number of features identified outside of the grids, were surveyed. Teams of two to three people conducted surveys using a Disto rangefinder, and Suunto compass/clinometer. The lead person entering the cave

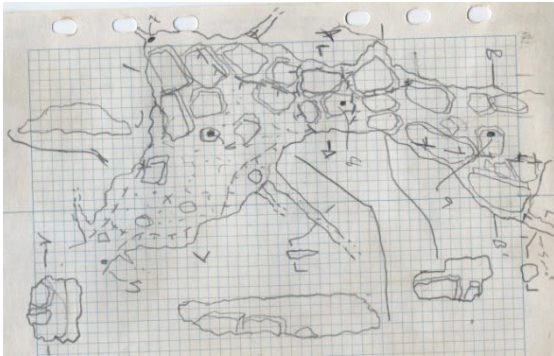


Figure B6: Example of field sketches containing morphological features from JB Hole.

acted as a scout and identified the point to which the second person entering the cave would perform instrument readings. Distance, azimuth and inclination were measured by this second team member at point (A), to the lead team member at point (B). The

collected data was recorded and all plan, profile and cross-sectional views were sketched in a Rite in the Rain All Weather Field Binder, according to National Speleological Society protocol (Dasher, 1994). Once general sketches had been drawn, geomorphic details such as rock types, floor and ceiling drops, fractures, and features indicative of either hypogene or epigene origin were added (Figure B6).

Once data was recorded and all sketches finished, the values were entered into Walls, a free program available through the Texas Speleological Survey designed for the analysis of cave survey data. Once a new project and item are created, the value of the “from point” is entered into column one, “to

#U	O=dva			
0	1	2.185	-23	82
1	2	2.510	-12	1
2	3	1.662	-16	322
3	4	12.879	1.5	35
3	5	3.424	-10	334
5	6	4.055	0	310
6	7	3.259	21	210
6	8	3.795	16	352
8	9	3.831	-6	11
9	10	2.748	19	355
9	11	4.976	-5	7
11	12	2.934	1	3.5
12	13	3.586	-2	27
13	J7	2.325	-22	7
J7	J1	1.723	11	103
J1	J2	3.17	4	211
J2	J3	1.43	-8	160
J3	J4	4.74	-4	231
J4	J5A	4.385	-1	258
J4	J5B	0.745	7	311
J5B	J6	3.424	-9	202

Figure B7: Example of Walls input file containing field measurements of point locations and their corresponding length, inclination, and azimuth.

point” entered into column two, followed by the length, inclination and azimuth in columns three, four and five, respectively (Figure B7). Walls compiles this input information to produce line plots of the profile and plan of the cave, in addition to statistics such as total passage length and depth (Figure B8).

The plan and profile views created by Walls were then imported into a blank Xara Xtreme 5 document, an illustration program used to digitize the field sketches. The field sketches were also

imported and overlain transparently on top of the Walls line plot by corresponding survey points in order to preserve scale. The plan, profile, and cross-sectional sketches were then digitized using the drawing tools within Xara.

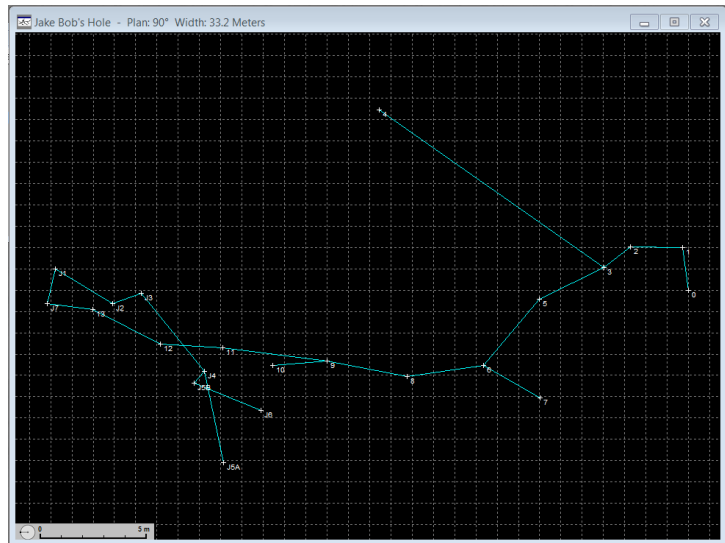


Figure B8: Plan view line plot generated by Walls from data collected in the field.

Once the drawing of the cave map is complete basic cartographic attributes were

added and the image was exported for publication. Vertical relief and relationship of all cave passages and features may now be assessed for a greater understanding of the speleogenetic history of the cave.

REFERENCES

- ArcGIS Resources. (2014). How Maximum Likelihood Classification works. (n.d.). ArcGIS Help 10.2.
- ArcMap. (2016). Generalizing zones with Nibble, Shrink, and Expand. ArcGIS for Desktop.
- Dasher, G. R. (1994). On station: a complete handbook for surveying and mapping caves. *National Speleological Society*.
- Udike, T. and Comp, C. (2010). Radiometric use of WorldView-2 imagery. *Digital Globe*. Technical note, 1-17.

APPENDIX C

CAVES AND KARST

CAVE INVENTORY

Speleogenetic history and formation conditions were determined through the performance of traditional cave surveying and drafting techniques using standard cave symbology. Caves exhibiting both epigenetic and hypogenetic characteristics were identified within the study area. The following is a description of each of the features found within the study area control grids and surrounding area considered that were large enough to physically enter and study. A total of 15 caves were mapped in the study area (Figure C1)

Bridge Cave

Bridge Cave (Figure C2) features a survey length of 86 m and depth of six m. The cave entrance is located in the bottom of the eastern most of two sinkholes, separated by a bridge-like structure formed by dissolution of gypsum bedrock (Figure C1). The entrance is partially blocked by a large boulder of bedrock, with an accessible opening of approximately one-half m in diameter. The adjacent sinkholes are a combination of gypsum bedrock and gypsic soil.

The cave passage maintains a constant size of approximately three m tall and one-half to one m wide for the initial 40 m of passage, slowly descending. The floor is generally gypsum bedrock with soil and bedrock float. The passage narrows to one m tall and slowly continues to narrow from one-half m in diameter

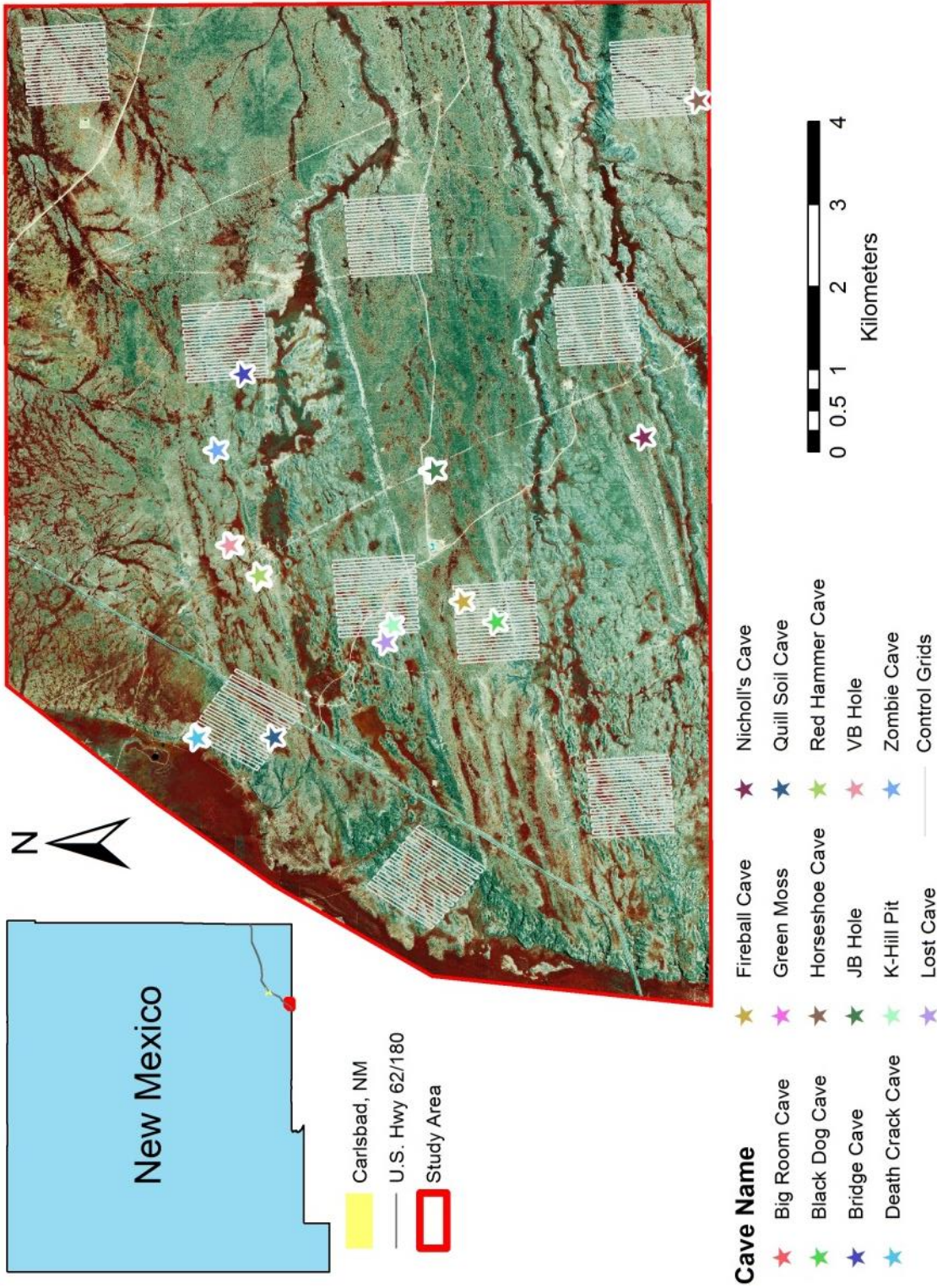


Figure C-1: Map of the study area detailing cave and control grid locations.



Figure C2: Drafted cave map of Bridge Cave.

to one-quarter m over the following 35 m until it is no longer accessible for survey. The final 10 m of passage is made up of gypsum bedrock floor and walls, but dissolution of the original ceiling and infilling of sediment has created a current ceiling of organic soil. All passages exhibit the characteristics of a classic tubular epigene passage formed in the phreatic zone that has become entrenched by vadose processes. Together these processes have culminated in the piping of soil into the eastern end of the cave by suffosion.

Death Crack and Big Room caves

Death Crack Cave (Figure C3) is the western most of two caves located in the northwest portion of the study area, west of U.S. Highway 62/180 (Figure C1). Both caves have undergone recent and extensive collapse of their original structure, due to dissolution of gypsum by vadose processes. They are located within a gypsum escarpment that lies along the edge of the Gypsum Plain, proximal to the Guadalupe Mountains. Death Crack Cave is an almost vertical multi-level shaft originating within the center of a soil and bedrock arroyo eight m in diameter and five m deep. The opening of the cave itself is two m long and one m wide. The vertical shaft drops 10 m, reaching the middle and largest level. Three passages, originating in a center room three m wide and five m long, follow the fracture of the bedrock walls outward before terminating in collapse. Down the original shaft another five m, the lower level terminates in a soil- and collapse-filled drain that forms a funnel within the floor. The walls of this section

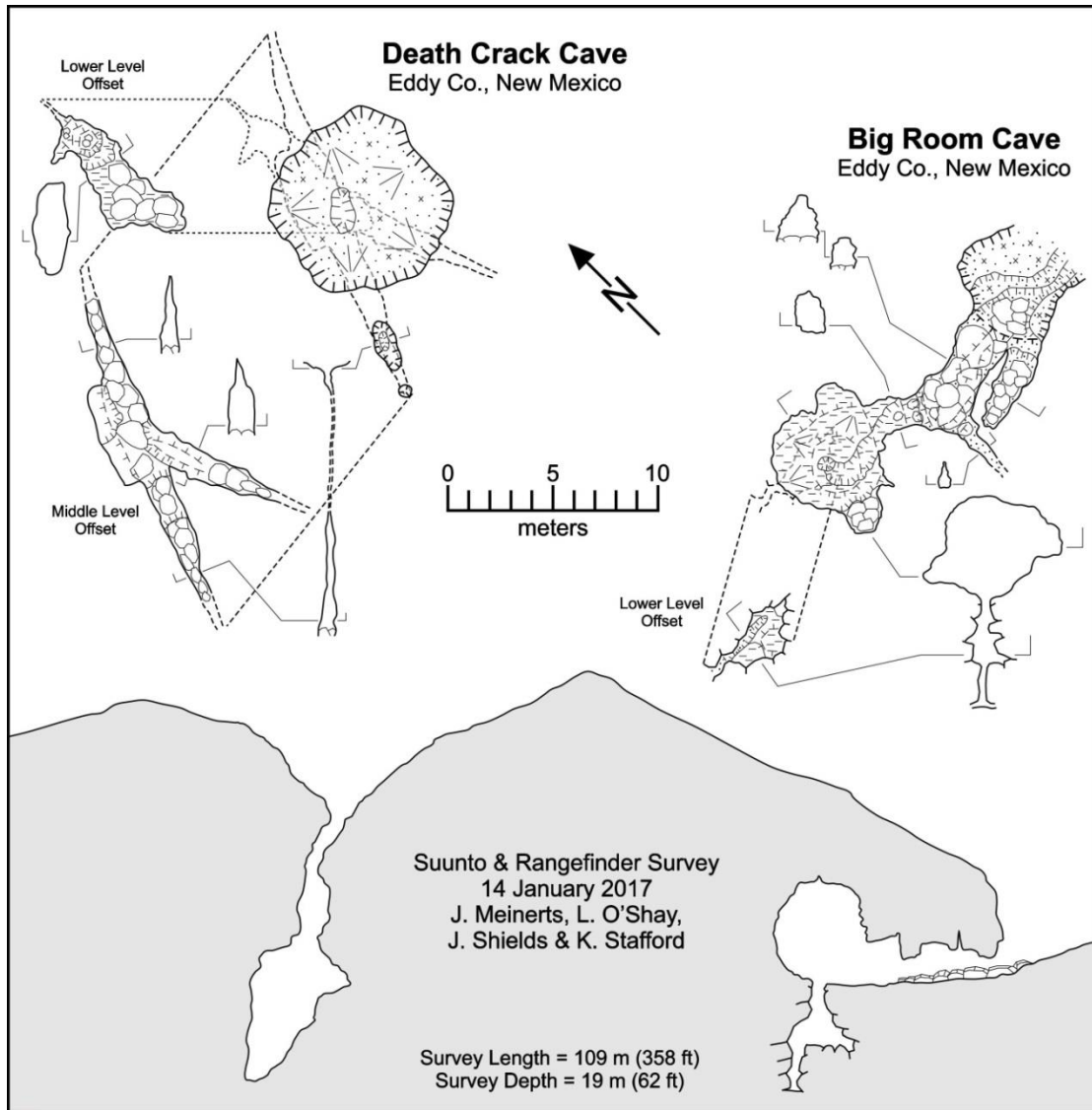


Figure C3: drafted cave map of Death Crack and Big Room caves.

of the cave are highly fractured bedrock, with large unstable slabs slowly shearing away due to dissolution of the rock.

Located 45 m southeast of the entrance to Death Crack Cave is Big Room Cave, the remnants of a collapsed room and cave passage. The entrance to Big

Room Cave is located in a soil and bedrock sinkhole within the side of the gypsum escarpment. At the base of a five-m-tall headwall, a hole two m wide and one-m-tall opens to a passage of solid bedrock ceiling and walls formed of gypsum collapse. This passage continues for approximately seven m before opening into a large room seven m in diameter and seven-m-tall. The floor in this area is a large accumulation of damp soil, derived from the gypsic soil ceiling and brought in by the flow of surficial waters. The walls adjacent to the lithified soil ceiling are highly fractured bedrock slabs arching to form the dome ceiling. The center of the soil floor features a vertical passage one-half-m in diameter and five-m-deep, completely made of collapsed bedrock held together by soil. The passage has been reopened from the original collapse by large flows of surface waters.

At one time Death Crack and Big Room caves were most likely one epigene passage connected via the area of collapsed in the bottom of Big Room cave, indicated by the trend of the lower collapse passage and the ease with which sound is carried between the caves. Other caves, primarily consisting of unstable bedrock collapse are also located in the northern portion of the gypsum escarpment. Collapse of the caves within the escarpment is due to the preferential flow of vadose and phreatic waters along the slope of the Gypsum Plain and through the escarpment to reach the Black River Valley separating the Guadalupe Mountains and the escarpment. The increased flow through this area

has caused greater dissolution of the gypsum bedrock forming Death Crack and Big Room caves than other caves in the study area, leading to more extensive and multiple episodes of collapse.

Fireball Cave

Fireball Cave (Figure C4) is located in the central portion of the study area (Figure C1) and is 13 m long and three m deep. The cave begins in a soil and bedrock sink three m in diameter before forming a bridge structure. On the opposite side of the bridge, the cave entrance is one m in diameter and opens to a passage approximately one-half-m in diameter. The passage continues three m before narrowing and becoming impassable. The cave passage is formed entirely within gypsum bedrock and the floor is covered in soil. The ceiling of the cave exhibits fracture control patterns while scalloped walls indicate rapid flow of surface waters into the epigene cave. At one time the bridge structure formed the main entrance to the cave connected to the second entrance by gypsum bedrock. Overtime fluid flow has caused the dissolution of that bedrock that once covered the sinkhole between the two entrances.

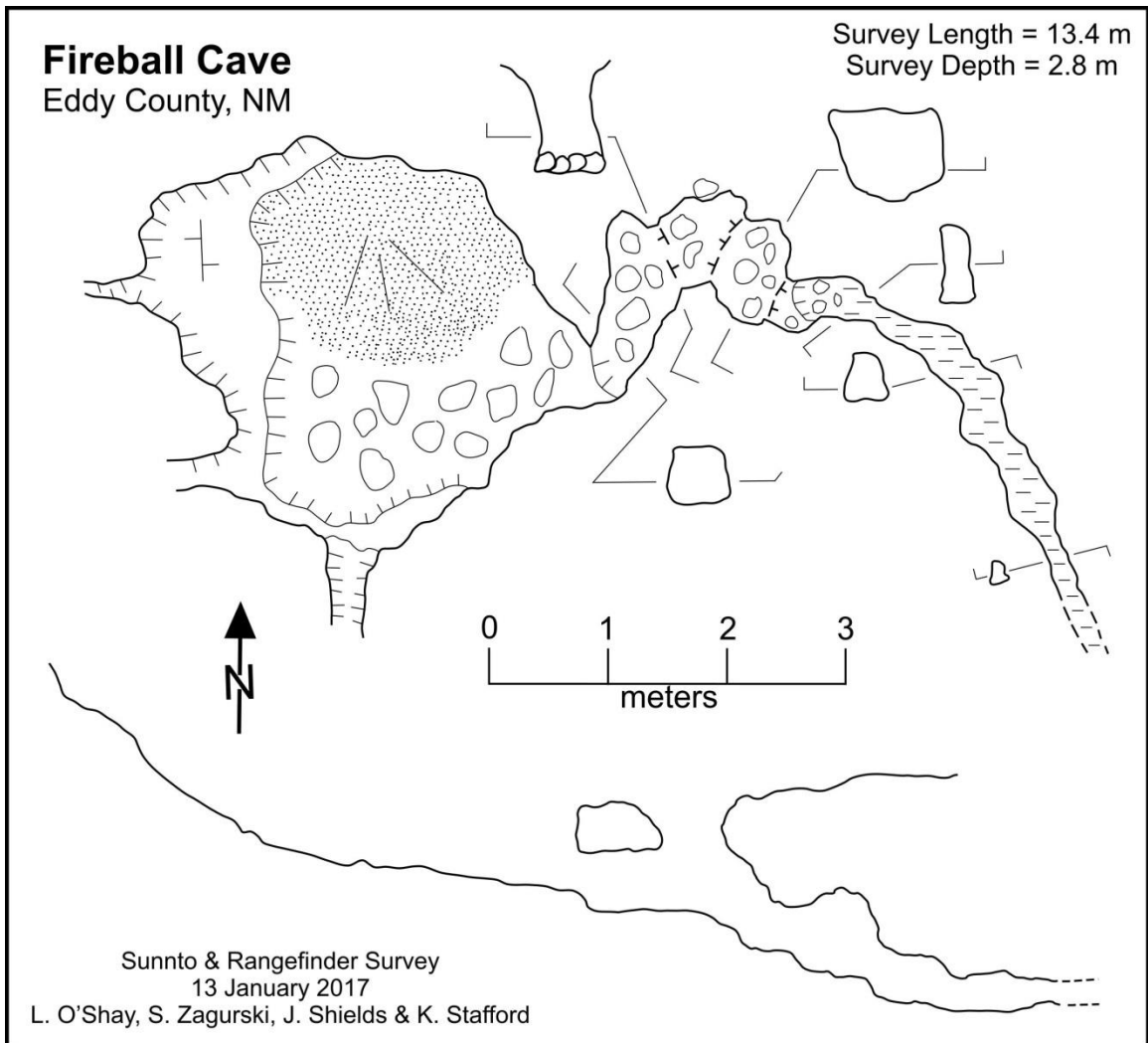


Figure C4: drafted cave map of Fireball Cave.

Green Moss Cave

Green Moss (Figure C5) is a traditional epigene karst feature with some hypogene characteristics, located just west of Red Hammer (Figure C1) With a survey length of 67 m and a depth of 11 m, Green Moss is one of the longest caves found within the study area. The entrance to the cave is approximately two m tall by three-fourths-m wide opening at the base of

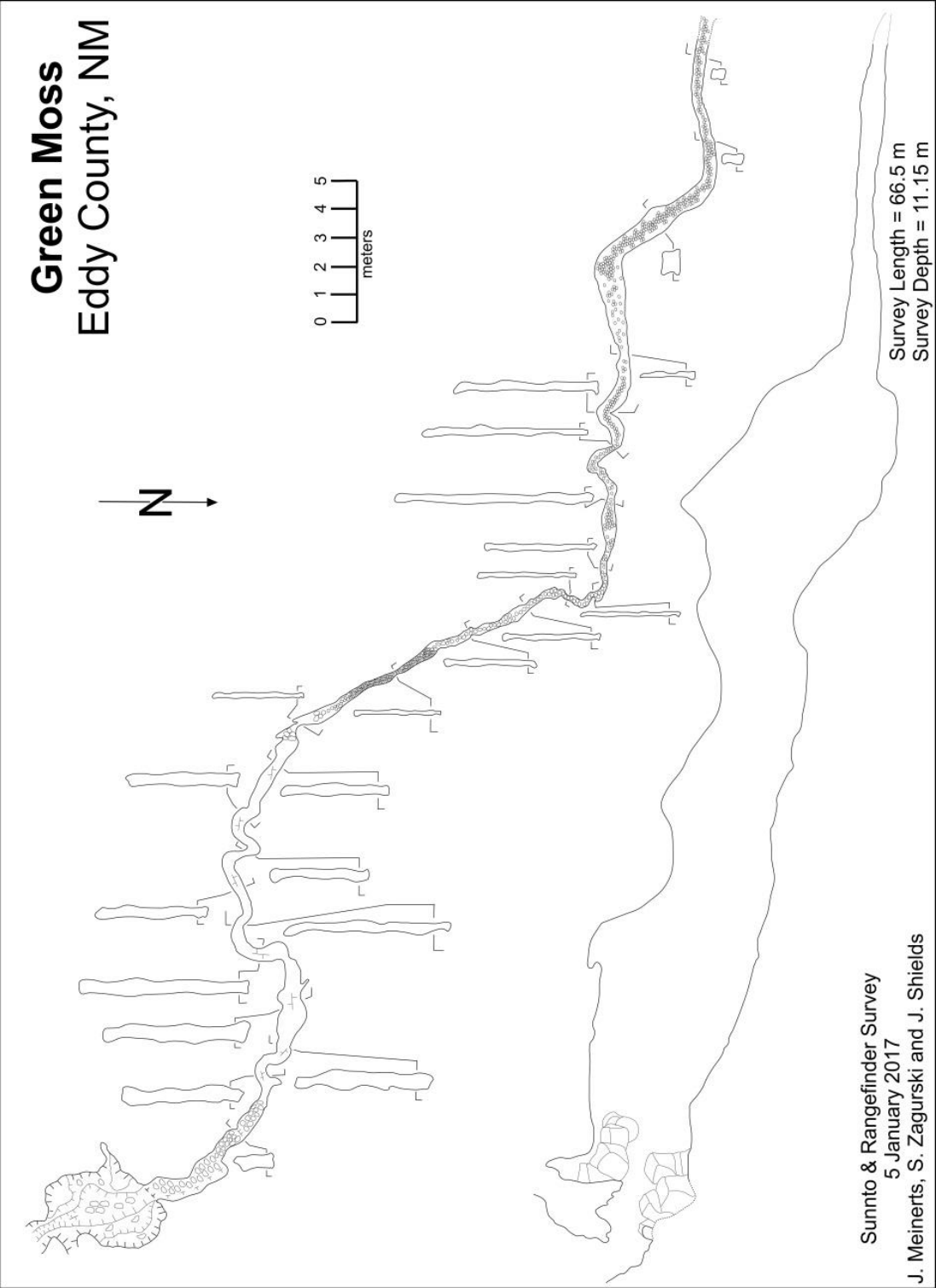


Figure C5: drafted cave map of Green Moss.

an east-west trending, incised arroyo of gypsum bedrock and soil approximately 15 m long, five m deep and four m wide at its largest point. The entrance immediately opens to a small room of collapsed bedrock from the adjacent ceiling and walls, approximately one m wide and two m tall. The cave directly narrows to a small entrance through the collapse of about one m in diameter that continues into a large passage of gypsum bedrock resembling a classic incised entrenchment of fracture-controlled passage formed within the vadose zone.

The following approximately 40 m of passage continues at an average width of one-half- to one-quarter-m and a height of three to seven m, in a sinuous fashion of extremely tight bends followed by straight stretches at a moderately steep downward gradient. The floor is mostly bedrock with areas of gypsum float and organic debris, most likely the result of large flows of surficial water during significant precipitation events. At this point, the cave passage steps down through a hypogene, vertical breccia pipe of calcitized gypsum extending approximately three lateral m, while narrowing to a more tube-like conduit one m in diameter and 10 m long. The passage became impassable because a sump was encountered, but it appears to continue with reduced aperture.

Horseshoe Cave

Horseshoe Cave (Figure C6) is located along the Texas-New Mexico border (Figure C1). The cave is approximately 60 m long and seven m deep. The entrance to the cave is located in the bottom of a large, collapsed bedrock arroyo

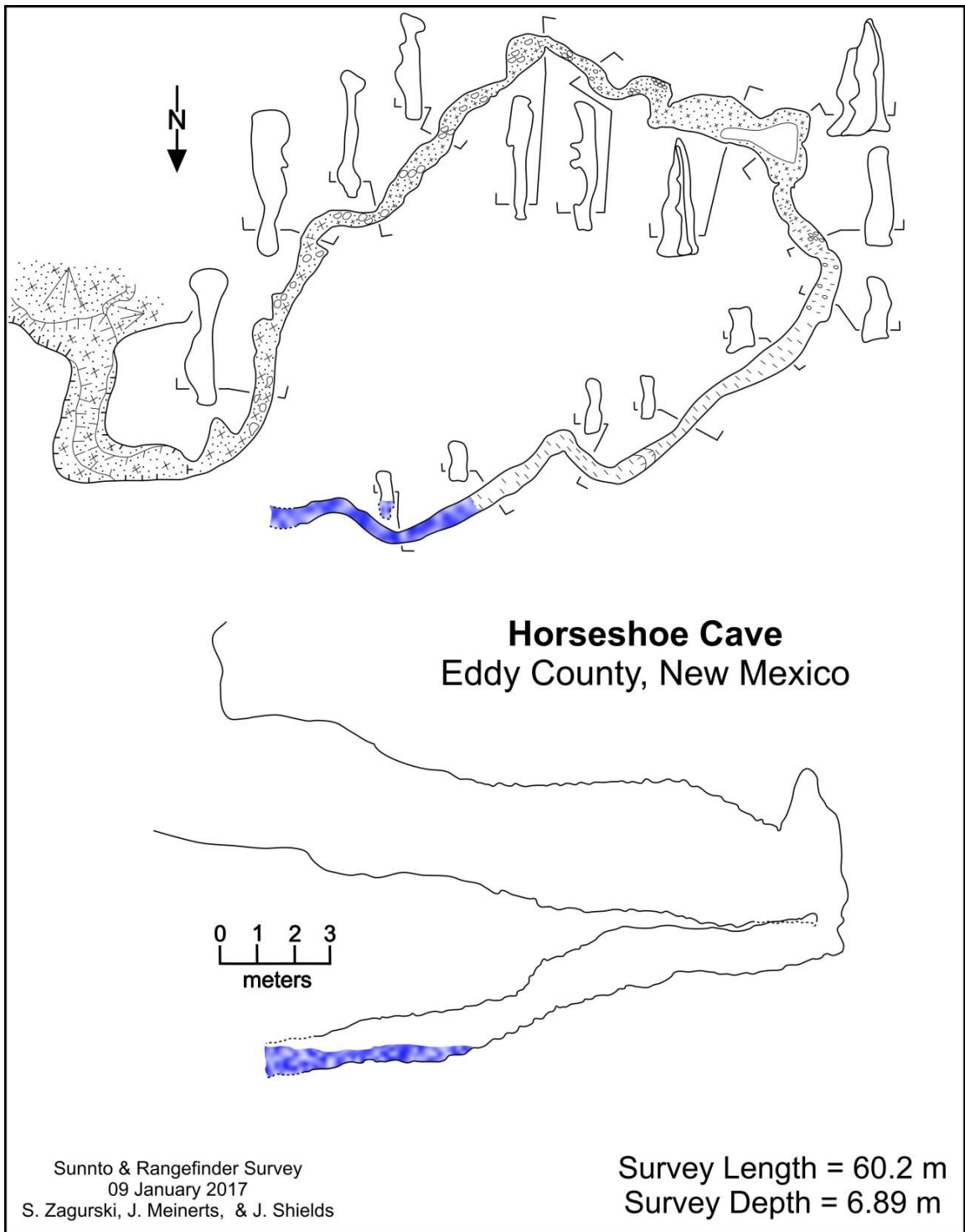


Figure C6: drafted cave map of Horseshoe Cave.

approximately 24 m in diameter and 10 m deep. Sediment and organic matter have been washed into the arroyo, forming a hill-like feature in the center with vegetation growing throughout. The entrance to the cave is four m tall and one m wide, with significant gypsum float and organic matter lining the floor. The entrenched passage continues with a relatively constant size for approximately 18 m before encountering a large section of bedrock wall that has sheared off and created a divider within the passage. Sediment and organic matter have accumulated around the feature from the flow of surface waters into the cave. After another three m, the passage begins to narrow to about one-and-one-half m tall, before crossing the phreatic zone and filling with water and mud. Fracture control patterns and vadose/phreatic entrenchment indicate epigene origins of Horseshoe Cave.

JB Hole

JB Hole (Figure C7) is centrally located within the study area (Figure C1), with a survey length of 74 m and four m in depth. The first of two entrances is an approximately one-m-tall, half-m-wide crawl located at the northern most extent of the cave. The passage immediately adjacent to the entrance opens to a three-m-wide room extending south to split into two passages. The floor is a layer of bedrock breakdown from the ceiling and walls. One of the passages extends southwest for approximately six m before narrowing from two m wide to a quarter-m.

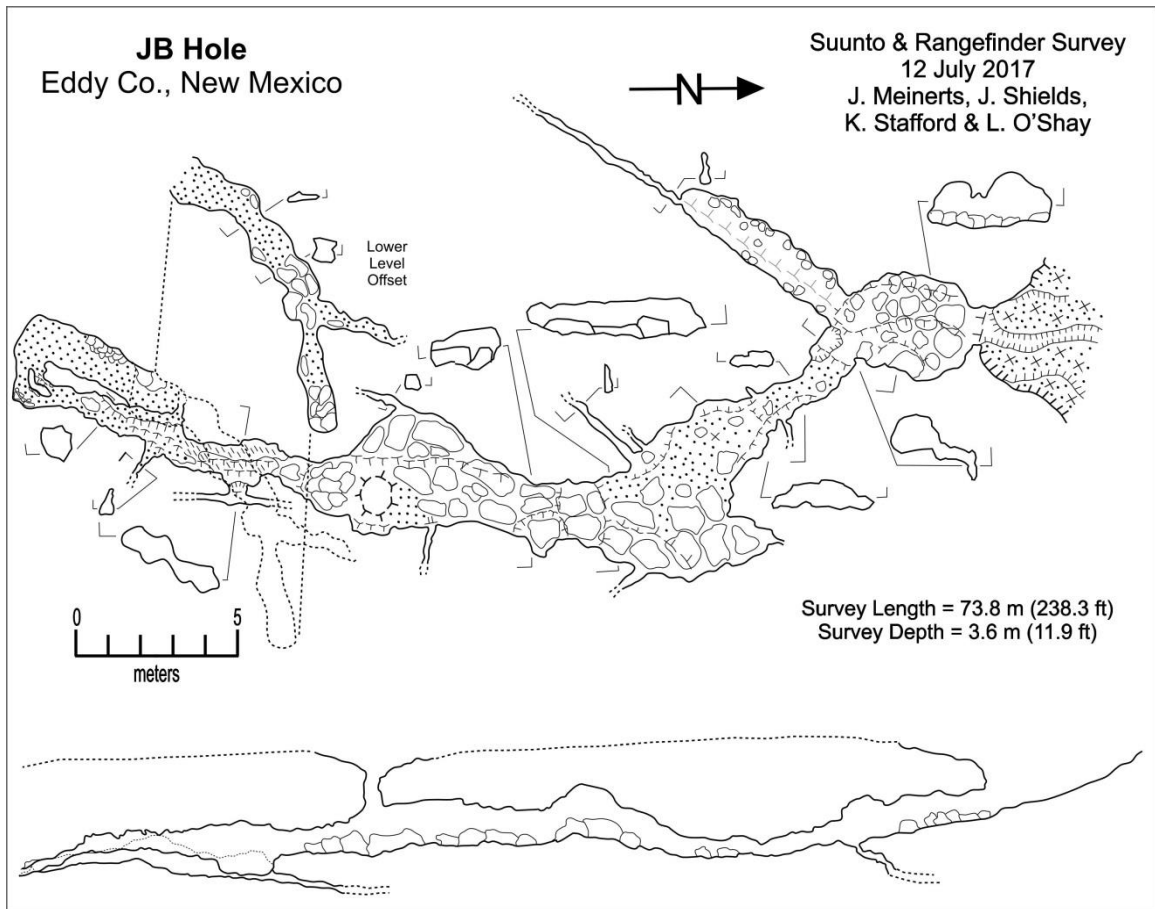


Figure C7: drafted cave map of JB Hole.

The main passage of the cave continues southeast for approximately 10 m before the subtle change to a southwest trend. Along this extent, the floor contains large amounts of gypsum bedrock breakdown from the ceiling and walls, as well as dry sediment. Several small drainage tubes are located along the base of the walls of this main passage. After traversing approximately 15 m, a second entrance to the cave is found as a skylight, approximately three m above the floor and three-fourths-m in diameter.

Beyond this second, southern most entrance, the cave narrows to approximately a quarter-m wide and half-m tall for approximately two-and-one-half m before opening to a series of collapsed rooms each no more than a m-and-one-half tall and a m wide. Eventually the cave terminates in a collapsed area that was impassable at the time of survey. A third collapsed sinkhole is located near the extent of JB Hole that likely connected to the feature before it's collapse.

JB Hole is an epigene feature formed as an entrenched and solutionally-widened fracture through gypsum bedrock. The extent of the cave follows a main fracture that has begun to collapse and exhibits large selenite crystal growth within the ceiling. Moderately-sized scallops along the walls of the cave are evidence of surficial water flow acting to further widen and entrench the cave. Suffosion of overlying and entrance soils have contributed to infilling and blockage of the greater extent of passage.

K-Hill Pit

K-Hill Pit (Figure C8) is located southwest of K-Hill (Figure C1), formed at the base of a near vertical arroyo approximately one m in diameter and three-and-on-half m deep. Small scallop features in the bedrock walls indicated rapid flow of water into the cave. At the bottom of the first pit a second, pit-like drop exists with a diameter of one-third-m and three-and-one-half m deep. The cave continues to narrow as the passage trends back below the second level shelf

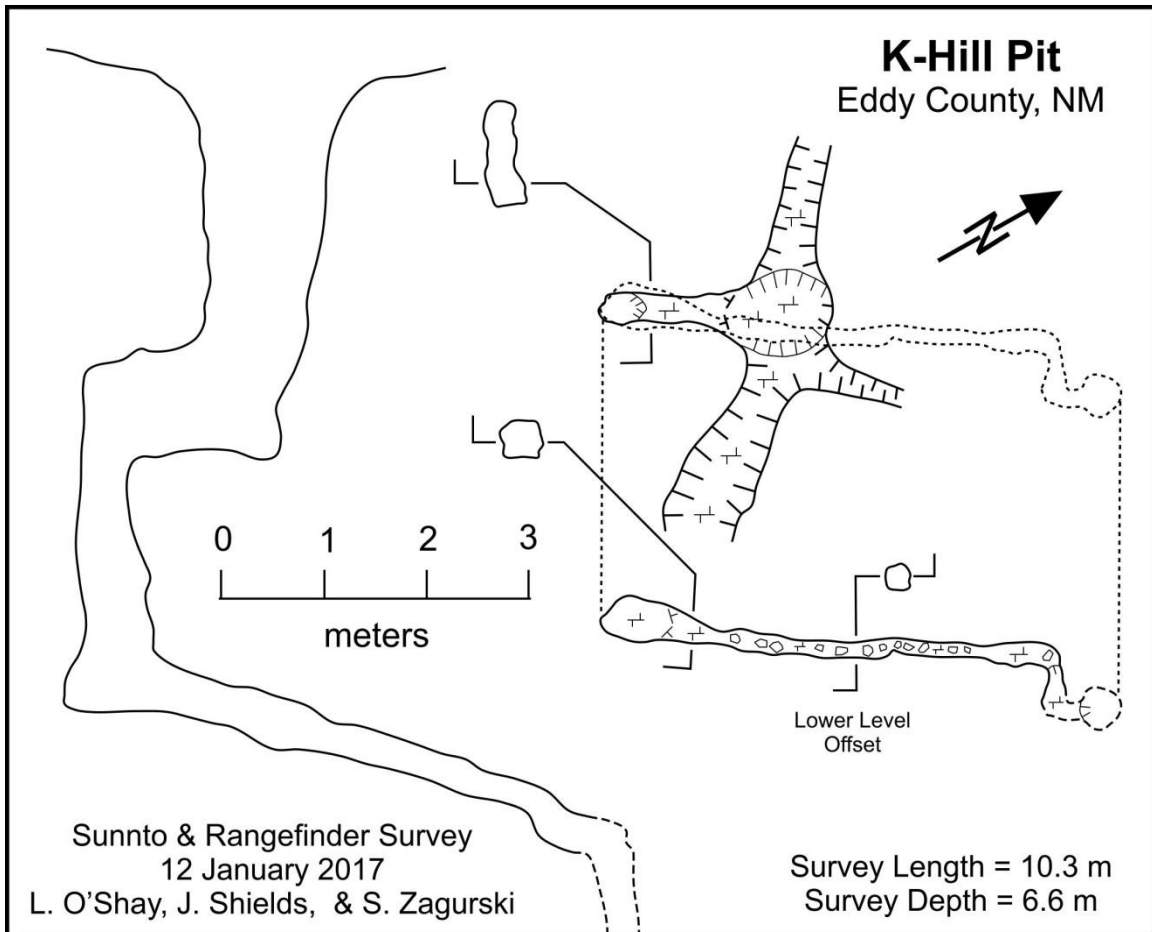


Figure C8: drafted cave map of K-Hill Pit.

feature in a northeast direction approximately three-and-one-half m before reaching a vertical drain pipe too small to enter. The ceiling of the cave shows heavy fracture control, suggestive of epigenic origins.

Lost Cave

Lost Cave (Figure C9) is a small epigene feature developed along a solutionally-widened and vadose-entrenched fracture with a length of 13 m and a total depth of three m located west of K-Hill (Figure C1). The entrance is approximately

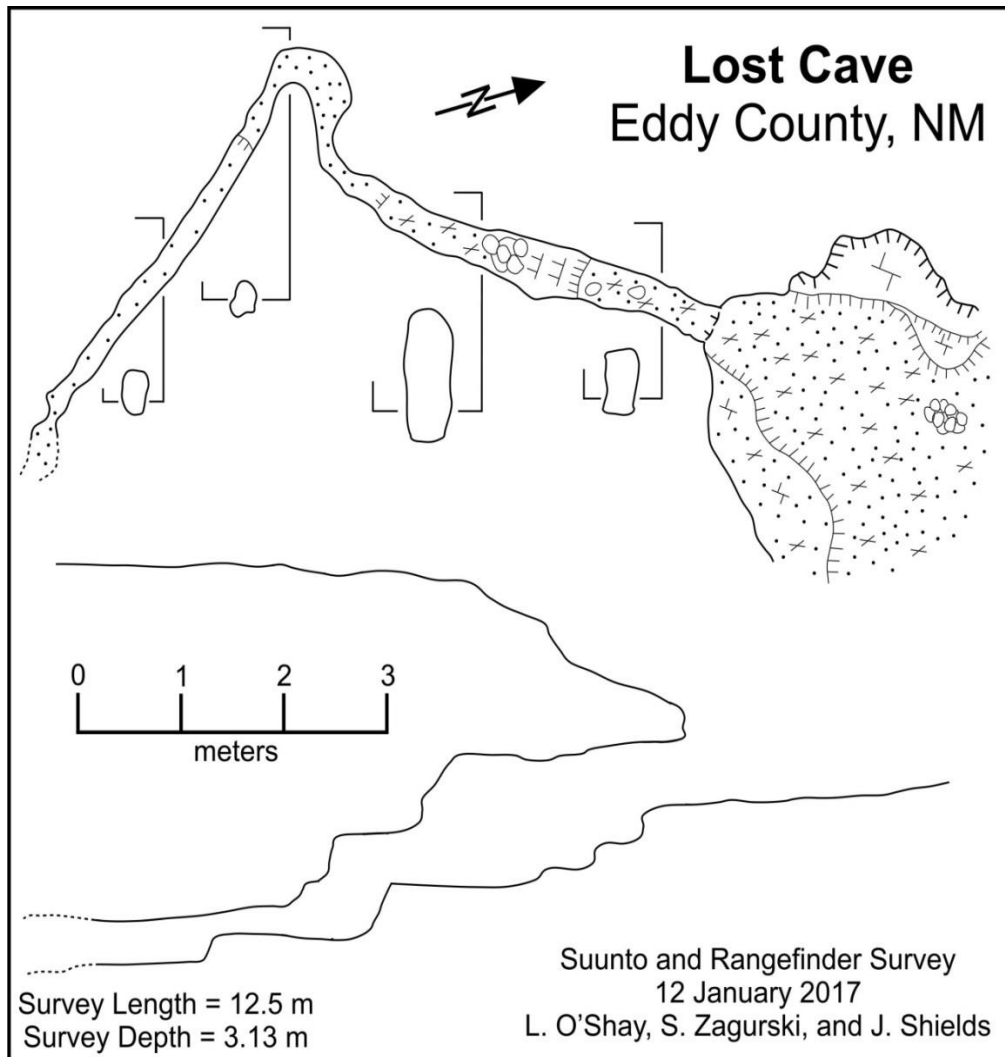


Figure C9: drafted cave map of Lost Cave.

three-fourths-m tall and a quarter-m wide, extending from a small soil sink approximately five m in a southwest direction, stepping down in depth.

After five m, the passage curves at a right angle to extend another four m southeast at a height of a quarter-m before becoming too small to enter. Plant roots from the surface and large amounts of organic matter are found in the cave, indicating suffusion also contributed to infilling.

Nicholl's Cave

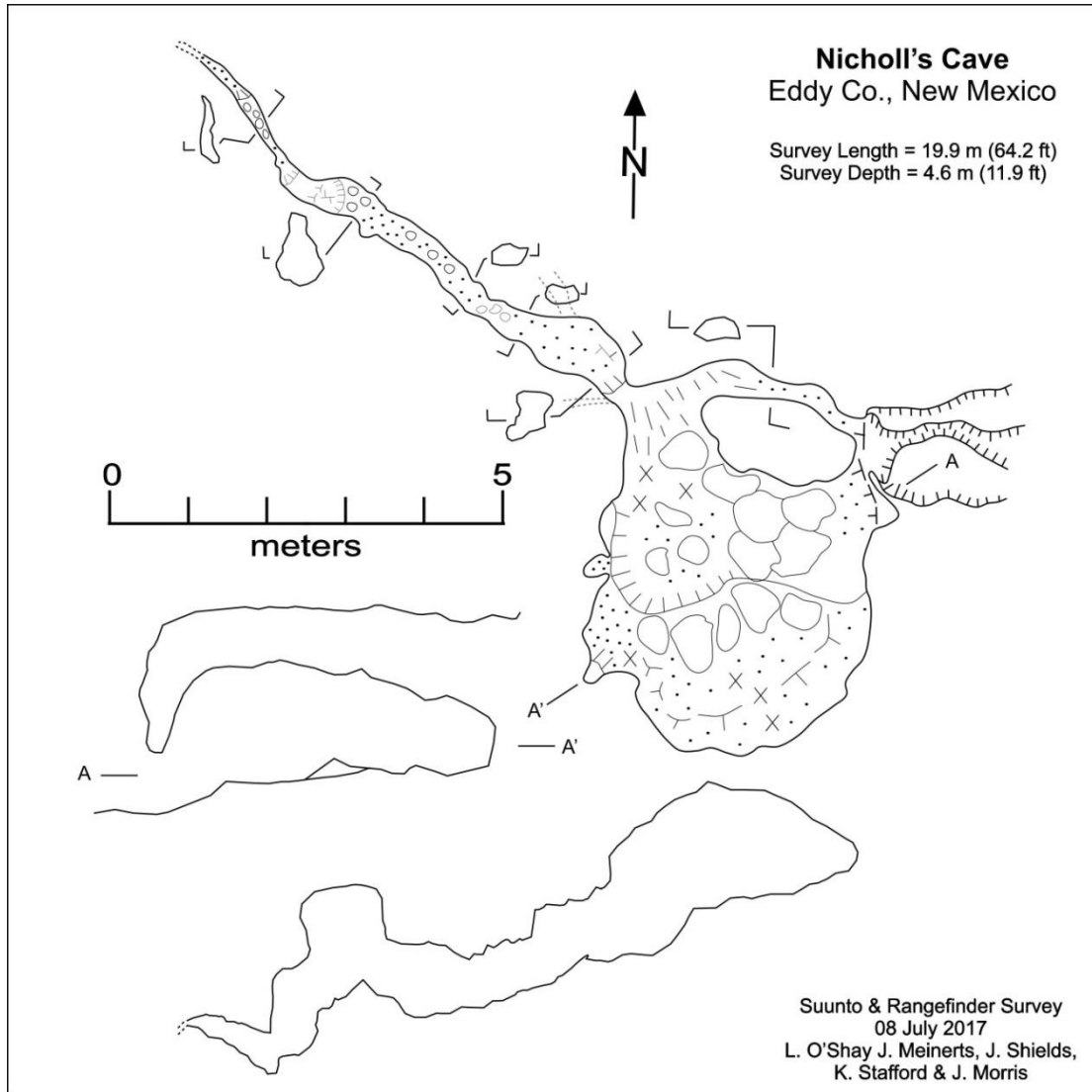


Figure C10: drafted cave map of Nicholl's Cave.

Nicholl's Cave is a small vadose zone cave system within gypsum bedrock formed by epigene processes (Figure C1). The cave features a total length of 20 m and depth of five m. The entrance to Nicholl's Cave is approximately one-half-m in diameter through indurated gypsic soil and opens to

a large room of the same material. Large sections of collapsed soil from the ceiling cover the floor. Suffosion caused by water flow from the surface to the lower cave system through subsurface fracture networks created this large soil room immediately adjacent to the entrance. The northwest corner of the room connects to solid gypsum bedrock passage about three-fourths-m in diameter and one-half-m tall, continuing in this way for nine m before becoming too narrow to continue. Gypsum float and soil line the floor along this portion of Nicholl's Cave (Figure C10). Small wall scallops, and the fracture-controlled nature of the ceiling indicate that this bedrock section of cave was created by epigene processes.

Quill Soil Cave

Quill Soil Cave (Figure C11) is located northwest of U.S. Highway 62/180 (Figure C1). The cave opens from a slight depression in the soil to converge with an entrance one m in diameter. The passage opens to three-m-wide and two-m-tall, extending four m before narrowing to one-m-wide by one-half-m-tall. The cave is completely formed within indurated gypsic soil, with boulders of soil collapse lining the passage floor. The cave opens to a small room of breakdown before extending another 12 m and opening to another room.

The passage continues in this pattern until finally narrowing to one-quarter-m in diameter, prohibiting further survey, for a total length of 49 m and depth of four m. Over time, the soil has piped through the subsurface by fluids

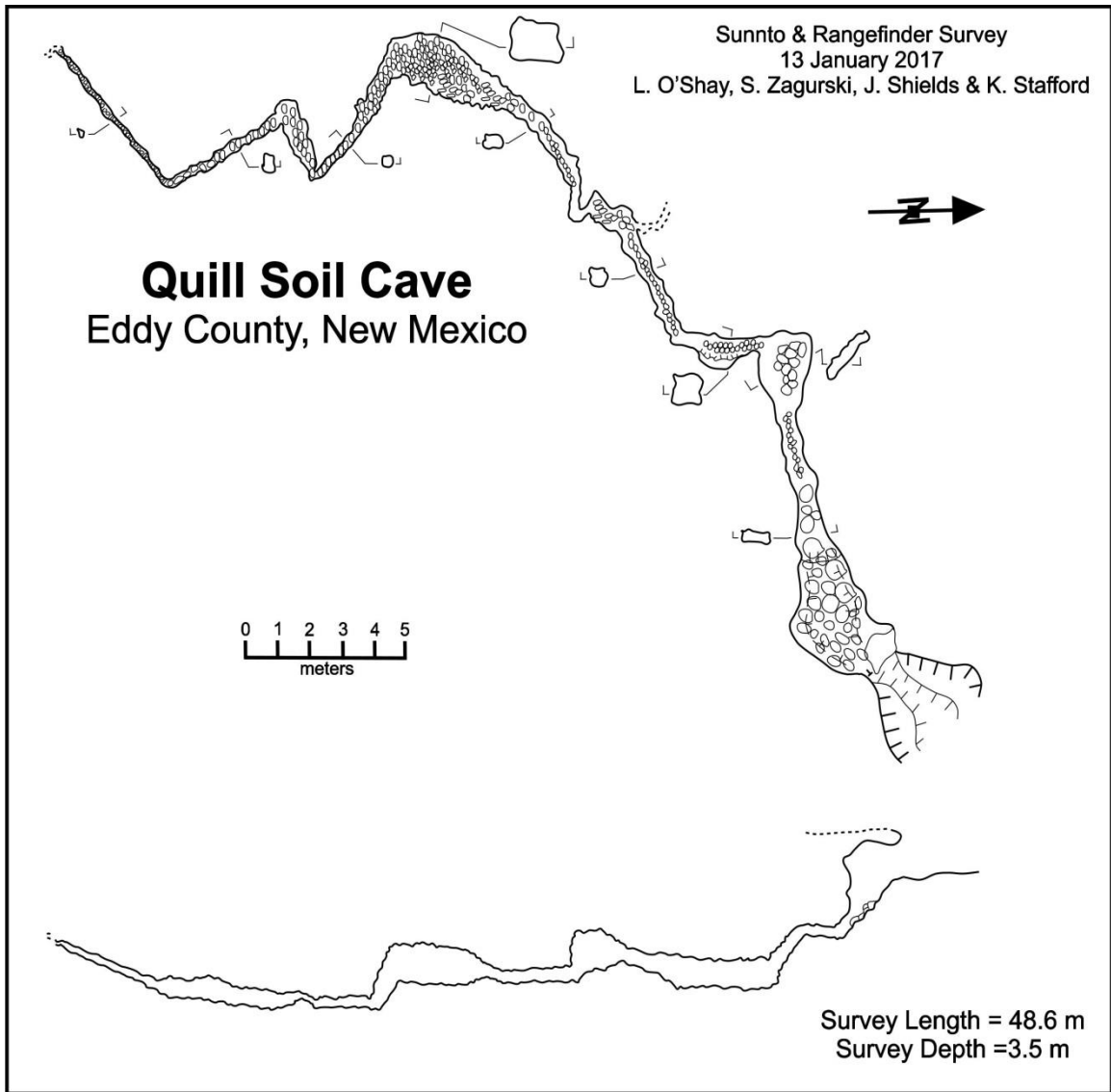
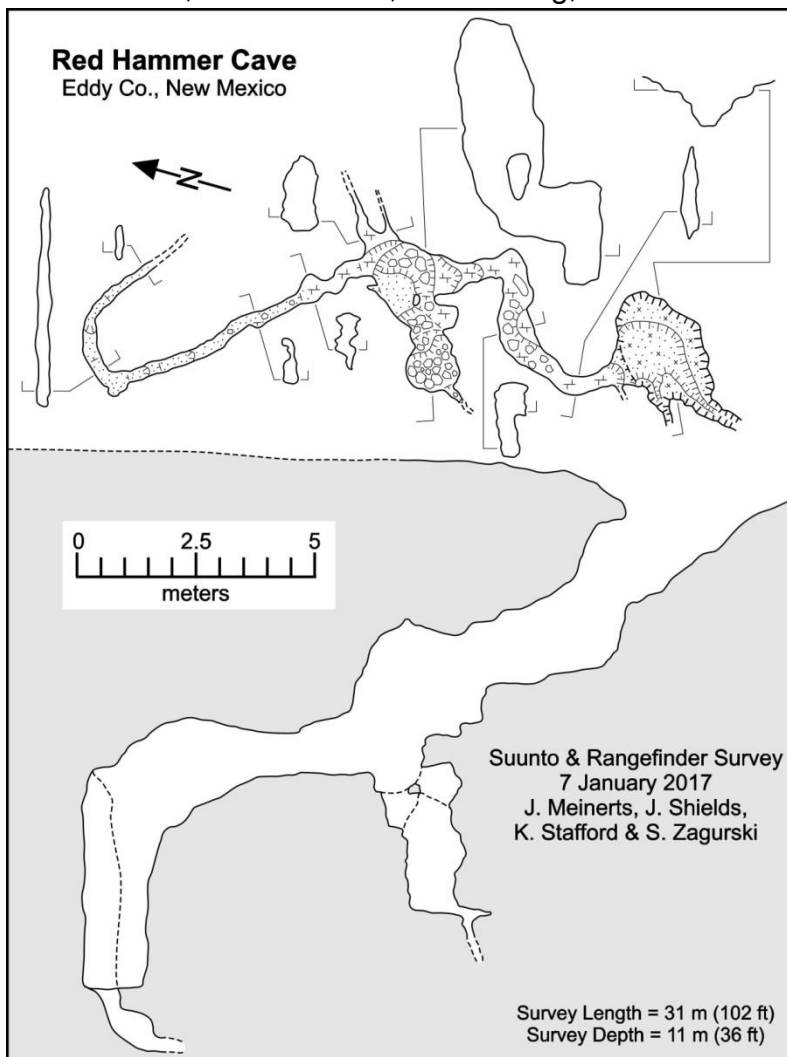


Figure C11: drafted cave map of Quill Soil Cave.

migrating downward along fractures and other preferential paths creating the suffosional void space of Quill Soil Cave (Figure 7D) seen today. The remaining soil is highly indurated forming a stable cave passage, while dissolution from surface waters has caused the breakdown scattered across the passage floor.

Red Hammer Cave

Red Hammer Cave (Figure C12) is located at the base of an entrenched bedrock arroyo two-m-wide (Figure C1). The entrance to the cave, formed within gypsum bedrock, is one-m-wide and two-m-tall. The cave immediately turns east travelling five m along an entrenched epigene passage before opening into a pit like structure, three-m-wide, one-m-long, and six-m-deep. From the entrance to



the pit, the floor is mostly gypsum bedrock with some gypsum float in areas. The pit area features three conduits one-quarter-m in diameter trending northeast and southwest at the level of the uppermost passage, further indicating epigenic phreatic formational processes.

Figure C12: drafted cave map of Red Hammer Cave.

Hypogene processes most likely formed the lower pit area, and the center spiral corkscrew feature through ascending fluids, due to the tubular passage shape and smooth wall detail. This lower hypogene feature eventually intersected epigene passage above, causing the floor to dissolve away and create a pit. Further entrenchment of the pit occurred due to preferential flow of surficial waters into the cave and down through the lower drain currently blocked by collapse at the bottom of the pit. The upper passage continues adjacent to the northern side of the pit, narrowing to half-m-wide and one-m-tall. All passages appear to be formed along fractures, widened by fluid flow. Organic matter flushed in through surface drainage lines this section of passage. After continuing another five m, the passage opens into a deeply-entrenched area five-m-tall and one-half-m-wide before the ceiling drops dramatically to a passage one-half-m-tall and plugged with sediment. At this point the passage intersects the phreatic zone, indicating phreatic-epigene formation of the entrenched portion.

VB Hole

VB Hole (Figure C13) is located along the southern side of the central portion of U.S. Highway 62/180 (Figure C1) within the study area, with a total survey length and depth of 63 m and two m, respectively. The main sinkhole is located at the north end of the cave, but the entrance itself is blocked by collapse. The larger of two remaining entrances, both of which are located within the ceiling of the passage, are 15 m southeast of the main sinkhole. This

entrance is one m in diameter and two m above the floor within gypsic soil. The cave passage is developed in solid gypsum bedrock trending northwest for 15 m at a width of 3 m. Gypsum collapse and soil line the floor in most of the cave. Additional side passages are found at the main entrance and 10 m along the passage north. These features exhibit drainage characteristics and indicate epigenic origins controlled by preexisting fractures within the bedrock.

The second entrance is much smaller than the first, and is found eight m south of the first. A shaft one-quarter-of-a-m in diameter and one m above the floor has formed within the gypsic soil above, due to diffusion processes. The passage south drastically narrows to one-quarter- m in diameter for two m before opening again to a relatively straight passage two m wide and one-and-one- half m tall until terminating in collapse 30 m later. This portion of the cave also exhibits high fracture control and epigene origins.

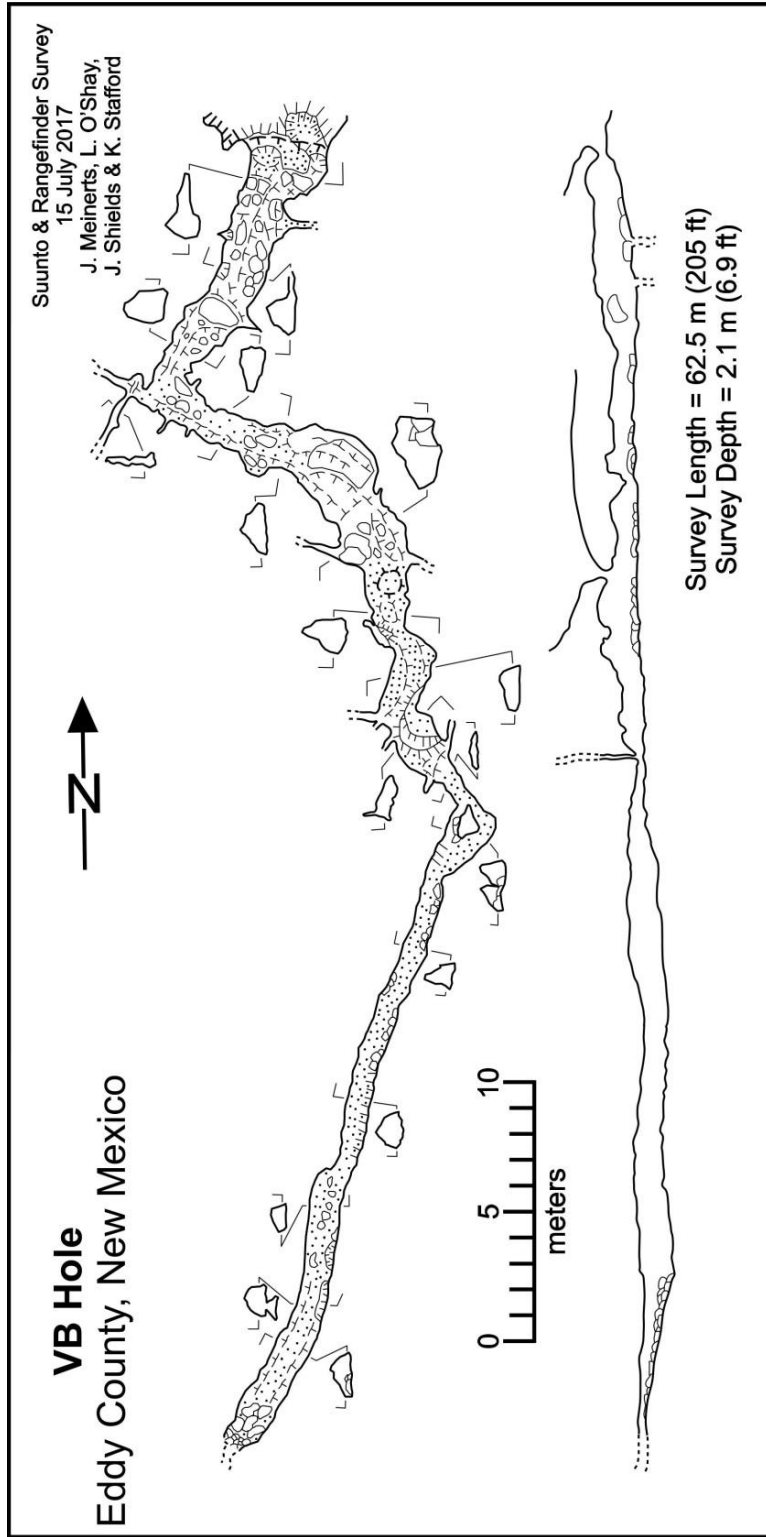


Figure C13 :drafted cave map of VB Hole.

Zombie Cave

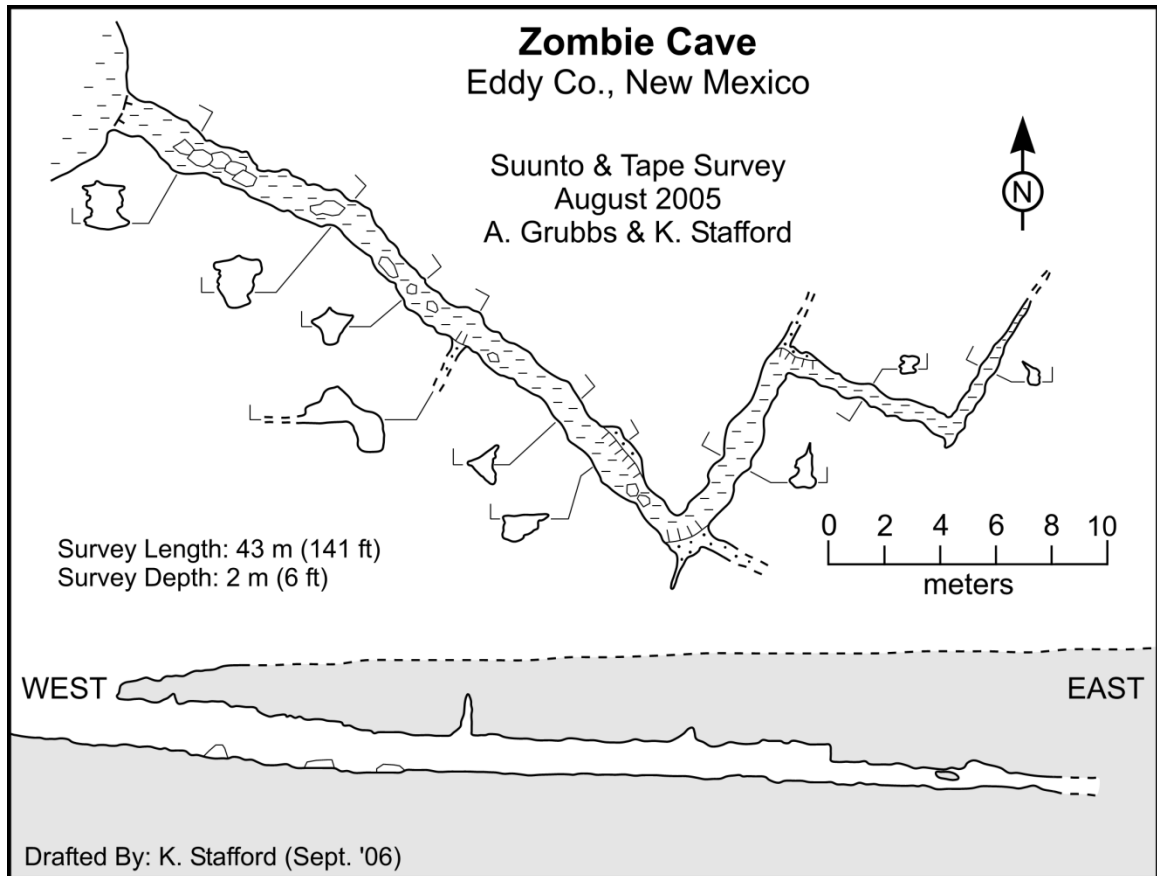


Figure C14: drafted cave map of Zombie Cave.

Zombie Cave (Figure C14) is a small epigene cave located between VB Hole and Bridge Cave (Figure C1) approximately 43 m long and two m deep. The cave entrance is located in the bottom of a bedrock sinkhole, approximately two m tall and one m wide. The passage is formed in solid bedrock. The floor of the passage is mostly bedrock with occasional collapse and dry soil. The passage is clearly fracture controlled, continuing from the entrance approximately 25 m, trending southeast at one-m-wide and one-and-one-half-m tall. The passage

forms a right angle, turning northeast for approximately 10 m at a similar height and width. Another tight, 90 degree turn to the southeast, followed by the same turn back to the northeast, ends in a decrease in passage width, impassable to the survey team.

VITA

Jessica M. Shields graduated from Brazoswood High School in Clute, Texas. In August of 2016, Jessica graduated from Stephen F. Austin State University where she received her Bachelor of Science in Geology. In August of 2016 she was admitted to the Graduate School of Stephen F. Austin State University and began pursuing her Master of Science degree in Geology. Jessica received her Master of Science degree in May of 2018.

Permanent Address: 2007 Wildwood Dr.
 Richwood, TX 77531

Style manual designation: Geological Society of America.

This thesis was typed by Jessica M. Shields.